Geochimica et Cosmochimica Acta 378 (2024) 1–35

Contents lists available at ScienceDirect

Geochimica et Cosmochimica Acta

journal homepage: www.elsevier.com/locate/gca

Accretion of warm chondrules in weakly metamorphosed ordinary chondrites and their subsequent reprocessing

Alex M. Ruzicka [a,*], Richard C. Hugo [a], Jon M. Friedrich [b,c], Michael T. Ream [a]

[a] Cascadia Meteorite Laboratory, Department of Geology, Portland State University, 1721 SW Broadway, Portland, OR 97207, USA
[b] Department of Chemistry, Fordham University, Bronx, NY 10458, USA
[c] Department of Earth and Planetary Science, American Museum of Natural History, New York, NY 10024, USA

ARTICLE INFO

Associate editor: Martin Robert Lee

ABSTRACT

To better understand chondrite accretion and subsequent processes, the textures, crystallography, deformation, and compositions of some chondrite constituents in ten lithologies of different cluster texture strength were studied in seven weakly metamorphosed (Type 3) and variably shocked ordinary chondrites (Ragland—LL3 S1, Tieschitz—H/L3 S1, NWA 5421—LL3 S2, NWA 5205—LL3 S2, NWA 11905—LL3-5 S3, NWA 5781—LL3 S3, NWA 11351—LL3-6 S4) using optical and electron microscopy and microtomography techniques.

Results support a four-stage model for chondrite formation. This includes 1) limited annealing following collisions during chondrule crystallization and rapid cooling in space prior to accretion, as evidenced by olivine microstructures consistent with dislocation recovery and diffusion; 2) initial accretion of still-warm chondrules into aggregates at an effective chondrite accretion temperature of ~900-950 °C with nearly in situ impingement deformation between adjacent chondrules in strongly clustered lithologies (NWA 5781, Tieschitz, NWA 5421, NWA 5205 Lithology A), as evidenced by intragranular lattice distortions in olivine consistent with high-temperature slip systems, and by evidence that some olivine-rich objects in Tieschitz accreted while partly molten; 3) syn- or post-accretion bleaching of chondrule mesostases, which transferred feldspathic chondrule mesostasis to an interchondrule glass deposit found in strongly clustered lithologies, as evidenced by chemical data and textures; and 4) post-bleaching weak or strong shocks that resulted in destruction of interchondrule glass and some combination of brecciation, foliation of metal and sulfide, and melting and shock-overprinting effects, as evidenced by poor cluster textures and presence of clastic texture, alignment of metal and sulfide grains caused by shock compression, presence of impact-generated glass, and changes in olivine slip systems. The data support the model of Metzler (2012), who suggested that chondrules in ordinary chondrites accreted while still warm to form cluster chondrite textures as a "primary accretionary rock" (our Stage 2), and that subsequent brecciation destroyed this texture to create chondrites with weak cluster texture (our Stage 4).

1. Introduction

Chondrites are unique sedimentary rocks that formed at the birth of the solar system by aerodynamic processes in a space environment to form planetesimals, pieces of which were ultimately delivered to Earth as meteorites (e.g., Dodd, 1981; Hutchison, 2004). The most common such meteorites are ordinary chondrites. The orthodox view holds that ordinary chondrites accreted at low temperatures (<400 °C) and were then variably heated to progressively higher temperatures with increasing depth in their parent bodies, with maximum temperatures approaching the metal-troilite eutectic at ~950 °C, establishing a metamorphic Type 3-6 series that corresponds to increasing metamorphic intensity (Dodd, 1981). The discovery that radioactive ^{26}Al could have been an early heat source strengthens this idea of prograde metamorphism (Hutchison, 2004).

However, "hot accretion" of chondrules is supported by the presence of mutually indenting chondrules in Type 3 ordinary chondrites that may have interacted while warm (Hutchison et al., 1979; Hutchison and Bevan, 1983; Hutchison, 2004; Metzler, 2012). Rubin and Brearley (1996) discounted the significance of occasional "misshapen chondrules" in ordinary chondrites, but Metzler (2012) noted the presence of clasts in Type 3 ordinary chondrites in which nearly every chondrule

* Corresponding author.
E-mail address: ruzickaa@pdx.edu (A.M. Ruzicka).

https://doi.org/10.1016/j.gca.2024.05.031
Received 7 November 2023; Accepted 31 May 2024
Available online 4 June 2024

Table 1
Meteorite samples studied.

Meteorite[1]	Type & subtype[2]	CML thin sections[3]	CML bulk samples[3,4]
NWA 5781	LL3.3	0244-2*	0244-3
NWA 11351 Lith. A[5]	LL3/4	0754-2*	0754-1
NWA 11351 Lith. B[6]	LL3/4	0754-2*	0754-1
NWA 11351 Lith. C[7]	LL5-6	0754-3	0754-1
Tieschitz	H/L3.6	0781-A, 0781-B*	–
NWA 5421	LL3.7	0953-3A*, 0953-3B	–
NWA 5205 Lith. A[8]	LL3.7[13]	0954-1A-1*	–
NWA 5205 Lith. B[9]	LL3.7[13]	0954-1A-1*	–
NWA 11905 Lith. A[10]	LL3.10	0978-1A, 0978-1B, 0978-3B*	–
NWA 11905 Lith. B[11]	LL3	0978-1A, 0978-1B, 0978-3B*	–
NWA 11905 Lith. C[12]	LL5	0978-1A, 0978-2A, 0978-3B*	–
Ragland	LL3.4	1051-1*	–

[1] Lith. = lithology. [2] Data from MBD (2023) except where noted. [3] CML = Cascadia Meteorite Laboratory; * Indicates section was studied for cluster texture strength and with EBSD methods. [4] Samples studied via μCT. [5] Chondritic clast, with strong cluster texture (Fig. 1g). [6] Clastic, with weak cluster texture (Fig. 1g). [7] Clastic, dominated by Type 5 and 6 material. [8] Chondritic clast, with strong cluster texture (Fig. 1e). [9] Clastic, with weak cluster texture (Fig. 1e). [10] Chondritic clast, with opaque matrix ("Lithology 1" in MBD, 2023) (Fig. 1f). [11] Chondritic, Type 3 host, with semi-opaque matrix ("Lithology 3" in MBD, 2023) (Fig. 1f). [12] Type 5 chondrite clast set in Type 3 host ("Lithology 2" in MBD, 2023) (Fig. 1f). [13] Revised to LL3.7 from LL3.2 (Müsing et al., 2021).

was "misshapen" and termed this texture "cluster chondrite". Metzler (2012) suggested that these cluster lithologies formed by the collision of warm chondrules by rapid accretion following the formation of chondrules as melt droplets. Metzler further posited that such cluster lithologies represented a "primary accretionary rock" that was later brecciated to form non-cluster textures in ordinary chondrites.

How chondrules accreted, and how chondrites formed, is of crucial importance for evaluating the growth of asteroidal and larger-sized bodies and ultimately terrestrial planets (Johansen et al., 2015). Here we test the model of Metzler (2012) using innovative Electron Backscatter Diffraction (EBSD) techniques that evaluate the relationship between deformation and heat, together with optical microscopy, scanning electron microscopy (SEM), and X-ray microtomography (μCT), with the goal of better understanding accretion and subsequent processes. Innovations in this study include: 1) the development of a quantitative metric for cluster texture strength; 2) the development of an improved EBSD metric for post-deformation annealing (Grain Orientation Spread [GOS] skewness ratio); and 3) the use of slip system systematics inferred from intragranular lattice distortions for olivine as measured by EBSD techniques to estimate deformation temperatures during shock events (T_{deform} values). We also demonstrate than an EBSD metric for grain-scale deformation (GOS) in olivine is an unbiased, quantitative metric for mean shock stage and the intensity of shock deformation; and provide new observations of petrographic features in chondrites that relate to accretion and post-accretion conditions, including bleached chondrules, interchondrule glass (previously known as white matrix), and a newly-recognized class of fine-grained olivine-rich objects. Preliminary results were reported by Goudy (2019) and Ruzicka and Hugo (2022a,b).

2. Samples and methods

2.1. Samples and data products

Table 1 lists information about the meteorite samples studied and Fig. 1 shows representative thin section images of the meteorites. Samples include various polished thin sections for optical and electron microscopy studies as well as hand specimen samples for two of the meteorites used for microtomography studies. NWA 5205 and NWA 5421 may be paired (Metzler and Pack, 2016; Müsing et al., 2021), which is not inconsistent with our data.

Various data products were generated. Table S1 (Appendix A, Supplementary Material) gives a list of data types, abbreviations, and parameters for all the techniques that were used. Table S1 describes all italicized abbreviations in the Text.

2.2. Optical microscopy

All thin sections were studied by optical microscopy prior to carbon coating. This included determination of shock stage based on olivine, using a Leica DM 2500 petrographic microscope in transmitted and cross-polarized light mode. Shock stage is presented as both a conventional shock stage (*CSS*) ranging from S1 to S6 (Stöffler et al., 1991), taken to be equivalent to C-S1 to C-S6 (Stöffler et al., 2018, 2019), as well as a weighted shock stage (*WSS*, a mean shock stage determined by observations of different olivine grains) using quantitative criteria (Jamsja and Ruzicka, 2010). To minimize the effects of possible operator bias, all shock stage determinations were made by a single researcher (AMR).

In addition, optical microscopy was performed prior to carbon coating using a binocular microscope (Leica EZ 4D) in transmitted light mode for the determination of cluster texture strength. Binocular image mosaics assembled by using Adobe Photoshop software were analyzed with ImageJ software to measure chondrule perimeter lengths and to determine the proportion of these boundaries that conform ("fit") to their nearest neighbors. The proportion of boundaries that conform is given by the parameter C_s:

$$C_s = (\textit{total perimeter length of conforming chondrule boundaries})/(\textit{total perimeter length of all chondrule boundaries}) \quad (1)$$

C_s gives an overall measure of cluster texture strength (0 = perfectly non-conforming, 1 = perfectly conforming). These values are quantitative, but they depend on a qualitative judgment of whether boundaries "conform". This judgment can be influenced by thick opaque rims that might be present on chondrules. If such rims are present (either composed of fine-grained material or opaque minerals such as metal or troilite), they would have the effect of separating chondrules, and adjacent chondrule margins would not be counted as "conforming". Only those chondrules that are in proximity as viewed in transmitted light, and that have boundaries that mimic adjacent chondrules, are counted as "conforming". To minimize the effects of possible operator bias, all C_s measurements were made by a single researcher (MTR).

2.3. Electron microscopy

Scanning Electron Microscopy (SEM) and Electron Backscatter Diffraction (EBSD) were performed using a Zeiss Sigma Variable Pressure-Field Emission-Scanning Electron Microscope (VP-FE-SEM) instrument operated at 20 kV (EBSD) or 15 kV (SEM) and low (5-10 nA)

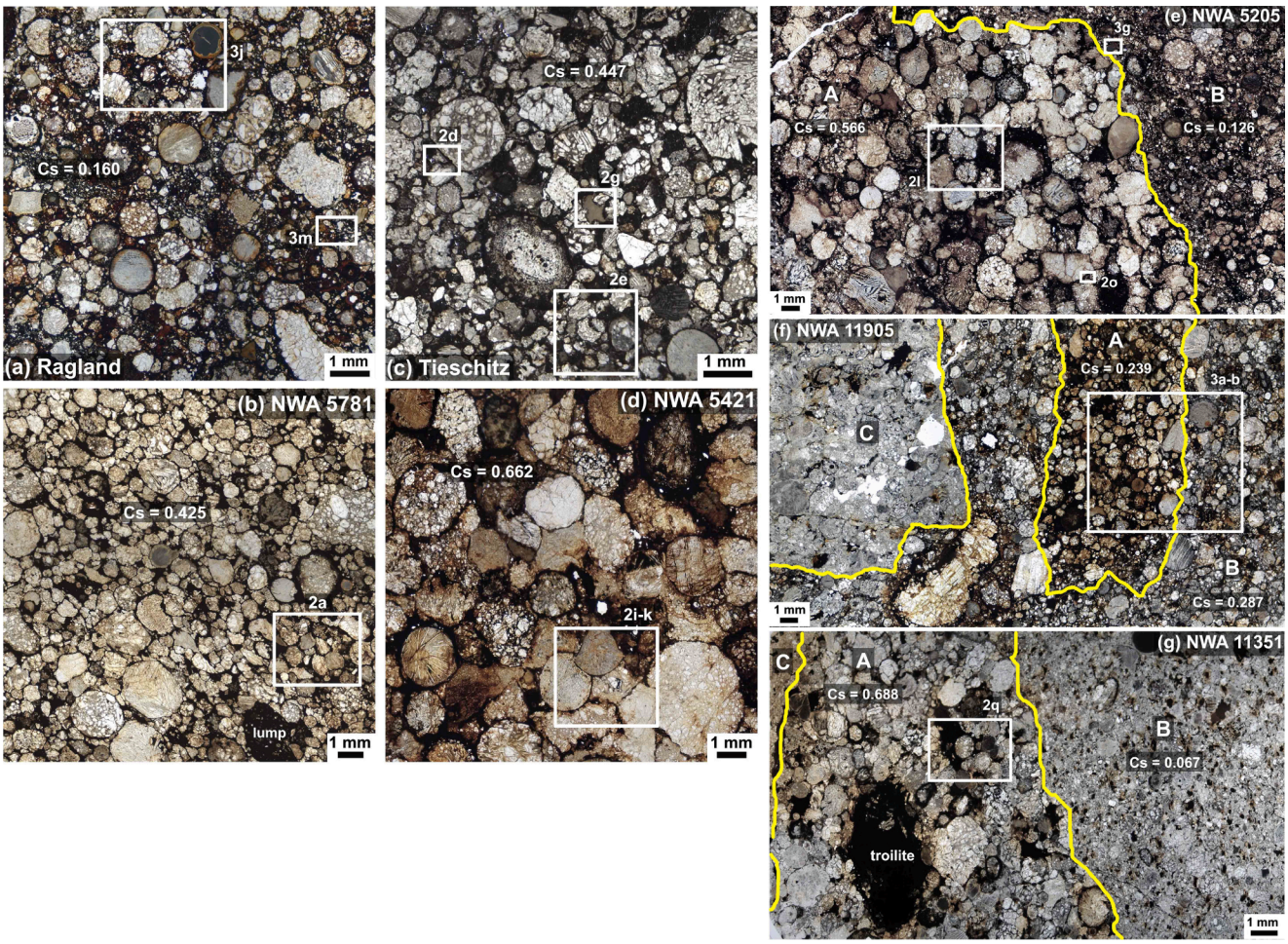

Fig. 1. Transmitted light binocular micrographs of the Type 3-bearing chondrites in this study showing variations in chondrule clustering texture, where C_s = cluster texture strength (= the proportion of chondrule edges that conform to their neighbors). Fields outline areas shown in more detail in Fig. 2 and 3. **(a)** Ragland. **(b)** NWA 5781. **(c)** Tieschitz. **(d)** NWA 5421. **(e)** NWA 5205 has two lithologies, A and B. **(f)** NWA 11905 has three lithologies, A, B, and C. **(g)** NWA 11351 has three lithologies, A, B, and C.

sample currents. For energy dispersive spectroscopy (*EDS*) an Oxford Instrument XMax50 was used prior to April 2019 and an Oxford Instruments 65 UltimMax was used after this date. For EBSD a Nordlys-Nano EBSD detector with 4-diode forward scattering electron detectors was used prior to August 2020, and an Oxford Instruments Symmetry detector with a 5-diode forward scattering detectors was used after this date.

For SEM work, backscatter electron (*BSE*) imaging and quantitative *EDS* analyses were performed at a standard 0° tilt and 8.5 mm focus distance. Quantitative *EDS* analysis used factory elemental standardizations and beam current standardization using pure Cu tape. This included analyses in focused spots as well as "bulk" analyses from larger analysis areas (~5-50 μm across) extracted from chemical maps. For bulk analyses, a CIPW norm procedure from Best (1982) modified to include $Fe_{80}Ni_{20}$ metal (all Ni into metal) and troilite (all S into troilite) and mineral densities from Gaines et al. (1997) was used to calculate normative composition. No attempt was made to correct for the unequal density effect in bulk analyses (Warren, 1997), thus elements concentrated in low-density feldspathic phases (e.g., Na, Al) might be slightly overestimated in bulk analyses relative to other elements sited in higher-density phases. According to Grossman et al. (2000), suitable correction factors might be (relative to Si) approximately 0.83 for Na and Al; 1.02 for Ca, and 1.03 for Mg and Fe. Given that we primarily compare chemical trends between constituents, our conclusions will not be significantly affected by ignoring corrections.

For EBSD work, polished sections were prepared by hand polishing using a 0.05 μm colloidal silica solution (Buehler No. 815-110) for 55-75 minutes, followed by cleaning in an ultrasonic bath of deionized water, drying, and the application of a thin (~5 nm thick) coat of evaporated carbon. In the SEM, samples were positioned at the standard 70° tilt from horizontal for optimal diffraction, and most runs included simultaneous *EDS* and EBSD data acquisition, although *EDS* data in such a tilted configuration were for qualitative textural-chemical study only. Different kinds of EBSD maps were obtained. They include Large Area Maps (*LAMs*), with a typical step size of 4 μm that enabled mapping over large portions of thin sections, and Targeted Maps (*TMs*), with smaller step sizes to cover a smaller area in more detail. *TMs* with larger (regional) mapping areas are also considered to be representative of lithologies and are called *miniLAMs*.

Oxford Instruments software AZtec versions 3.2-6.0, Channel5, and AZtecCrystal versions 1.1-2.2 were used to obtain and analyze SEM and EBSD data. For EBSD data reduction, no post-acquisition "cleaning" (e.g., filling of non-indexed pixels, or replacement of wildspikes) was performed, and criteria for grain identification were set to a minimum of 5 contiguous pixels and a critical grain boundary misorientation of 15°, all in accordance with previous work on Type 6 ordinary chondrites (Ruzicka and Hugo, 2018; Hugo et al., 2020). Crystal match files (forsterite, hypersthene, clinoenstatite, diopside, albite, bcc Fe-metal, fcc Fe-metal, tetrataenite, chromite, whitlockite) were the same as used in this earlier work, but with nepheline and sodalite added as possible

phases.

2.4. SEM-EBSD maps and data

Table S1 (Appendix A, Supplementary Material) gives a list of EBSD map types, abbreviations, and parameters. Most EBSD maps are overlays that portray a property shown in false color, such as crystal 3D orientation (Inverse Pole Figure or *IPF* maps), one of several deformation parameters, or X-ray intensity for one or more elements, together with a property for electron or diffraction intensity of some sort shown in monochrome, such as Band Contrast (*BC*) intensity, simulated *BSE (Electron)* intensity, or Forescatter Diode (*FSD*) intensity. Deformation map types include: (1) Grain Reference Orientation Deviation angle or *GROD angle* maps (e.g., Fig. 2a), which show changes in the orientation of crystals with respect to the average grain orientation such as caused by intracrystalline deformation; (2) Local Misorientation or *LocMis* maps (e.g., Fig. 2j), which show smaller-scale changes in crystal orientations such as caused by deformation; (3) Kernel Average Misorientation or *KAM* maps (e.g., Fig. 2n, 3b), which show somewhat larger-scale changes in crystal orientations such as caused by deformation; and (4) Grain Orientation Spread (Brewer et al., 2009) or *GOS* maps (e.g., Fig. 3d), which show grain-scale average misorientations such as caused by deformation. Table S1 gives details.

Tabulated EBSD grain lists, including various EBSD grain parameters such as equivalent grain size (*d*, the diameter of a circular grain with the same area as measured, given in microns) and *GOS* were compiled for the principal phases in each map, including olivine (forsterite), clinoenstatite, orthopyroxene (hypersthene), plagioclase (albite), troilite, and kamacite (or martensite) (bcc Fe-metal). If map subsets were defined (e.g., for chondrule and interchondrule areas), grain lists were extracted and analyzed for the subsets. Although data for multiple phases were obtained, attention was focused on olivine in this work.

Grain list data for the principal phases were imported into Excel spreadsheets together with map products for these phases. In these spreadsheets, the distribution of *GOS* values was determined for olivine grains in different grain size bins (d>50 μm, d=15-50 μm, d=5-15 μm, and d<5 μm) and was used to calculate the skewness values of *GOS* for specified grain sizes *d*, defined here as:

$$Sk_d = (\text{mean } GOS_d)/(\text{median } GOS_d) \quad (2)$$

where $Sk > 1$ indicates positive skewness (high proportion of low-*GOS* grains, but presence of some high-*GOS* grains) and $Sk < 1$ indicates negative skewness. Because a positively skewed *GOS* distribution can be associated with annealing, $Sk_{d>50}$ (as defined here) for olivine was previously referred to as an "annealing parameter" (Ruzicka and Hugo, 2018; Goudy 2019; Hugo et al., 2020), but because other physical processes can cause similar distributions, here skewness is given a neutral designation. *Sk* is a measure of asymmetry in *GOS* distribution for a grain population with a given number of grains (*Ng*) and can be considered a measure of deformation heterogeneity, i.e., having a significant number of grains with *GOS* values that are either higher or lower than most other grains. Comparison of different maps for olivine in each lithology indicate that when $Ng \geq 40$, reasonably consistent results are obtained for *Sk*, but that more variable and therefore possibly unrepresentative results are obtained for smaller values of *Ng*. Thus, *Sk* determinations are discussed only for datasets with $Ng \geq 40$.

For olivine, Crystal Rotation Axis (*CRA*) plots were used to portray the distribution of misorientation rotation axes, in crystal coordinates, between adjacent pixels in the 2-10° and 0.5-2° ranges. *CRA* plots were contoured according to the spatial density of data points given by values of Multiples of Uniform Distribution (*MUD*), using 25° half-width contouring to emphasize broad trends. In the spreadsheets, the *MUD* values were used to calculate the fraction (f_i) of misorientations in different directions (i = <100>, <210>, <010>, <012>, <001>, <101>) in an olivine crystal frame. A useful parameter related to rotation axis directions is $R_{2\text{-}10}$, which is the proportion of 2-10° misorientation rotations in the <010> and <001> directions compared to the sum of rotations in the <010>, <010> and <100> directions:

$$R_{2-10} = \left(f_{<010>} + f_{<001>}\right)/\left(f_{<100>} + f_{<010>} + f_{<001>}\right) \quad (3)$$

An analogous expression holds for 0.5-2° misorientation rotations ($R_{0.5\text{-}2}$). Because <010> and <001> rotations are associated with slip systems that are more easily activated at high temperatures, $R_{2\text{-}10}$ was previously referred to as a "temperature parameter" (Ruzicka and Hugo, 2018, Goudy, 2019; Hugo et al., 2020) as it is related to the temperature of deformation (Ruzicka and Hugo, 2018), but it is more directly related to deformation slip directions (proportion of **c**-type and **a**-type dislocation slip in olivine; Ruzicka and Hugo, 2018) that can be affected by temperature of deformation as well as other variables, and is here given a neutral designation.

For evaluating EBSD measurement quality, we can consider various types of measures. Mean Angular Deviation (*MAD*) measures the mean angular deviation between EBSD-indexed grains and the crystal match files and is an indicator of fitting quality. For olivine, a typical average *MAD* value for indexed olivine grains using the forsterite crystal match file (Ruzicka and Hugo, 2018) in the acquired datasets is ~0.5°. Also important for evaluating data quality is analytical precision for crystallographic orientation, which for olivine in our maps is estimated as ≤0.1-0.2° with a similar detection limit (Ruzicka and Hugo, 2018). This can be taken as an analytical precision for values of *GOS* obtained in this work. Another important measure of measurement quality is repeatability of EBSD metrics (e.g., *GOS*, $R_{2\text{-}10}$, *Sk*) for maps obtained in different areas of the same lithology. For repeatability in *LAMs* and *miniLAMs*, we define a "representative error" for EBSD metrics based on the ±1 standard deviation of values for the seven maps obtained for Lithology A in NWA 5205, which is the largest dataset obtained for a given lithology. The same relative error was applied to *LAM* and *miniLAM* data for all lithologies. This representative error measures how well "averaged" values for a particular lithology are determined considering combined analytical errors and possible sample variability. It provides a better idea of the true uncertainty associated with the averaged values than standard deviations of individual map measurements.

A complete list of all SEM datasets for Type 3 chondrites, including EBSD and non-EBSD SEM sessions, is given in Table S2 (Appendix A, Supplementary Material), which includes metadata as well as comments of noteworthy features revealed in maps.

2.5. X-ray microtomography

Samples of two meteorites (NWA 5781 and NWA 11351) were selected for X-ray microtomography (μCT) studies based on appropriate sample shape (approximately equidimensional), size (small enough so imaging the entire sample at adequate resolution is possible, but large enough to give adequate volumes of various lithologies), and scientific interest, as representatives of chondrites containing various Type 3 cluster lithologies. A GE phoenix v|tome|x s240 μCT system at the American Museum of Natural History was used to fully image a 21.8 g sample (CML 0754-1) of the NWA 11351 chondrite and a 7.1 g sample (CML 0244-3) of the NWA 5781 chondrite at a resolution of 16.5 μm/voxel and 15.5 μm/voxel, respectively, which is a similar resolution to what has been used previously for chondrites (e.g. Friedrich et al. 2008, 2017). A current of 110 μA and a potential of 140 keV were used to generate polychromatic x-rays with a tungsten tube, and a 0.1 mm Cu filter was used to minimize the beam hardening artifacts associated with x-ray tube imaging. Volumes were assembled from 2D "tomo slices" and the opaque mineral grain shapes in these samples were characterized quantitatively for common orientation tendency using the strength factor *C* (Woodcock and Naylor, 1983) as used in previous work (Friedrich et al., 2017), and for the type of fabric (foliation, lineation) using the *K-parameter* of Woodcock and Naylor (1983) and the *T-parameter* of

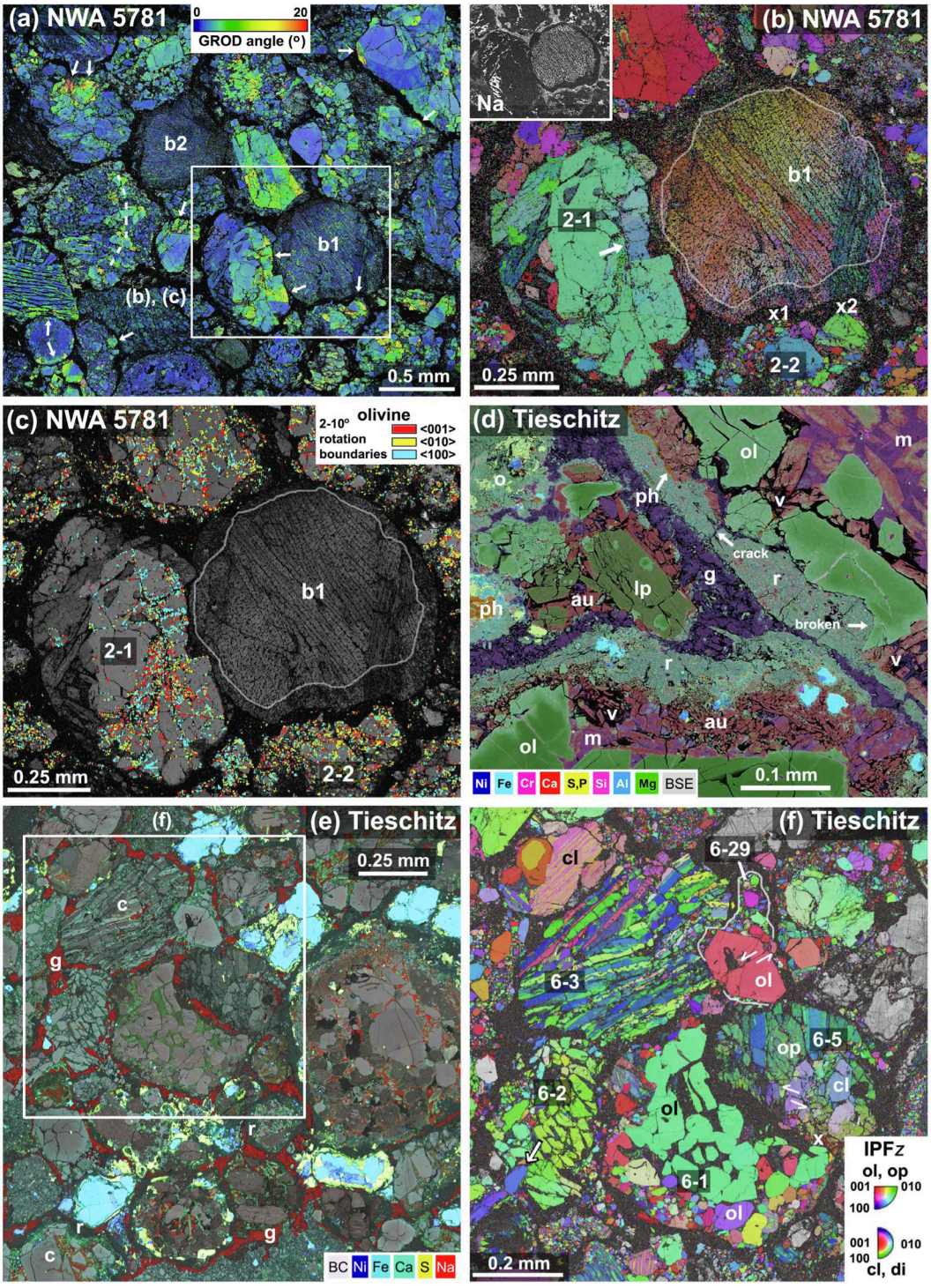

(caption on next page)

Fig. 2a-f. Images of strongly clustered lithologies (see also Supplementary Material). Fig. 2a-f. **(a)** NWA 5781 area showing evidence for mutual chondrule deformation, *GROD+BC* overlay (TM2). Extra deformation (green, yellow, orange colors) occurs at apparent impingement points between chondrules (arrows). A throughgoing deformation zone occurs (dashed) in a chondrule at left. b1 and b2 are two "bleached" chondrules. **(b)** NWA 5781 closeup of bleached Chondrule b1 (bleached margin indicated) and adjacent Chrondrules 2-1 and 2-2, *IPFz+BC* overlay, (TM2, see Fig. 2a for context). The *IPFz* legend is the same as in Fig. 2f. "x1" and "x2" are apparent impingement points betewen Chondrules b1 and 2-2 that caused the bleached zone to be indented. **(c)** NWA 5781, *GB+SB+BC* overlay for olivine, showing misorientation boundaries (subgrain boundaries) with different crystal rotation axis directions in an olivine crystal frame (same area as Fig. 2b). Colors represent different rotation directions (light blue = <100>, yellow = <010>, red = <001>). **(d)** Tieschitz interchondrule region and adjacent chondrules, *EDS+BSE* overlay. Features include interchondrule glass ("g"), fine-grained rim material ("r"), interchondrule pocket ("o"), marginal chondrule mesostasis zones containing voids ("v") and augite ("au"), normal chondrule mesostases ("m"), low-Ca pyroxene ("lp"), olivine ("ol"), phosphate ("ph"), and metal (light blue). Small bits of material similar in composition to fine grained rim (green) occur within interchondrule glass. **(e)** Tieschitz area with typical texture, *EDS+BC* overlay (TM6). Na-glass (red) sometimes occurs inside chondrules but also forms interchondrule glass deposits between chondrules and isolated grains. Two chondrules contain Na-glass in chondrule cores ("c") and have Na-depleted, more calcic mesostases (green) towards chondrule margins. **(f)** Tieschitz area showing conforming objects with evidence for mutual deformation, *IPFz+BC* overlay (TM6, see Fig. 2e for context). Chondrule 6-3 with parallel olivine and pyroxene bars has been partly crushed, misorientating crystals, against a small chondrule (6-29, outlined) with an euhedral olivine crystal that has been microfaulted (arrows give sense of displacement along the fault). Chondrule 6-1 has a core consisting of olivine of one orientation (*IPFz*-green) and a granular olivine rim that has been removed against fragmented and deformed pyroxene-rich fragment 6-5; an impingement point ("x") in 6-5 is inferred from where orthopyroxene has been deformed. Clinoenstatite in 6-5 was microfaulted (arrows give sense of displacement). Chondrule 6-2 consists largely of olivine with similar but slightly variable *IPF* colors (*IPFz* green to green-yellow), evidence it has been misoriented. An olivine crystal from outside the object projects partly into 6-2 (arrow).Fig. 2. Images of strongly clustered lithologies, continued (see also Supplementary Material).

Jelinek (1981).

3. Results

Chondrite textures and features are reported in Sec. 3.1, large-scale metrics for texture and deformation in Sec. 3.2-3.4, microtomography data in Sec. 3.5, small-scale deformation features in high-resolution maps in Sec. 3.6, and the compositions of some chondrite constituents in Sec. 3.7. Table 2 provides metrics for large-scale features in different lithologies of the Type 3 chondrites of this study based on optical microscopy and *LAM* and *miniLAM* EBSD maps, including cluster texture strengths, shock stages, and averaged EBSD deformation parameters.

3.1. Type 3 chondrite textures and features

Figs. 1-3 portray different aspects of the textures, crystallography, and deformation of the chondrites that were studied. We identify different lithologies based on differences in texture and petrographic type (Sec. 3.1.1), features characteristic of chondritic clasts with strongly- or moderately-clustered lithologies (Sec. 3.1.2), features characteristic of chondritic clastic material with weakly clustered lithologies (Sec.3.1.3), features present in both strongly- and weakly-clustered lithologies (Sec. 3.1.4), and features unique to the more heavily shocked (mainly S4—MBD, 2023) NWA 11351 (Sec. 3.1.5). A more detailed narrative for these topics, with each lithology discussed separately, is given in Appendix A, Supplementary Material.

3.1.1. Overall texture and cluster texture strength

Binocular transmitted light images of the various Type 3 chondrites studied illustrate overall chondrite textures and are shown in Fig. 1. Some meteorites have a single lithology that can be reasonably characterized by one cluster texture strength value (C_s value, see Eq. [1]), including Ragland (Fig. 1a), NWA 5781 (Fig. 1b), Tieschitz (Fig. 1c), and NWA 5421 (Fig. 1d) (Table 2). In our samples of these meteorites, the lithologies are >2 cm across and relatively uniform.

Other meteorites have multiple lithologies characterized by different textures and/or C_s values, including NWA 5205 (Fig. 1e), NWA 11905 (Fig. 1f), and NWA 11351 (Fig. 1g). For these meteorites, Type 3 chondritic clasts with an opaque matrix in transmitted light (here designated as Lithology A) occur within Type 3 hosts that have less opaque matrix and that are more clastic (here designated as Lithology B) (Fig. 1e-g). A similar description was given by Metzler (2012) who described chondritic clasts within chondritic host breccias. Besides Type 3 lithologies, two meteorites also contain lithologies with more metamorphosed material. NWA 11905 has clasts of Type 5 material (Lithology C, Fig. 1f), and NWA 11351 contains a clast that itself is a breccia dominated by Type 5 and 6 material (Lithology C, only a thin portion of this is visible in Fig. 1g). The presence of Lithology A as clasts in these meteorites is confirmed by observations of hand specimens and multiple thin sections. More specifically, observations indicate that: (1) Lithology A in NWA 5205 forms a clast up to 2-3 cm across within Lithology B; (2) Lithology A in NWA 11315 forms a lenticular (or lens-shaped) clast with maximum thickness of ~1-2 cm sandwiched between two other lithologies (B and C); (3) Lithology A in multiple samples of NWA 11905 forms clasts up to, but often smaller than, ~2-3 cm across within Lithology B. This is consistent with Metzler (2012), who found that Lithology A-type clasts can range up to at least 10 cm across. In two of the meteorites (NWA 5205 and NWA 11351), the lithologies with opaque matrix (Lithology A) also have higher C_s values than the hosts (Lithology B), whereas in NWA 11905, the apparent C_s values are similar (Table 2). However, as explained in Appendix A, Supplementary Material, the C_s value for Lithology A in NWA 11905 may be an underestimate of cluster texture strength, which would indicate that Lithology A materials all are more strongly clustered than Lithology B hosts.

Meteorites with "strongly clustered lithologies", which have the highest C_s values and appear clustered with optical microscopy (Fig. 1), are NWA 5781 (C_s =0.425), Tieschitz (0.447), NWA 5421 (0.662), Lithology A of NWA 5205 (0.566), and Lithology A of NWA 11351 (0.688). Meteorites with "weakly clustered lithologies" and which appear not very clustered in Fig. 1, include Ragland (C_s = 0.160), Lithology B of NWA 5205 (0.126), and Lithology B of NWA 11351 (0.067). Lithology A and B of NWA 11905 have intermediate C_s values (0.239 and 0.287, respectively) and can be considered "moderately clustered lithologies".

3.1.2. Chondritic clasts with strong or moderate clustering texture

In all the strongly clustered lithologies except NWA 11351 Lithology A, EBSD data provide good evidence for nearly *in situ* impingement deformation effects between neighboring chondrules, though not every neighboring chondrule shows such deformation. *In situ* impingement deformation is specifically inferred for NWA 5781 (Fig. 2a-c), Tieschitz (Fig. 2f), NWA 5421 (Fig. 2j-k), and NWA 5205 Lithology A (Fig. 3a-e). For example, in NWA 5781, there is extra deformation (i.e., more misorientation) at the edge of a chondrule (2-1) with a large olivine grain where it abuts against a pyroxene-rich chondrule (b1) (Fig. 2a-b). The deformation resulted in a variety of subgrain boundaries in the large olivine that have different misorientation rotation axis directions (Fig. 2c). Similarly, in NWA 5421, there is extra deformation at the edges of adjacent chondrules (Fig. 2i-j). Most obvious is deformation in a pyroxene-rich chondrule (1-2) that was caused by the impingement of a fine-grained olivine-rich object (1-1), which caused partial breaking of Chondrule 1-2 (Fig. 2i) and misorientation of olivine bars within it (Fig. 2k). Similarly, in the moderately clustered lithologies in NWA 11905, there is extra deformation at the edges of chondrules and

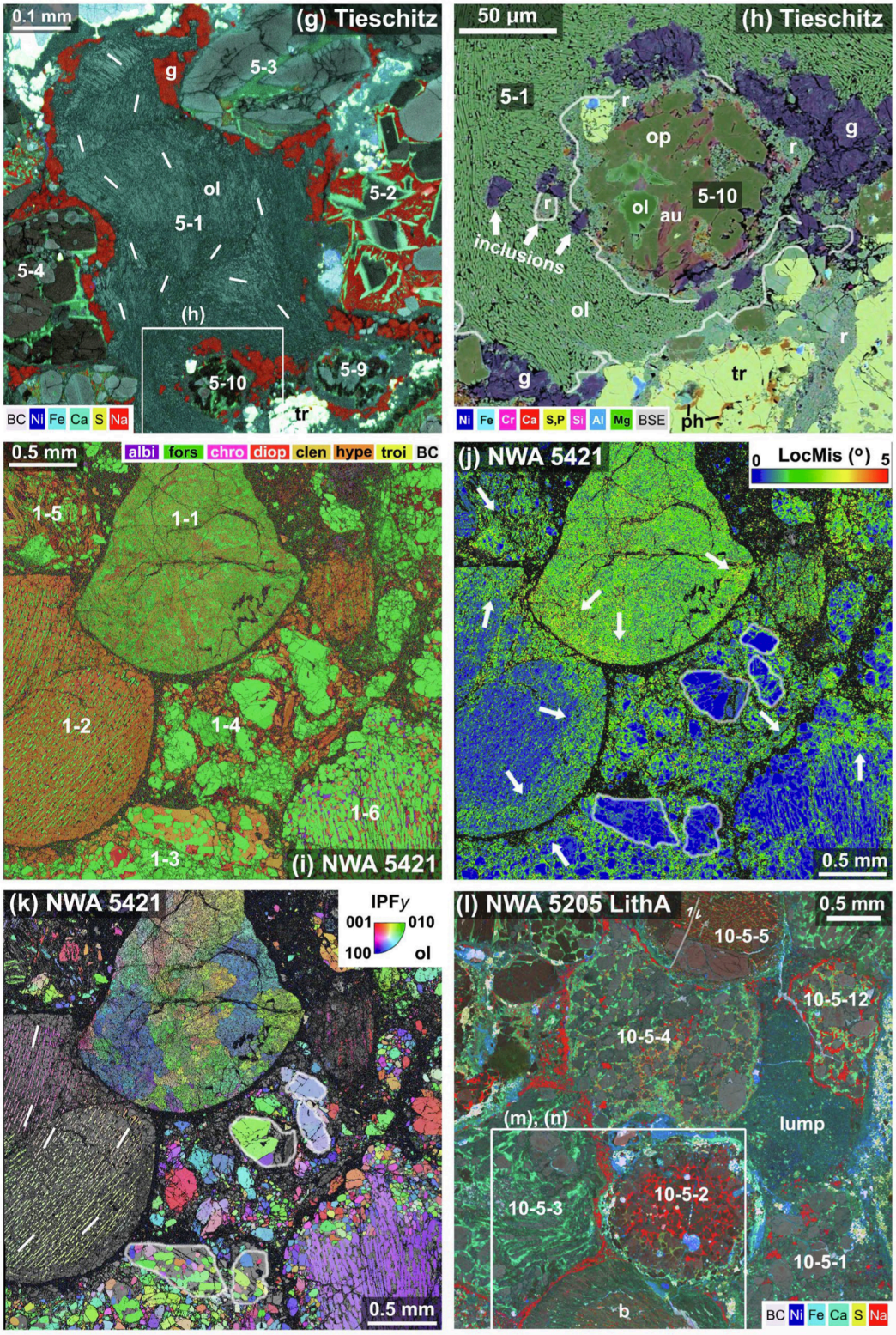

Fig. 2g-l. **(g)** Tieschitz, centered on olivine pocket 5-1, *EDS+BC* overlay (TM5). 5-1 is composed chiefly of rod-shaped olivine crystallites; lines show trends of their long axes. Na-rich glass (red) occurs as interchondrule glass between chondrules and the pocket, as inclusions in the pocket, and as mesostasis in Chondrule 5-2. **(h)** Tieschitz, edge of olivine pocket 5-1, *EDS+BSE* overlay (see Fig. 2g for context). Olivine in 5-1 has inclusions of interchondrule glass ("g") and fine-grained rim ("r") (arrows) and appears to engulf Chondrule 5-10, including its fine-grained rim ("r"). Similar rim material also surrounds and is intergrown with troilite ("tr", yellow-green) and minor phosphate ("ph", orange) at bottom. ol = olivine, op = orthopyroxene, au = augite. Phase colors as in Fig. 2d. **(i, j, k)** NWA 5421 area showing highly conforming chondrules (TM1). Part (i) shows a *Phases+BC* overlay; part (j) a *LocMis+BC* overlay, where arrows indicate extra deformation at chondrule edges; and part (k) shows an *IPFy+BC* overlay for olivine, where line segments in Chondrule 1-2 indicate the trend of olivine grains. In parts (j) and (k), outlines in Chondrules 1-3 and 1-4 indicate relatively low-deformation regions amidst more deformed. **(l)** NWA 5205 Lithology A, typical area, *EDS+BC* overlay (TM10-5). Na-rich glass (red) occurs within some chondrules (notably 10-5-2), and in places as interchondrule glass, and is absent in some chondrules (10-5-3). A fine-grained matrix-like lump is present. A microfault cuts both interior and rim of Chondrule 10-5-5. "b" indicates a bleached chondrule. Fig. 2. Images of strongly clustered

lithologies, concluded (see also Supplementary Material). Fig. 2m-r. **(m)** NWA 5205 Lithology A, closeup of bleached chondrule and adjacent chondrules, *EDS* Na (TM10-5, see Fig. 2l for context). Note Na-rich interchondrule glass is missing in the indented area between the bleached chondrule and 10-5-2 (right arrow), and that some Na-glass occurs in the bleached zone at left. **(n)** NWA 5205 Lithology A, *KAM+BC* overlay (same area as Fig. 2m). The bleached margin of the pyroxene-rich chondrule has more deformation than the underlying core. 10-5-2 contains a deformed relict olivine grain (arrow); 10-5-3 is deformed throughout. **(o)** NWA 5205 Lithology A showing interchondrule glass wedge, *EDS* (TM4). Fine-grained rim ("r") material is locally present on chondrules and as inclusions in the glass wedge. EBSD-verified phases include glass ("g", purple), which occurs in interchondrule regions as well as in the chondrule at right, plagioclase ("pl", purple) in the chondrule above and below, olivine ("ol", green), orthopyroxene ("op", tan), clinoenstatite ("cl", tan), augite ("au", red-tan), and chromite ("cr"). **(p)** NWA 5205 Lithology A, closeup of interchondrule glass wedge in Fig. 2o, *EDS+BSE* (see Fig. 2o for context). Glass ("g") with voids ("v") encloses grains of olivine ("ol"), orthopyroxene ("op"), augite ("au"), and rounded patches of chondrule rim ("r") material. **(q)** NWA 11351 Lithology A, representative area, *EDS+BC* overlay (TM1). Coarser troilite ("tr", greenish yellow), intergrown with smaller amounts of metal ("bcc", blue) and silicates, partly surrounds chondrules and forms veins between chondrules. Na-rich glass (red) mostly occurs within chondrule mesostases but some is present in matrix as patches associated with olivine-like material to form "spotted matrix", too small to see well here, but which is present on the magnesian edge (black) of a pyroxene rich chondrule (right side of "p") with Ca-pyroxene in its core (green). Pyroxene-rich chondrule "b" has some Na-glass in its core and a Na-poor margin and is "bleached". **(r)** NWA 11351 Lithology A, centered on spotted matrix (TM1N). Olivine *IPFx+BC* overlay (left) shows indexed olivine in chondrules but very little in the matrix area near center which appears black. Closeup *EDS+BSE* overlay (right) shows matrix consists mainly of feldspathic ("f", purple) and olivine-like ("o", green) material; one ring of indexed olivine ("ol") occurs in the matrix and is a bit smoother than non-indexing matrix olivine. "p" is low-Ca pyroxene in an adjacent chondrule.

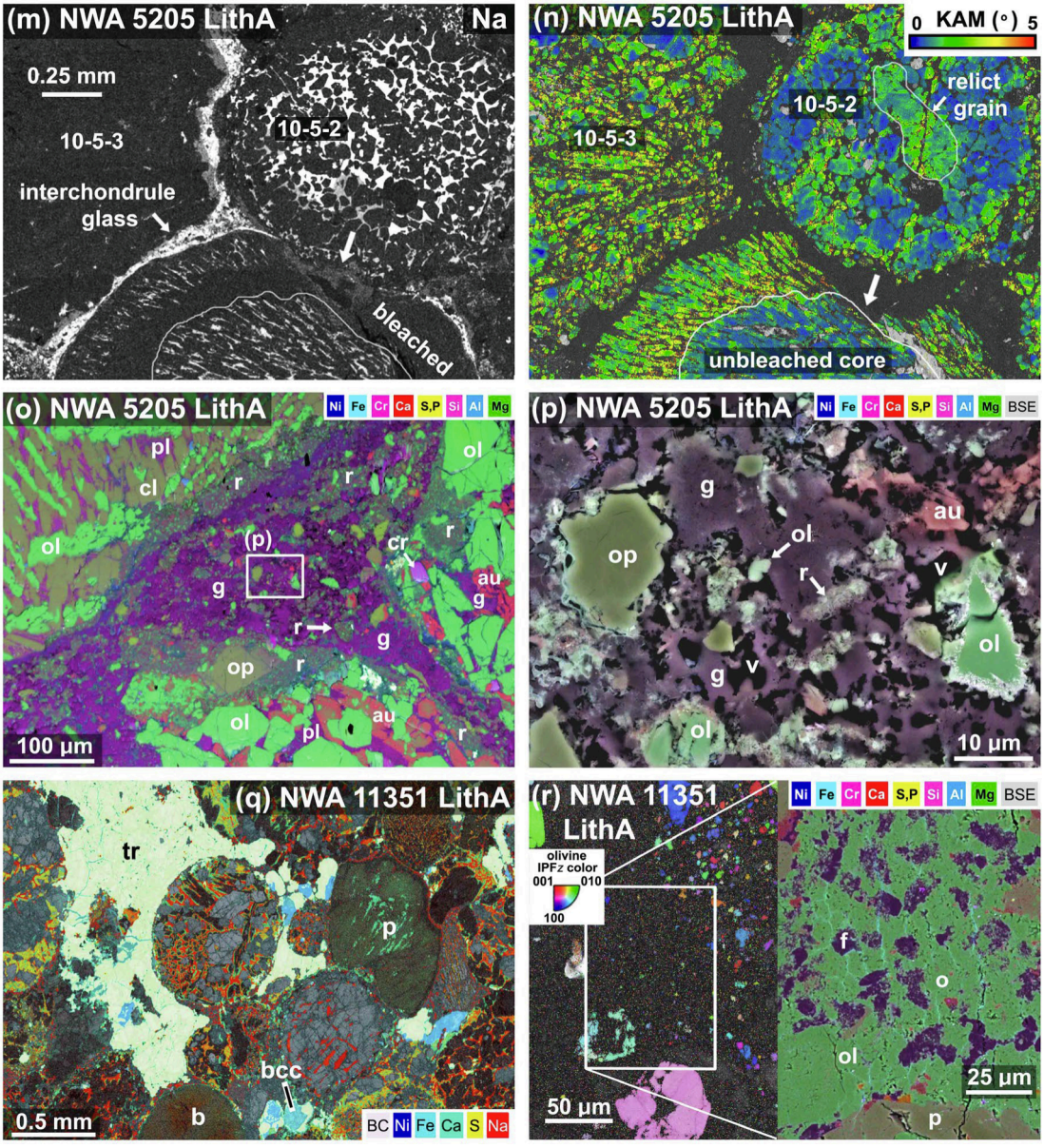

Fig. 2g-l. (*continued*).

fragments in both Lithology A and B (Fig. 3b). A fine-grained olivine-rich object in Lithology A at the margin of Lithology B has extra deformation adjacent to the contact than farther from it (Fig. 3c-e). A deformation map (*GOS*) shows that olivine in this object is strongly deformed ($GOS_{d\geq 10}$ ~4-10° and up to 13°) within ~0.5 mm of the contact with Lithology B, and much less deformed ($GOS_{d\geq 10} \leq 3°$) farther from the contact (Fig. 3d). This large difference in *GOS* does not correspond to the overall 3D orientations of the olivine grains as given in the

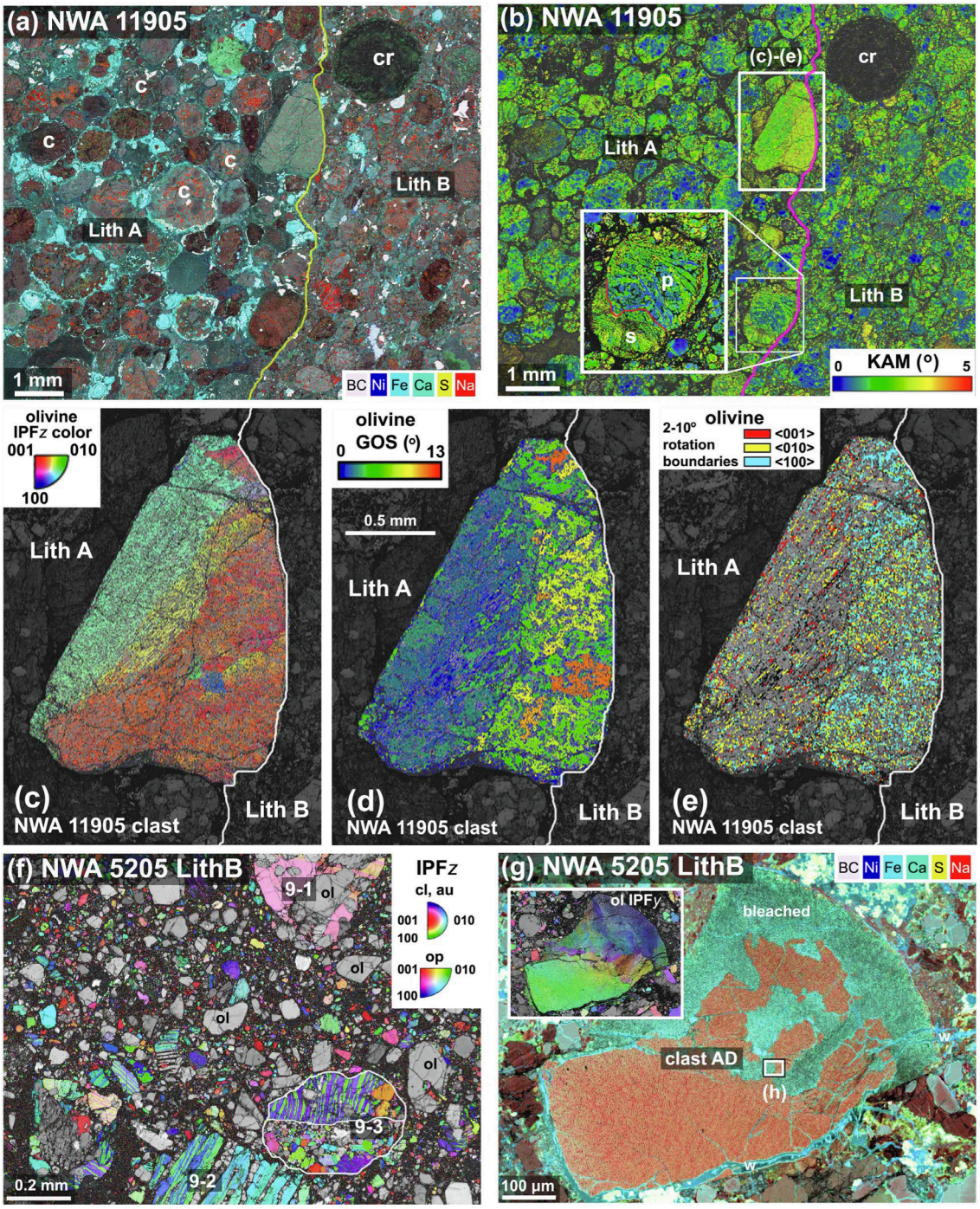

Fig. 3a-g. Images of moderately and weakly clustered lithologies (see also Supplementary Material). Fig. 3a-g. **(a)** NWA 11905, *EDS+BC* overlay (LAM). A sharp contact (line) separates Lithology (Lith.) A (left) from Lith. B, with Lith. A having better distinction of interchondrule areas that are Fe-rich (light blue = metal, white = troilite). Na-rich glass (red) in both lithologies resides mostly within chondrules although it forms smaller patches within Lith. B (difficult to see at this scale). In some chondrules in Lith. A, Na-glass is concentrated in chondrule cores (c) and grades into more Ca-pyroxene (green)-rich margins. cr = large pyroxene-rich cryptocrystalline chondrule. **(b)** NWA 11905, *KAM+BC* overlay (LAM, same area as Fig. 3a). Deformation in both lithologies is often concentrated at grain and chondrule edges (light green-yellow), leaving the cores of larger grains relatively low in deformation (blue). A compound chondrule in Lithology A is shown in the inset and has a larger part (p) and a smaller part (s). **(c, d, e)** Fine-grained olivine-rich object subset data for olivine (LAM, see Fig. 3b for context). Part (c) shows an *IPFz+BC* overlay, part (d) a *GOS+BC* overlay, and part (e) an *GB+SB+BC* overlay. Grains closer to the edge of the melt object adjacent to the Lithology A-B contact have higher *GOS* values (part (d)), and more <100> (light blue) rotation axes than farther from the contact where there are more <001> and <010> rotations (red and yellow, part (e)). **(f)** NWA 5205 Lithology B, *IPFz+BC* overlay (TM9). Pyroxene is shown as colored grains and most of the non-colored grains are olivine. Clinoenstatite has bent twins in lithic Clast 9-3, an apparent compound object with mainly clinoenstatite at top and orthopyroxene below. **(g)** NWA 5025 Lithology B, *EDS+BC* overlay (TM2). Image is centered on Clast AD, a fine-grained olivine-rich clast. The inset shows an olivine *IPFy* map of the same area (legend same as in Fig. 2k). Clast AD has an irregularly shaped interior with elevated Na and appears orange, the exterior is "bleached" with lower Na and higher Fe and Ca contents and appears blue-green. This chemistry does not correspond precisely to the orientations of olivine crystallites as given in the *IPF* map. Terrestrial weathering veins ("w", bottom) cross cut both bleached and Na-rich zones. Fig. 3. Images of moderately and weakly clustered lithologies, concluded (see also Supplementary Material).

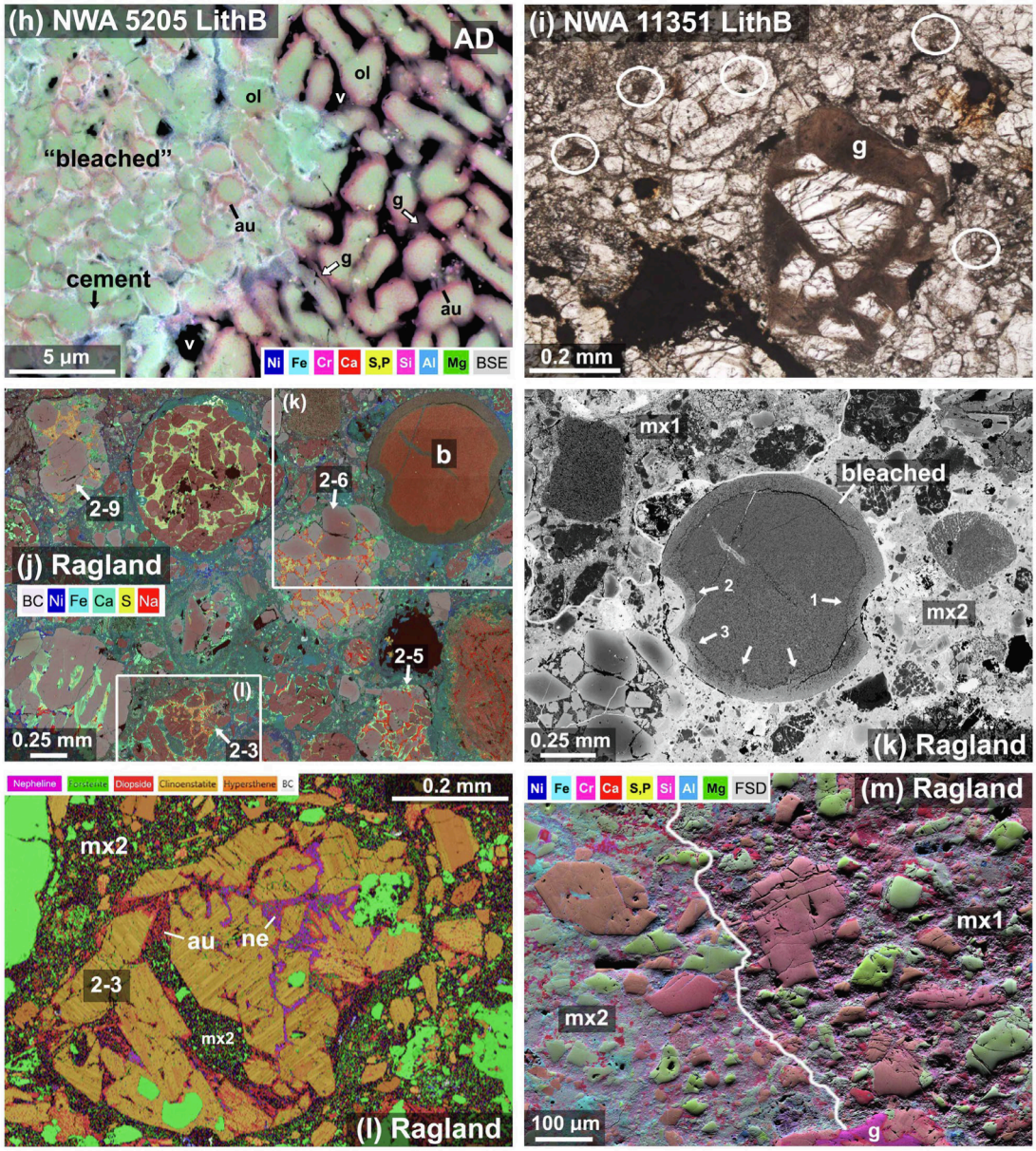

Fig. 3h-m. **(h)** NWA 5205 Lithology B, closeup of clast AD at contact between bleached zone at left and non-bleached at right, *EDS+BSE* overlay (see Fig. 3g for context). ol = olivine crystallites, au = augite, g = glass, v = voids. **(i)** NWA 11351 Lithology B, plane-polarized transmitted light image, showing turbid glass ("g") in mesostases and between grains (circled). **(j)** Ragland, *EDS+BC* overlay (TM2). Area exhibits weak cluster texture with a variety of chondrule types, including a bleached cryptocrystalline chondrule ("b"), Chondrules 2-6 and 2-9 which contain Na-rich glass (red) in the core and more calcic mesostasis towards their edges (green), and Chondrule 2-5 with Na-rich glass (red) right up to an apparently broken edge at left and right. **(k)** Ragland, *BSE* image of bleached chondrule with three indentation points (1, 2, 3) (see Fig. 3j for context). "mx1" and "mx2" are two different matrix types. **(l)** Ragland, *Phases+BC* overlay (TM2, see Fig. 3j for context). Closeup of Chondrule 2-3, a fragment that contains EBSD-indexed nepheline ("ne", purple) and augite ("au", red) in a mesostasis between pyroxene phenocrysts composed chiefly of clinoenstatite (pale orange), orthopyroxene (dark orange), and olivine (green). Matrix type 2 ("mx2") surrounds the fragment and occurs within the chondrule. Mesostasis grades in composition from nepheline + augite to augite + voids (black) towards the fragment edge. **(m)** Ragland, *EDS+FSD* overlay (TM6). Contact between two matrix types "mx1" and "mx2"; both contain mineral clasts composed of olivine of different compositions (lighter and darker green) and pyroxene of different compositions (brown, pale orange), but mx1 is rougher and has less interstitial Fe-rich material (blue) than mx2. A chondrule fragment with glass ("g") extending to the fragment edge is at bottom.

IPF map (Fig. 3c). The change in *GOS* values does, however, correspond with a change in misorientation rotation axis directions in olivine (Fig. 3e). Away from the contact, most rotation axis directions are <010> and <001>, whereas close to the contact, most of the rotation axis directions are <100> with a secondary importance for <010> (Fig. 3e).

In NWA 11351 Lithology A, despite high cluster texture strength, impingement deformation effects are less apparent, possibly because the meteorite is more strongly deformed throughout.

The most strongly clustered lithologies, except for NWA 11315 Lithology A, also contain interchondrule feldspathic glass between chondrules and large metal-sulfide aggregates. The glass is exclusively present as a discrete deposit in the strongly clustered lithologies of Tieschitz (Fig. 2d-e), NWA 5421, and NWA 5205 Lithology A (Fig. 2l, 2o-p). This glass is Na-rich (Fig. 2e, 2g, 2l-m). It is identified as glass because it shows no significant crystallinity with EBSD methods (it has low Band Contrast) and it appears essentially isotropic with optical microscopy. However, high-magnification *BSE* and *EDS* reveal small-

Table 2
Chondrite cluster texture and olivine grain size and deformation data for Type 3 ordinary chondrites based on optical microscopy and EBSD Large Area Map (LAM, map areas >52 mm^2) and mini-LAM (map areas 5-36 mm^2) data. EBSD parameters include grain size *d*[6], Grain Orientation Spread *GOS*[7], *GOS* skewness *Sk*[8], and misorientation rotation axis parameters $R_{0.5\text{-}2}$ *and* $R_{2\text{-}10}$ [10]. *GOS*, *Sk*, and *R* values represent map-area-averaged data. Lith. = lithology.

	NWA 5781	NWA 11351 Lith. A	NWA 11351 Lith. B	Tieschitz	NWA 5421	NWA 5205 Lith. A	NWA 5205 Lith. B	NWA 11905 Lith. A	NWA 11905 Lith. B	Ragland
Cluster texture										
C_s [1]	0.425	0.688	0.067	0.447	0.662	0.566	0.126	0.239	0.287	0.160
Olivine										
N [2]	156	67	79	145	144	117	120	53	102	95
CSS [3]	S3	S4	S4	S1	S2	S2	S2	S4	S3	S1
WSS [4]	2.57±0.96	3.76±0.76	3.87±0.81	1.50±0.76	1.75±0.84	2.30±1.10	1.97±0.94	2.42±1.17	2.46±1.01	1.13±0.39
EBSD maps averaged	LAM, TM2	LAM, TM1, TM2	LAM, TM2	LAM1, LAM2, TM1, TM3	LAM, TM1	LAM, TM1, TM5, TM10-1, TM10-4, TM10-5, TM10-6	LAM, TM7	LAM1	LAM1	LAM, TM2
Map area (mm^2) [5]	108.26	89.39	30.10	139.31	94.18	255.45	58.05	60.00	61.78	134.83
d, d>50 [6]	90.4±55.8 (1517)	89.1±53.9 (1373)	84.0±46.9 (1314)	94.2±56.5 (2757)	87.6±49.6 (1888)	86.7±49.3 (5422)	79.9±40.7 (927)	86.8±49.2 (912)	81.9±41.0 (833)	86.9±49.6 (1776)
d, d=15-50 [6]	24.0±8.2 (20246)	24.0±8.2 (9720)	23.9±8.2 (11454)	24.6±8.6 (15585)	24.6±8.6 (11133)	25.0±8.8 (31744)	24.3±8.3 (8304)	24.7±8.6 (5221)	24.3±8.3 (7054)	24.8±8.7 (10611)
d, d=5-15 [6]	11.4±1.7 (24200)	9.9±2.0 (31217)	10.9±1.8 (22912)	10.9±1.8 (32662)	11.2±1.7 (23666)	10.4±1.8 (94468)	12.0±1.4 (13851)	11.9±1.6 (6801)	11.8±1.6 (10267)	11.3±1.7 (19336)
$GOS_{d>50}$ (°) [6,7]	2.41±1.61 (0.59)	3.56±1.67 (0.86)	3.78±1.72 (0.92)	1.56±1.86 (0.38)	2.67±2.02 (0.65)	2.69±2.06 (0.65)	1.82±1.60 (0.44)	2.63±2.25 (0.64)	2.60±2.27 (0.63)	1.00±1.12 (0.24)
$GOS_{d15\text{-}50}$ (°) [6,7]	2.00±1.49 (0.37)	3.15±1.67 (0.59)	3.53±1.75 (0.66)	1.59±1.79 (0.30)	2.62±1.98 (0.49)	2.37±1.88 (0.44)	1.80±1.54 (0.34)	2.30±2.19 (0.43)	2.38±2.16 (0.44)	0.95±1.06 (0.18)
$GOS_{d5\text{-}15}$ (°) [6,7]	1.64±1.35 (0.36)	2.65±1.54 (0.58)	3.26±1.73 (0.71)	1.45±1.69 (0.32)	2.49±1.94 (0.54)	1.90±1.62 (0.41)	1.76±1.53 (0.38)	2.43±2.22 (0.53)	2.36±2.06 (0.51)	0.99±1.19 (0.22)
$Sk_{d>50}$ [6,8]	1.24 (0.04)	1.10 (0.04)	1.10 (0.04)	1.98 (0.07)	1.24 (0.04)	1.28 (0.04)	1.41 (0.05)	1.44 (0.05)	1.33 (0.04)	1.79 (0.06)
$Sk_{d15\text{-}50}$ [6,8]	1.28 (0.05)	1.12 (0.04)	1.11 (0.04)	1.89 (0.07)	1.24 (0.05)	1.31 (0.05)	1.38 (0.05)	1.54 (0.06)	1.41 (0.05)	1.86 (0.07)
$Sk_{d5\text{-}15}$ [6,8]	1.34 (0.05)	1.14 (0.04)	1.11 (0.04)	2.19 (0.08)	1.25 (0.05)	1.36 (0.05)	1.39 (0.05)	1.49 (0.05)	1.39 (0.05)	2.03 (0.07)
$Sk_{d>50}/Sk_{d5\text{-}15}$ [6,8]	0.928 (0.051)	0.970 (0.054)	0.988 (0.055)	0.904 (0.050)	0.992 (0.055)	0.943 (0.052)	1.013 (0.056)	0.963 (0.053)	0.953 (0.053)	0.905 (0.050)
$Sk_{d15\text{-}50}/Sk_{d5\text{-}15}$ [6,8]	0.953 (0.052)	0.985 (0.054)	0.989 (0.054)	1.047 (0.057)	1.003 (0.055)	0.980 (0.054)	1.022 (0.056)	0.935 (0.051)	0.945 (0.052)	0.993 (0.054)
N_p (0.5-2) [9]	1407178	382228	913152	2732050	963926	6377999	512162	364887	363683	1035835
N_p (2-10) [9]	521295	1080078	526871	450007	647591	1816999	188414	154926	164615	204979
$R_{0.5\text{-}2}$ [10]	0.623 (0.049)	0.475 (0.037)	0.440 (0.034)	0.601 (0.047)	0.592 (0.046)	0.630 (0.049)	0.612 (0.048)	0.660 (0.051)	0.653 (0.051)	0.624 (0.049)
$R_{2\text{-}10}$ [10]	0.604 (0.023)	0.412 (0.016)	0.414 (0.016)	0.640 (0.024)	0.616 (0.024)	0.628 (0.024)	0.624 (0.024)	0.649 (0.025)	0.614 (0.023)	0.611 (0.023)
T_{deform} (°C) [11]	924±89	714±99	716±99	963±87	937±89	950±88	946±88	973±87	934±89	931±89

[1] C_s = cluster texture strength = fraction of chondrule boundaries that conform to their neighbors, based on optical microscopy (transmitted light binocular micrographs). [2] Number of grains used for shock stage analysis. [3] CSS = conventional shock stage (Stöffler et al., 1991, 2018, 2019) based on optical microscopy for larger (mainly d>50 μm) olivine grains. [4] WSS = weighted shock stage (Jamsja and Ruzicka, 2010) represents the mean and ±1 standard deviation of shock stage for larger olivine grains based on optical microscopy. [5] Total map area of averaged EBSD data. [6] d = EBSD equivalent grain size in μm, the diameter of a circular grain with the same area as measured, in three different grain size bins (for d>50, d=15-50, and d=5-15); values outside the parentheses are mean ± standard deviation, and values in parentheses are the number of grains (N_g). [7] Grain Orientation Spread (GOS) represents the mean angular lattice misorientation within grains, in three different grain size bins; values outside parentheses are mean ± standard deviation of all grains; values in parentheses are representative ±1σ errors (see Text). [8] GOS skewness Sk = (mean GOS)/(median GOS), for three different grain size bins; values in parentheses are representative ±1σ errors. GOS skewness ratios for different grain sizes ($Sk_{d>50}/Sk_{d5\text{-}15}$ and $Sk_{d15\text{-}50}/Sk_{d5\text{-}15}$) are relevant for assessing post-deformation dislocation recovery and annealing, with $Sk_{d>50}/Sk_{d5\text{-}15}$ being the primary annealing metric; values in parentheses are representative ±1σ errors (see Text). [9] N_p =number of pixels with 0.5-2 and 2-10 misorientation rotations that were counted to determine values for the R parameters. [10] Misorientation rotation axis parameter $R_j = (f_{001}+f_{010})/(f_{100}+f_{001}+f_{010})$, where j = 0-5-2° or 2-10° rotation misorientations, and f_i = fraction of misorientation rotation axis directions in the *ith* crystal direction of olivine, determined from Crystal Rotation Axis (CRA) plots using 25° half width contouring; values in parentheses are representative ±1σ errors (see Text). R-parameter is relevant for assessing slip directions of dislocation slip systems and relative deformation temperature (see Text). [11] T_{deform} = model deformation temperature and estimated uncertainty, based on map-averaged $R_{2\text{-}10}$ values, assuming that temperature is the primary control on slip systems (see Text).

scale variations and potential partial crystallinity. Further, the glass may be essentially identical to what has been termed "white matrix" in Tieschitz that is at least partially crystalline on a TEM and larger scale (Ashworth, 1981; Alexander et al., 1989; Hutchison et al., 1998).

The interchondrule glass forms bands between chondrules, or triangular wedge-shaped pockets when it occurs between three intersecting objects (Fig. 2d-e, 2l, 2o-p). The glass bands are not of uniform thickness but rather pinch out in places (Fig. 2d-e, 2g, 2l-m). The glass deposits can contain irregularly shaped and apparently clastic grains of olivine, orthopyroxene, augite, and rounded inclusions of fine-grained chondrule rim material (Fig. 2o-p). The glass can be highly vuggy (Fig. 2p). Some of the vugs have rounded edges, but in many places they have highly irregular margins, presenting an "etched" appearance (Fig. 2p). "Etching" is most pronounced against glass.

Although this glass is only present in strongly clustered lithologies, it is not present in NWA 11351 Lithology A that has the strongest cluster texture, nor is it present in NWA 5781, which has a cluster texture nearly as strong as Tieschitz. Possibly this is because of later destruction by one or more impact events associated with the S4 (NWA 11351) or S3 (NWA 5781) shock stages of these meteorites.

Chondrules in strongly- and moderately-clustered lithologies, except for NWA 11351 Lithology A, best show the presence of fine-grained ferromagnesian rims on chondrules. Fine-grained rims typically have grains too small (<1 μm across) to discern clearly at typical SEM magnification but sometimes are coarser grained ("medium grained"). They sometimes overlie broken chondrule margins (Fig. 2d), indicating rimming following deformation.

3.1.3. Clastic material with weak clustering texture

Weakly clustered lithologies such as NWA 5205 Lithology B, NWA 11351 Lithology B, and Ragland exhibit significant clastic texture. NWA 5205 Lithology B contains only small chondrules (Fig. 1e) and has many lithic and mineral clasts, including some clasts that themselves contain clasts (Fig. 3f). Matrix is almost indistinguishable in NWA 11351 Lithology B which is dominated by fragmental material (Fig. 1g, 3i). Ragland has a more distinguishable chondrule-matrix texture (Fig. 1a, 3j) but contains many chondrule fragments (Fig. 3k-l) as well as abundant matrix that is dominated by mineral clasts of olivine and pyroxene (Fig. 3m). In Ragland there are two matrix types that have relatively sharp contacts. One type, "Matrix 1", has a notably rougher texture; the other, "Matrix 2", has more fine-grained material and appears smoother (Fig. 3k, 3m). Matrix 1 is enriched in Na and K and depleted in Fe and Ni compared to Matrix 2 (Fig. 3m). Matrix 1 appears to form clasts within Matrix 2, but this could simply indicate that Matrix 2 is more prevalent.

Impingement effects can be inferred for chondrules in weakly clustered lithologies (NWA 5205 Lithology B, NWA 11351 Lithology B) based on additional deformation observed on the margins of some chondrule boundaries. However, with lower cluster texture strengths it is not obvious that such deformation is the result of mutual impingement between chondrules.

3.1.4. Features found in both strongly- and weakly-clustered lithologies

Some features found in both strongly- and weakly-clustered lithologies are described here because they may have implications for accretion or subsequent processes. This includes the presence of fine-grained olivine-rich objects, and bleached chondrules (Grossman et al., 2000).

Fine-grained to cryptocrystalline olivine-rich objects are distinctive features in Type 3 ordinary chondrites that have not been widely recognized. In texture they most resemble cryptocrystalline chondrules but are unlike these chemically in being olivine-rich, not pyroxene-rich (Gooding and Keil, 1981). They are igneous-textured, have multiple crystallite orientation domains and high *GOS* values in olivine, and come in different varieties. Examples are in Tieschitz (Fig. 2g-h), NWA 5421 (Fig. 2i-k), NWA 11905 (Fig. 3c-e), and NWA 5205 Lithology B (Fig. 3g-h).

In Tieschitz, fine-grained olivine-rich objects form pockets or lumps interstitial to chondrules. Figure 2g shows one of the most prominent examples (Object 5-1), which is also visible in thin section (Fig. 1c), and Fig. 2h shows the margin of this object and an adjacent small chondrule (5-10). Another pocket is visible in Fig. 2d. Such pockets consist mainly of tabular or acicular olivine crystallites in different orientation domains. In Object 5-1, which is coarser than most, olivine grains are ≤2 μm wide and ~5-50 μm long (Fig. 2h). These crystals are locally aligned and often parallel to the nearest margin of the object (Fig. 2g). Olivine domains in 5-1 have one overall 3D crystal orientation in each domain, although the crystals have some orientation variability in each domain. The pockets conform completely to their surroundings (Fig. 2h), with convex-inwards margins that are defined by surrounding objects. From their textures they appear to have crystallized interstitial to chondrules, between fine-grained rims and interchondrule glass deposits (Fig. 2g-h). The olivine-rich lumps also contain inclusions of interchondrule glass and fine-grained rims (Fig. 2g-h). The observations seem to indicate that they crystallized after the formation of neighboring chondrules, rims, and interchondrule glass.

Object 1-1 in NWA 5421 is another example of a fine-grained olivine rich object (Fig. 2i). This object has strong crystal misorientations (Fig. 2j) and is composed of olivine crystals with various orientation domains (different colors in Fig. 2k). In overall texture, mineralogy, and high deformation character, it resembles the melt clast in the MIL 99301 Type 6 chondrite (Ruzicka and Hugo, 2018). It also resembles the internal texture of olivine-rich pockets in Tieschitz, except it has well-defined, compact, convex-outward margins. Rather than being interstitial to all other materials as for the olivine pockets in Tieschitz, Object 1-1 in NWA 5421 appears to have accreted as a coherent, semi-rigid object that pushed against adjacent chondrules.

Bleached chondrules are chondrules that have less feldspathic glass in their margins than in their interiors, presumably because of removal of glass from the edges (Skinner et al., 1989; Grossman et al., 2000; Kostynick, 2019). This removal could have been caused either by a leaching event involving unspecified fluids (Michel-Levy, 1976), an aqueous fluid (Hutchison et al., 1998; Grossman et al., 2000), or physical movement of chondrule mesostasis melt into matrix during agglomeration (Hutchison et al., 1979, 1998; Hutchison and Bevan, 1983).

Although not all chondrules are bleached, all investigated Type 3 lithologies except NWA 13351 Lithology B contain examples of chondrules that have depletions of Na-feldspathic mesostasis glass in their outer zones, often accompanied by voids. Contrary to earlier indications (Grossman et al., 2000), a variety of chondrule textural types appear to have lost Na-rich mesostases from their peripheries, including:

- cryptocrystalline chondrules (Chondrule b in Fig. 3j-k; Chondrule b in Fig. 2q);
- radial pyroxene chondrules (Chondrule p in Fig. 3q);
- fine-grained pyroxene-rich chondrules that are not cryptocrystalline nor classic radial pyroxene texture (Chondrule b1 in Fig. 2a-c);
- barred pyroxene chondrules (Chondrule b in Fig. 2l-n);
- barred pyroxene-olivine chondrules (Chondrule 6-3 in Fig. 2e-f);
- olivine microporphyritic chondrules (the two largest chondrules visible in Fig. 2d; Chondrule 10-5-2 in Fig. 2l-m; Chondrules 2-6 and 2-9 in Fig. 3j); and
- fine-grained olivine-rich clasts (Clast AD in Fig. 3g-h).

In microporphyritic chondrules, bleached zones typically contain voids together with an excess of augite crystallites. A variation of bleaching is found in some chondrules from Ragland and Tieschitz, where nepheline in mesostasis takes the place of Na-rich glass, grading into bleached zones that contain augite crystallites and voids (Fig. 3l).

Observations constrain the timing of bleaching relative to deformation. Our data support Grossman et al. (2000) in indicating that bleaching occurred both after and before deformation and further show how bleaching is related to cluster texture. A good example of bleaching after deformation is Chondrule b1 in strongly clustered NWA 5781 (Fig. 2a-c). The bleached zone of b1 conforms to the outline of adjacent Chondrule 2-2 (Fig. 2b-c) and bows inward from two apparent impingement points labeled as x1 and x2 in Fig. 2b. This suggests that the bowing of the margin pre-dated the bleaching, so bleaching post-dated impingement deformation. The *IPF* map in Fig. 2b shows the orientations of grains in the chondrules. In the bleached chondrule (b1), one can see that the orientations of pyroxene grains, given by colors in the *IPF* map, extend across the boundary from the interior through the bleached zone. However, the alignments of pyroxene grains are jogged, both at the edges of the bleached zone at the contact with the interior, and elsewhere within the interior of the chondrule. This jogging could have been created by deformation, or it could have been created by crystallization effects alone. In either case, crystal orientations were jogged before bleaching.

In other cases, there is evidence for multiple episodes of deformation with an intervening bleaching episode. This occurs in both strongly- and weakly-clustered lithologies. For example, in weakly clustered Ragland, a prominent bleached cryptocrystalline pyroxene-rich chondrule has

three indent points where the outer part of the chondrule has been removed to leave hemispherical cavities ("1", "2", "3" in Fig. 3k). At two of these indent points (1, 2), the bleached zone extends inwards, whereas at another (3), there is no change in the inner boundary of the bleached zone (Fig. 3k). This suggests (Grossman et al., 2000) that at points 1 and 2, indentation occurred before bleaching, whereas at point 3, indentation occurred after bleaching. Two other inward deflections of the bleached zone with no outside cavities (arrows in Fig. 3k) may have been caused by early indents that are not evident from the outer boundary of the chondrule.

Similarly, two deformation events with an intervening bleaching episode can be inferred for pyroxene-rich bleached Chondrule b in strongly clustered NWA 5205 Lithology A (Fig. 2l-n). A portion of the bleached rim and adjacent interchondrule glass have been removed where the bleached chondrule abuts neighboring Chondrule 10-5-2 in an apparent indentation location (Fig. 2m). In the deformation map (Fig. 2n), the bleached margin is seen to be heavily deformed, and completely absent adjacent to Chondrule 10-5-2, indicating that it was removed at the indentation location with 10-5-2. The interior of the bleached chondrule is much less deformed (Fig. 2n). The observations and geometry suggest two episodes of deformation: an earlier deformation that coincided with the bleached zone, and a later deformation caused by impingement deformation that partially removed the bleached zone. We speculate the later deformation moved a portion of the missing bleached zone out of the plane of the section to where it is not visible. Microfaulting that displaced material in other chondrules is seen nearby (Fig. 2l) and may have been responsible for this removal.

Finally, a good example of bleaching that pre-dated deformation is given by Clast AD in weakly clustered NWA 5205 Lithology B. This object is a high-*GOS*, fine-grained olivine-rich object with an "inner" portion that contains more Na and K, and an "outer" portion that is depleted in Na and K and enriched in Fe and (at the very edge of the clast) Ca (Fig. 3g). Chemical zones show no obvious relationship with the present edge of the object (Fig. 3g) or with olivine orientation domains (see inset, Fig. 3g). A higher magnification view shows the texture of Clast AD at the contact between inner and outer portions (Fig. 3h). In this area, both sides are composed of olivine crystallites that form short rods (~2 μm wide by ~5 μm long) or spheroids (~2 μm across) that might be rods at high angle to the section, mantled by augite (≤0.5 μm thick) (Fig. 3h). The olivine in both areas has the same 3D crystal orientation and may be part of the same grain (*IPFy* yellow-green color, Fig. 3g inset). Inner and outer parts differ only in their mesostases, with many voids and some feldspathic glass in the inner zone, and areas between olivine and augite in the low-porosity outer zone filled with Fe-rich cement (Fig. 3h). The Fe-rich cement in the bleached zone of the clast is cross-cut by obvious weathering veins (Fig. 3g) and so must have formed before the obvious terrestrial veins. From these observations one can infer that the outer zone is rich in Fe and poor in Na and K because Fe-rich cement has replaced mesostasis voids and small patches of glass in the inner zone during a pre-terrestrial bleaching event. Although the strong deformation recorded by olivine in Clast AD may have occurred early, there is good evidence that bleaching pre-dated the brecciation that produced the present shape of the clast, because both portions were broken during the formation of the clast.

3.1.5. Features found only in NWA 11351

NWA 11351 has some features that are not found in any of the other lithologies, possibly because it is more deformed. This includes coarse troilite in Lithology A that forms elongated patches which partly engulf surrounding chondrules (Fig. 1c, 2q), a "spotted" matrix texture (Fig. 2r), and a near-absence of crystalline plagioclase. Furthermore, the strongly clustered Lithology A in the meteorite differs from other strongly clustered lithologies in lacking interchondrule glass, fine-grained rims, and clear evidence for impingement deformation.

In spotted matrix, best seen in Lithology A, feldspathic material forms irregularly shaped domains ~10-20 μm across within material chemically like olivine (Fig. 2r). However, both the feldspathic and olivine-rich portions of this matrix must be poorly crystalline, as both have low Band Contrast values and neither index well (Fig. 2r). Some grains in matrix, and those within chondrules, do index as olivine (Fig. 2r), suggesting that the non-indexing for matrix "olivine" is not caused by a general analytical problem. Spotted matrix was previously found as a distinctive intergrowth of "albite" and "olivine" in the matrix of three strongly shocked, paired LL3 chondrites from Iran (Lut 005, Lut 006, and Lut 007) (Hutson et al., 2014).

NWA 11351 has notably little plagioclase in any chondrules, in contrast to other Type 3 chondrites that contain some plagioclase-bearing chondrules. Instead, all feldspathic material in NWA 11351, both Lithology A and B, appears to be amorphous, but it is not maskelynite that preserved crystal shapes, but rather turbid, colored glass in chondrule mesostases (Fig. 3i). The abundance of glass is striking as such a feature is more typical of a low-subtype chondrite, but olivine in both Lithology A and B are almost uniform in Fe/Mg unlike what one expects for a low subtype chondrite, and the matrix in Lithology B is not opaque as one expects for a low subtype chondrite (Fig. 1g). These contradictory features result in a hybrid Type 3/4 designation for NWA 11351 Lithology A and B (MBD, 2023).

3.2. Deformation intensity (shock stage and Grain Orientation Spread)

Both shock stage and average *GOS* are measures of overall shock deformation intensity. Here we compare weighted shock stage (*WSS*; Jamsja and Ruzicka, 2010) and conventional shock stage (*CSS;* Stöffler et al., 1991, 2018) based on the optical properties of coarse (roughly > 50 μm across) olivine grains, to average *GOS* values of olivine for different grain sizes (equivalent diameter *d,* in microns). Shock stage and averaged *GOS* data for olivine in Type 3 chondrite lithologies are given in Table 2. The *GOS* values in Table 2 are based on map-area-averaged data obtained with large-area EBSD maps (*LAMs* and *miniLAMs*) to obtain the most representative values.

Fig. S1 (Appendix A, Supplementary Material) shows shock stage histogram data for olivine used to determine the weighted and conventional shock stage. Shock stages vary significantly, from Ragland, for which *WSS* = 1.13±0.39 (mean and standard deviation) and *CSS* = S1, to Lithologies A and B in NWA 11351, for which *WSS* = 3.76±0.76 (*CSS* = S4) and *WSS* = 3.87±0.81 (*CSS* = S4), respectively.

Figure 4 compares average $GOS_{d>50}$ for olivine to weighted shock stage for both the Type 3 chondrite lithologies of this study and Type 6 chondrites studied previously (Ruzicka and Hugo, 2018; Hugo et al., 2020). With the additional data it is now clear that $GOS_{d>50}$ and *WSS* values are well-correlated, with a linear correlation coefficient $r^2 = 0.88$, despite large standard deviation values (Fig. 4). Data for Elbert (LL6) are excluded because olivine in Elbert has been partially recrystallized (Hugo et al., 2020), which has the effect of decreasing mean *GOS* but increasing *WSS* (olivine recrystallization is an S6 characteristic—Jamsja and Ruzicka, 2010; Bischoff et al., 2019). The standard deviation bars tend to be larger for the Type 3 chondrites than for Type 6 chondrites, but for a given chondrite the standard deviations for $GOS_{d>50}$ and *WSS* are similar (Fig. 4). As the *GOS* standard deviations are much larger than the estimated precision for *GOS* determinations (≤0.1-0.2°, Sec. 2), this indicates that intergrain deformation heterogeneity is present for all the chondrites, recorded both by standard deviation in *GOS* and by variations in optical shock stages for different grains. Such deformation heterogeneity is typically larger for Type 3 than for Type 6 chondrites, although some Type 6 chondrites (e.g., Saint-Séverin, Elbert) are also heterogeneous (Fig. 4).

The equation for the least-squares linear regression in Fig. 4 between *WSS* and $GOS_{d>50}$ in olivine is:

$$WSS = 0.352 + 0.866 \times (\text{mean } GOS_{d>50}{}^{\circ}) \quad (4)$$

This implies an almost 1:1 relationship between *WSS* and mean

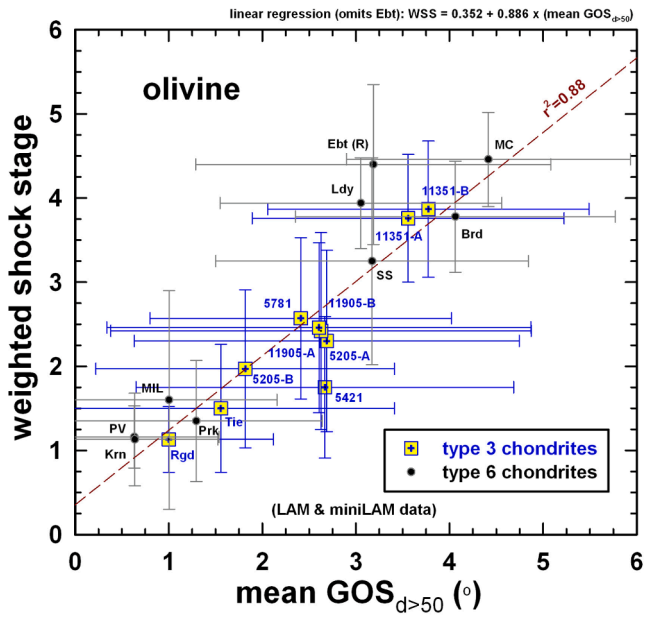

Fig. 4. Olivine deformation comparison between optical microscopy (weighted shock stage) and EBSD (map-area-averaged Grain Orientation Spread, mean $GOS_{d>50}$), for both the Type 3 chondrites of this study, and reference Type 6 chondrites (Ruzicka and Hugo, 2018; Hugo et al., 2020). Points and bars represent mean values and ±1 standard deviation. The linear regression (r^2 = 0.88) excludes partially recrystallized (R) Elbert (LL6) (Hugo et al., 2020). Meteorite abbreviations: Rgd = Ragland; Tie = Tieschitz; 5205-A and 5205-B = NWA 5205 Lithology A and B respectively; 5421 = NWA 5421; 11905-A and 11905-B = NWA 11905 Lithology A and B, respectively; 5781 = NWA 5781; Krn = Kernouvé; PV = Portales Valley; Prk = Park; MIL = MIL 99301; Ldy = Leedey; Brd = Bruderheim; MC = Morrow County; SS = Saint-Séverin; Ebt = Elbert.

$GOS_{d>50}$°. A perfect 1:1 fit would have a y-intercept of 0 and a slope of 1, but the lowest *WSS* value possible is 1 whereas the lowest $GOS_{d>50}$ value possible is 0° (realistically ~0.1° considering detection limit, Sec. 2.4), and this causes the y-intercept to be greater than zero and the slope to be less than 1. Given that one of the main criteria in the *WSS* scheme is misorientation within grains as evident from variations in extinction position (Jamsja and Ruzicka, 2010), which is like what is measured by *GOS*, this indicates fundamental agreement between EBSD and optical microscopy for deformation. This is despite "extinction variation" being open to some interpretation (it depends for example on whether an overall extinction variation is considered, or whether the maximum extinction variation is considered; for this work an overall variation was considered). Although EBSD and optical microscopy are consistent, we can take mean *GOS* to be a quantitative metric for the intensity of olivine shock deformation, up to the point at which olivine begins to recrystallize. This metric for deformation intensity is free of any subjectivity that might arise in optical determinations of extinction variation.

In all Type 3 lithologies there is a tendency for *GOS* values in olivine to decrease with smaller grain sizes, regardless of lithology or overall deformation intensity (Table 2). The same is generally true for various minerals. This pattern was noted also for olivine in Type 6 chondrites (Ruzicka and Hugo, 2018). The grain size dependence of *GOS* means that it is important to specify grain size when specifying *GOS*.

3.3. Misorientation rotation axis directions in olivine (EBSD R parameter)

Averaged $R_{0.5\text{-}2}$ and $R_{2\text{-}10}$ values (Eq. [3], Sec. 2.4) that are statistically related to intragranular misorientation rotation axis directions and to what we suggest are activated slip systems in olivine for each lithology are given in Table 2. In general, the averaged $R_{2\text{-}10}$ and $R_{0.5\text{-}2}$ values for the lithologies correlate (r^2 = 0.90, although the regression is controlled by the difference between NWA 11351 and other lithologies), and $R_{0.5\text{-}2}$ values will not be considered further.

Fig. 5 shows olivine Crystal Rotation Axis (*CRA*) plots for 2-10° rotation misorientations in a *LAM* dataset for each Type 3 chondrite lithology arranged according to increasing $R_{2\text{-}10}$. For reference Fig. 5a shows the inferred slip systems that correspond to these rotations and Fig. 5l gives directions in the olivine crystal frame. For NWA 11351 Lithology A and B, the *CRA* plots are dominated by rotation axes in the <100> direction (Fig. 5b-c). For other lithologies, rotation axis directions are more varied, concentrating along the principal axis directions, <100>, <010>, or <001>, but with a significant number in other directions along the periphery of the *CRA* plots (Fig. 5d-k). In all cases there are relatively few rotation axes in the <012> direction, or in directions away from the edges of the *CRA* plots such as <111> or <212> (center of CRA plot) (Fig. 5).

The data in *CRA* plots can be quantified with f-values (Sec. 2.4). In Fig. 6, f-values for 2-10° rotations are shown in ternary diagrams for the Type 3 chondrites of this study compared to data previously obtained for Type 6 chondrites (Ruzicka and Hugo, 2018; Hugo et al., 2020) and to coarse grain interiors in ureilite NWA 11993 (Frye, 2022). These ternaries quantitatively portray misorientation rotation axis data for olivine, with variations in the $R_{2\text{-}10}$ parameter given along the left join ($f_{<100>}$ vs. ($f_{<010>}$ + $f_{<001>}$)) and data for other directions used as additional variables.

Fig. 6 reveals some trends, which can be conveniently discussed with respect to $R_{2\text{-}10}$. Fig. 6a ($f_{<100>}$ vs. [$f_{<010>}$ + $f_{<001>}$] vs. $f_{<210>}$) shows an overall linear trend, with the proportion of <210> rotation axes remaining almost constant for different chondrites despite large variations in $R_{2\text{-}10}$. There is at best a slight increase in the number of <210> rotation axes as $R_{2\text{-}10}$ increases, except at the highest $R_{2\text{-}10}$ values, represented by ureilite NWA 11993, which shows a large decrease in $f_{<210>}$ together with a further drop in $f_{<100>}$. Fig. 6b ($f_{<100>}$ vs. [$f_{<010>}$ + $f_{<001>}$] vs. [$f_{<101>}$ + $f_{<210>}$ + $f_{<012>}$]) shows an overall curved trend, away from $f_{<100>}$ at lower $R_{2\text{-}10}$ values, and towards the $f_{<001>}$ + $f_{<010>}$ apex at higher $R_{2\text{-}10}$ values. The highest values for the sum of $f_{<210>}$+$f_{<012>}$+$f_{<101>}$ occur at intermediate $R_{2\text{-}10}$ values and include most of the Type 3 chondrites of this study.

Considering the data shown in ternary (Fig. 6) and *CRA* plots (Fig. 5), the following systematics in olivine slip directions are implied. At the lowest $R_{2\text{-}10}$ values, most rotation axes are in the <100> direction and secondarily in the <210> direction, implying mostly **c**-type slip. Meteorites with this characteristic include Lithologies A and B of NWA 11351 of this study (Fig. 5), as well as the Type 6 chondrites Bruderheim, Leedey, and Morrow County (Ruzicka and Hugo, 2018) and somewhat more distantly, Elbert (Hugo et al., 2020) (Fig. 6). At higher $R_{2\text{-}10}$ values, which includes all of the remaining Type 3 chondrites of this study, as well as the Type 6 chondrites Portales Valley, MIL 99301, Kernouvé, and the MIL 99301 melt clast (Ruzicka and Hugo, 2018), there is a multiplicity of rotation axis directions, with relatively fewer <100> and more <010>, <100>, <101> and <210> rotation axes (Fig. 5, 6). This corresponds to a combination of **c**-type and **a**-type slip directions. At higher $R_{2\text{-}10}$ values, which includes the Type 6 chondrites Park (Ruzicka and Hugo, 2018) and Saint-Séverin (Hugo et al., 2020), and ureilite NWA 11993 (Frye 2022), <010> rotation axes become dominant, and <001> rotation axes also become notable in the ureilite (Fig. 6; Frye, 2022). This corresponds to a combination of **c**-type and **a**-type slip with the latter becoming more important in the ureilite. Altogether, there is a progressive increase in (**a**-slip)/(**c**-slip) ratio, from Bruderheim (L6) on the low end ($R_{2\text{-}10}$ = 0.348) to NWA 11993 (ureilite) on the high end ($R_{2\text{-}10}$ = 0.879), with most Type 3 chondrites (except NWA 11351 Lithology A and B) about half-way between these end members ($R_{2\text{-}10}$ = 0.604-0.649).

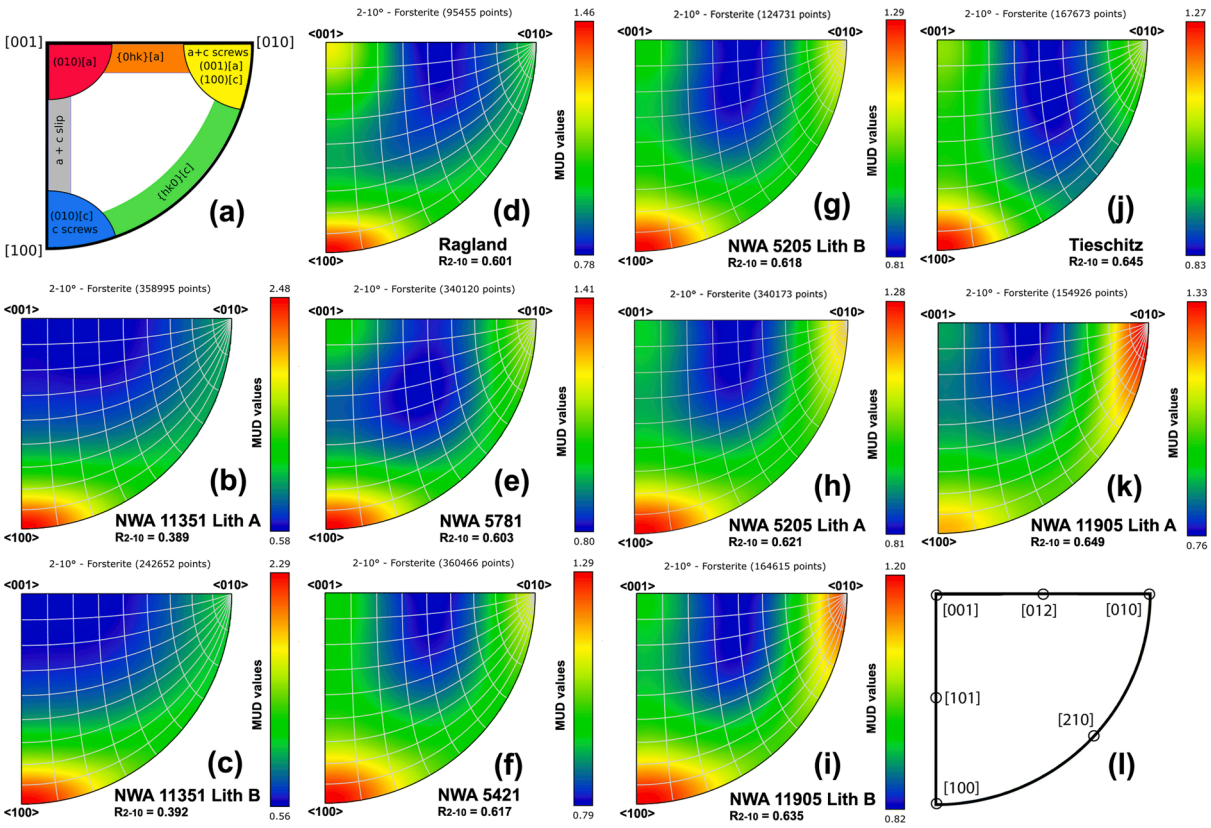

Fig. 5. Crystal Rotation Axis (CRA) plots for 2-10° misorientations in olivine (olivine crystal frame, equal-area projection, 25° half-width contouring, 10° great circle grid overlay) in Large Area Maps (LAMs) from each lithology. Colors show values of Multiples of Uniform Distribution (MUD), a spatial density value. Plots b-k are arranged in order of increasing $R_{2\text{-}10}$ values (R is proportional to the number of <001> and <010> compared to <100> rotation axis directions). (a) Schematic CRA diagram for olivine indicating slip systems corresponding to rotation axis directions; colors here correspond to increasing inferred deformation temperature (in sequence blue, green, yellow, orange, red; grey is indeterminate) (Ruzicka and Hugo, 2018). (b) NWA 11351 LAM Lithology A: $R_{2\text{-}10}$ = 0.389, MUD range = 0.58 (blue)-2.48 (red). (c) NWA 11351 LAM Lithology B: $R_{2\text{-}10}$ = 0.392, MUD range = 0.56 (blue)-2.29 (red). (d) Ragland LAM: $R_{2\text{-}10}$ = 0.601, MUD range = 0.78 (blue)-1.46 (red). (e) NWA 5781 LAM: $R_{2\text{-}10}$ = 0.603, MUD range = 0.80 (blue)-1.41 (red). (f) NWA 5421 LAM: $R_{2\text{-}10}$ = 0.617, MUD range = 0.79 (blue)-1.29 (red). (g) NWA 5205 LAM Lithology B: $R_{2\text{-}10}$ = 0.618, MUD range = 0.81 (blue)-1.29 (red). (h) NWA 5205 LAM Lithology A: $R_{2\text{-}10}$ = 0.621, MUD range = 0.81 (blue)-1.28 (red). (i) NWA 11905 LAM1 Lithology B: $R_{2\text{-}10}$ = 0.635, MUD range – 0.82 (blue)-1.20 (red). (j) Tieschitz LAM1: $R_{2\text{-}10}$ = 0.648, MUD range = 0.83 (blue)-1.27 (red). (k) NWA 11905 LAM1 Lithology A: $R_{2\text{-}10}$ = 0.649, MUD range = 0.76 (blue)–1.33 (red). (l) Approximate directions in an olivine crystal frame shown in a CRA-type format (inverse pole figure).

3.4. Skewness of Grain Orientation Spread (EBSD Sk parameter) in olivine

The skew or asymmetry of *GOS* distributions for an olivine grain population is related to heterogeneity and can provide clues either for annealing or the admixture of deformed material (Ruzicka and Hugo, 2018). Here we provide data on the relationship of *Sk* value (Eq. [2], Sec. 2.4) to grain size that can help distinguish between these possibilities.

Figure 7 shows the relationship between olivine *GOS* skewness and average equivalent grain size for three grain size bins (d = 5-15, d = 15-50, d > 50 μm) based on large maps (*LAM* and *miniLAM* datasets) for Type 3 chondrites (Fig. 7a), compared to the data for Type 6 chondrites based on *LAM* datasets (Fig. 7b) (Ruzicka and Hugo, 2018; Hugo et al., 2020). Because skewness refers to the *GOS* distribution for a grain population, grains are binned into different equivalent diameter ranges to increase grain statistics. These bin ranges are arbitrary, but they are chosen with the recognition that there are typically many more small grains than large, so that bin ranges can be smaller for smaller grains and still allow each of these bins to be populated with many grains. For most *LAMs*, which were mapped at a step size of 4 μm, the smallest grain that can be resolved using the grain criteria used is d ~10 μm, although *miniLAM* data allow smaller grain sizes to be measured.

In all Type 3 chondrite datasets for grain sizes with equivalent diameters $d \geq$ 5-10 μm, there is an overall positive skewness (*Sk*>1) (Fig. 7). This indicates tails to high *GOS* values in the *GOS* distributions. However, the extent of positive skew varies greatly, as does the trend of *Sk* with respect to grain size. For most Type 3 chondrites, except Ragland and Tieschitz, *Sk* values are low (*Sk* ~1.1-1.4; ~1.4-1.5 for NWA 11905 Lithology A) and do not vary much according to grain size, although there is small uptick in *Sk* at smaller grain sizes (Fig. 7a). Ragland and Tieschitz have higher skew which increases sharply at the lowest grain size (Fig. 7a).

For Type 6 chondrites there are three basic patterns. Most Type 6 chondrites have overall low values of skew (*Sk* ~1.1-1.25) that do not change much with grain size, except for the MIL 99301 melt clast which shows large increases in *GOS* skew at lower grain size, and except for Park, which has a high skew at coarse grain sizes that increases further at smaller grain sizes (Fig. 7b). A different pattern is shown by three chondrites, MIL 99301 host, Portales Valley, and Kernouvé, which have high values of *Sk* at the largest grain size and decreasing skew for smaller grain size (Fig. 7b).

Thus, most Type 3 chondrites resemble most Type 6 chondrites in having low *Sk* values that do not vary too much with grain size, but there are chondrites that show other patterns. This result has implications for annealing on the d ≥ 5-10 μm scale and will be discussed in Sec. 4.2.1.

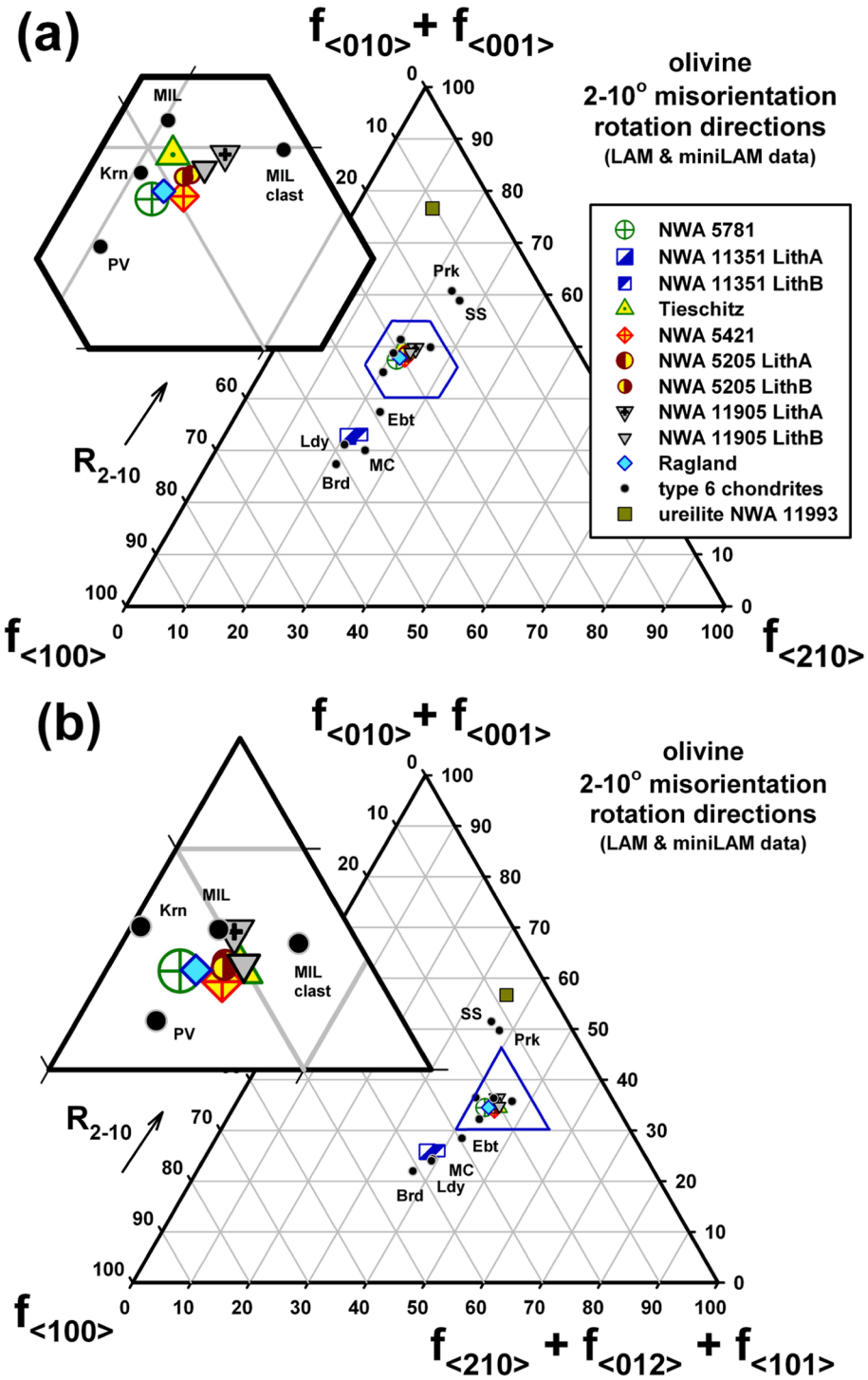

Fig. 6. Olivine misorientation rotation axis data for the Type 3 chondrites of this study (averaged LAM and miniLAM data) compared to Type 6 chondrites (LAM data; Ruzicka and Hugo, 2018; Hugo et al., 2020; meteorite abbreviations same as in Fig. 4) and ureilite NWA 11993 (LAM data; Frye, 2022). 'f' represents the fraction of misorientation rotations in the indicated crystal directions based on MUD values. Lith = lithology. The join at left in both plots corresponds to variations in the $R_{2\text{-}10}$ parameter. Insets better show the data for most Type 3 chondrites. (a) $f_{<100>}$ vs. $f_{<210>}$ vs. $(f_{<010>} + f_{<001>})$. Altogether, most data form a rough linear trend corresponding to variations in $R_{2\text{-}10}$ parameter; most Type 3 chondrites cluster tightly near MIL 99301 (MIL) and Kernouvé (Krn). (b) $f_{<100>}$ vs. $(f_{<210>} + f_{<012>} + f_{<101>})$ vs. $(f_{<010>} + f_{<001>})$. Altogether, data appear to form a curved trend, away from $f_{<100>}$ at lower $R_{2\text{-}10}$ values and bending towards $(f_{<010>} + f_{<001>})$ at higher $R_{2\text{-}10}$ values. Most Type 3 chondrites form a tight cluster in f-values close to MIL 99301, Kernouvé, and Portales Valley.

3.5. *Microtomography fabric data*

Table 3 and Fig. 8 provide microtomography data for metal and sulfide grains in NWA 5781 and three lithologies of NWA 11351. Collectively, these data can be used to evaluate the existence and nature of petrofabrics (Shape Preferred Orientations, or *SPOs*) based on grain shapes. Tomography specimens included one sample of NWA 5781 that is strongly clustered and moderately shocked (S3), and one sample of NWA 11351 that has three lithologies including two Type 3 lithologies (A, B) that vary in cluster texture strength and that are strongly shocked

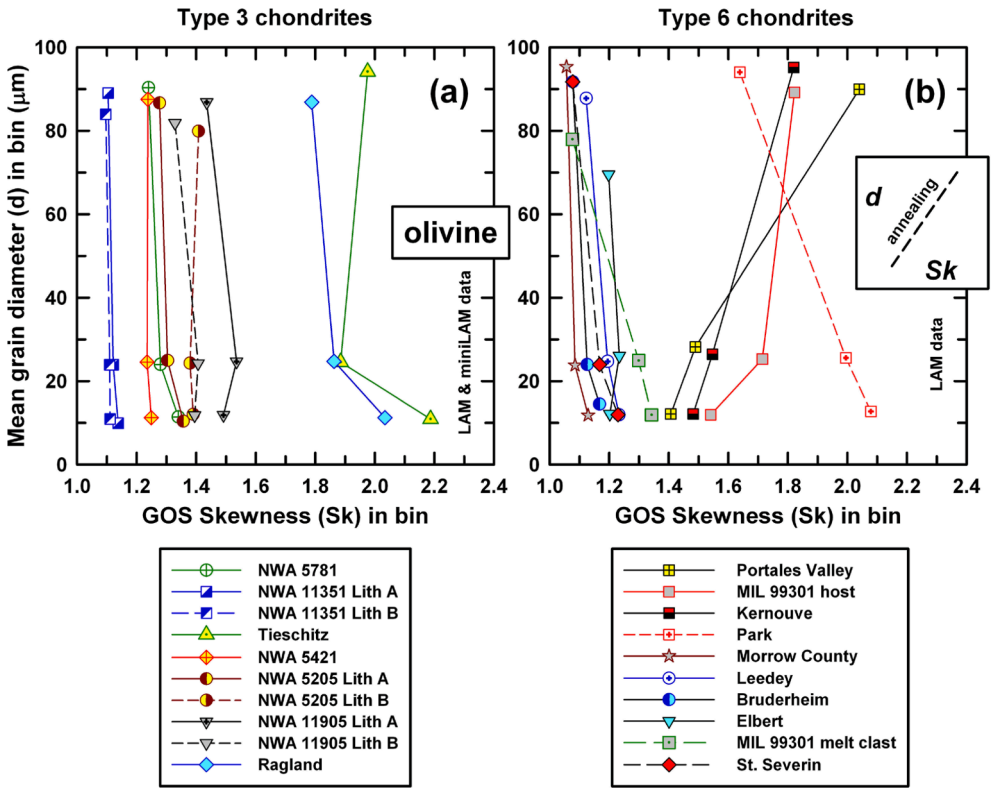

Fig. 7. Relationship between grain size (mean equivalent diameter d) and GOS skewness (Sk) in three grain size bins (d>50 μm, d=15-50 μm, and d=5-15 μm). (a) Type 3 chondrites of this study, based on averaged LAM and miniLAM datasets. (b) Type 6 chondrites, based on LAM datasets (Ruzicka and Hugo, 2018; Hugo et al., 2020). The inset shows a schematic trend expected for preferential removal of dislocations (decreasing GOS and GOS skewness) for smaller grains, as would expected for recovery during annealing.

Table 3
Fabric parameters (C, T, K) for opaque grains (metal and sulfide) in NWA 5781 and three lithologies of NWA 11351 obtained via microtomography. N_g = number of grains included in metric.

	Resolution (μm/voxel)	C -parameter [1]	Ng for C	T-parameter [2]	K-parameter [3]	Ng for T & K
NWA 5781	15.5	1.01	17948	0.53	0.33	Largest 5000
NWA 11351 Lithology A	16.5	0.874	11640	0.35	0.47	Largest 5000
NWA 11351 Lithology B	16.5	0.955	10077	0.66	0.21	Largest 5000
NWA 11351 Lithology C	16.5	0.862	747	0.37	0.41	747

[1] C-parameter of Woodcock & Naylor (1983): higher values indicate more shape-preferred-orientation (SPO). [2] T-parameter of Jelinek (1981): ranges from T= -1 for pure lineation to T= +1 for pure foliation; $0 \leq T \leq 1$ indicates planar fabric. [3] K-parameter of Woodcock and Naylor (1983): ranges from K=0 for uniaxial girdle to K = infinity for uniaxial clusters; $K < 1$ indicates girdle-shaped spatial distribution.

(S4). The third lithology of NWA 11351 (C) is a breccia with metamorphosed material (Type 5, 6) (Sec. 3.1.1). These three lithologies in NWA 11351, and the occurrence of strongly clustered Lithology A as crude layer between the other two, is shown in the hand specimen image in Fig. 8, which also shows the direction that data were acquired during microtomography (from bottom to top) and how the stereoplots are related to the sample orientation (the center of the stereoplots point upwards in the direction of the arrow).

In all the stereoplots for the four lithologies, the long axes of metal and troilite grains (modeled as best-fit ellipsoids) are mainly oriented within a common orientation plane (a foliation), and the short axes are oriented normal to this plane (a lineation) (Fig. 8). Within the common orientation plane, the long axes of grains are not equally clustered; there is a preferred direction (lineation).

In NWA 11351, the three lithologies have nearly the same petrofabric. For instance, the main short axis direction of the metal and troilite grains are only a few degrees apart for Lithology A, B, and C (Fig. 8). Also, this short axis direction is approximately normal to the lithology contacts in hand specimen, and the long axis directions are subparallel to these contacts (Fig. 8).

In Table 3, metrics quantify the *SPO* characteristics. All four lithologies have relatively high values of the strength parameter, *C*, indicating a strong or anisotropic *SPO*. Although there are some variations in the values for *C*, the values are among the highest that have been analyzed in chondrites (Friedrich et al., 2017). The nature of the *SPO* as a foliation of the long axes of metal and troilite grains is confirmed by the *T-parameter* and *K-parameter*, both of which can be described as indicative of foliation (Table 3). Furthermore, the *T-* and *K-parameters* vary in a coordinated fashion, with *T-parameter* being higher and *K-parameter* being lower for NWA 5781 and 11351 Lithology B; and *T-parameter* being lower and *K-parameter* being higher for NWA 11351 Lithology A and C (Table 3). This suggests a somewhat stronger foliation tendency in NWA 5781 and NWA 11351 Lithology B compared to Lithology A and C in NWA 11351. The strength factor *C* is also higher in the first two lithologies (Table 3), which implies that the value of *C* is mainly reflecting the strength of foliation.

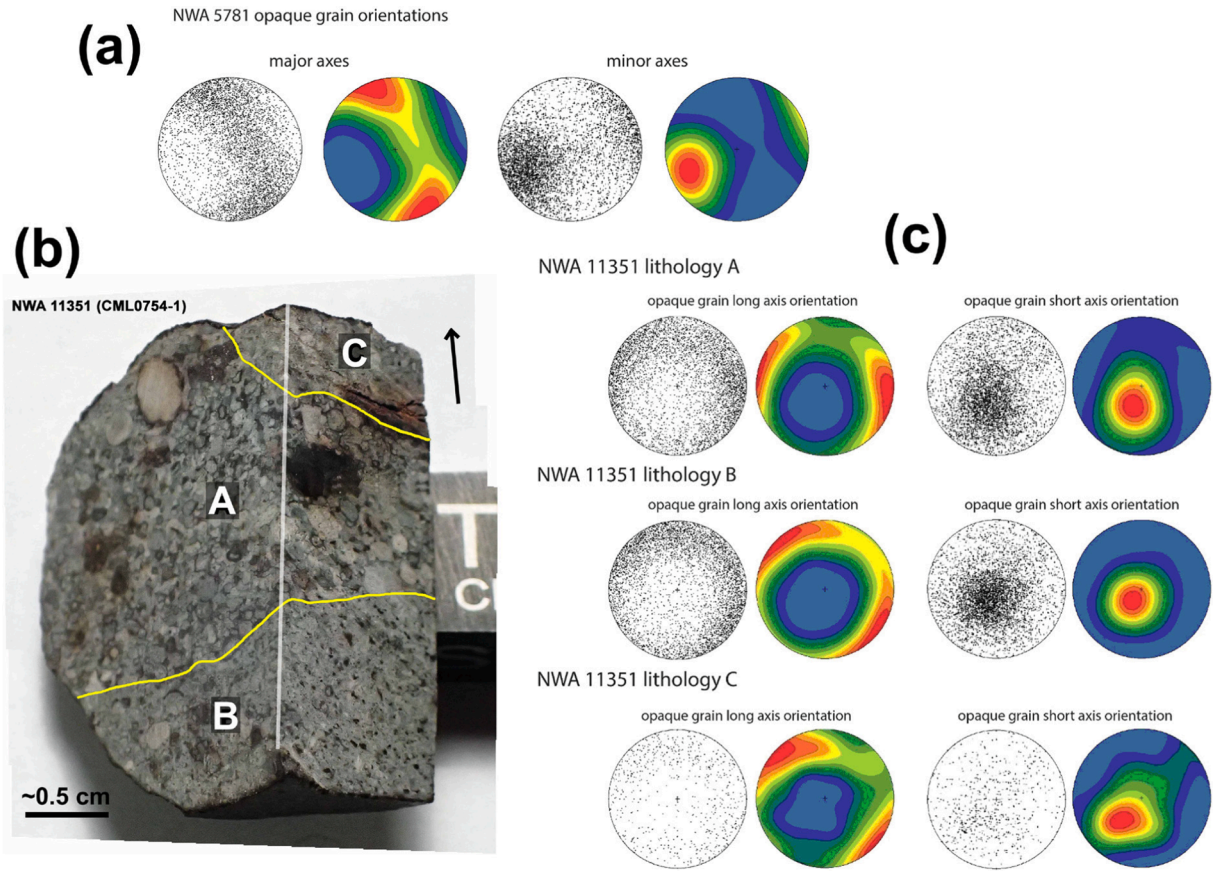

Fig. 8. Microtomography data for metal and sulfide grain shapes in NWA 5781 and NWA 11351. For each lithology, two sets of stereoplots are shown for major and minor axes, including individual grain data, and contoured versions with red = higher densities and blue = lower densities. **(a)** Stereoplots showing spatial orientations of grain shapes in NWA 5781. **(b)** Sample CML0754-1 used for tomography studies; Lithology A forms a lenticular body between Lithology B and C (contacts shown by yellow lines). The white line represents a corner between two nearly perpendicular cut faces (the right face is parallel to polished thin section 0754-2 used for SEM studies), the arrow shows the approximate direction towards the center point of the stereoplots in part c. **(c)** Stereoplots showing spatial orientations of grain shapes for all lithologies of NWA 11351.

3.6. Deformation of matrix and adjacent chondrules at small scales

Deformation of interchondrule areas (matrix) and adjacent chondrules were studied at small scales with EBSD using small step sizes for maps. Table 4 provides high-spatial-resolution EBSD data for olivine in matrix and adjacent chondrule regions (chondrule composites) in six different lithologies, including NWA 5781, Tieschitz, NWA 5421, NWA 5205 Lithology A, NWA 5205 Lithology B, and Ragland. These data are based on multiple targeted maps in each lithology and include averaged values for $R_{2\text{-}10}$, *GOS*, and *Sk* for different grain sizes in each lithology, including a $d < 5$ μm bin, together with *Sk* ratios ($Sk_{d15\text{-}50}/Sk_{d5\text{-}15}$ and $Sk_{d<5}/Sk_{d5\text{-}15}$). For most maps, step sizes were <1 μm, and for the $d < 5$ μm size bin, the average grain size is $d \sim 2$ μm.

In Table 4, there is no large overall difference evident *between matrix and adjacent chondrule regions* in terms of $R_{2\text{-}10}$, *GOS* and *Sk*. For instance, averaging all six lithologies, one finds values of $R_{2\text{-}10} = 0.633 \pm 0.054$ (±1 SD) for matrix and $R_{2\text{-}10} = 0.655 \pm 0.020$ for adjacent chondrules, which overlap to within the standard deviations. For a given grain size range, *GOS* values appear to be slightly higher for chondrules compared to adjacent matrix, but again the data overlap within standard deviations (Table 4). A similarity between chondrules and matrix is also seen for individual lithologies (Table 4). Therefore, the results indicate few overall differences between chondrules and adjacent matrix areas.

However, if one considers the smallest grain sizes, there are some notable variations in *GOS* parameters *between lithologies*. For instance, Fig. 9 plots *Sk* ratios for grains of different sizes ($Sk_{d15\text{-}50}/Sk_{d5\text{-}15}$ and $Sk_{d<5}/Sk_{d5\text{-}15}$) and *GOS* values for the smallest grains ($GOS_{d<5}$). There is a large variation in $Sk_{d<5}/Sk_{d5\text{-}15}$ ratios, with some values <1 and some values >1, in contrast to values of $Sk_{d15\text{-}50}/Sk_{d5\text{-}15}$ that are all similar and ≤1 (Fig. 9a). More significantly, the variable $Sk_{d<5}/Sk_{d5\text{-}15}$ ratios correlate positively with variable $GOS_{d<5}$ values, with the data for all lithologies except Ragland lying on one trend (Fig. 9b). This correlation indicates that for the smallest grains (d<5 μm), as overall deformation intensity ($GOS_{d<5}$) decreases, the asymmetry of *GOS* distributions for the smallest grains relative to larger grains ($Sk_{d<5}/Sk_{d5\text{-}15}$) decreases. Thus, grains become more homogenous in deformation intensity as grain size and overall deformation decrease. This result has implications for annealing on a small (d < 5 μm) scale and will be discussed in Sec. 4.2.2.

3.7. Composition of interchondrule and chondrule mesostasis areas

Chemical data were obtained for some key interchondrule and chondrule mesostasis constituents to help define relationships. The most extensive chemical dataset was obtained for Tieschitz. This meteorite was selected for detailed chemical study because it is a good example of a minimally weathered, strongly clustered chondrite. For Tieschitz, data are provided for interior chondrule mesostases, porous outer chondrule mesostases, fine-grained rims, interchondrule glass, and interchondrule olivine-rich pockets, as well as for "medium-grained rim / mesostasis" material that appears either as a coarser variety of rim, or that occurs in outer chondrule mesostases and that grades into fine-grained rims. For these constituents, individual "bulk" compositions (~5-20 μm scale) are shown for some key elemental ratios in Fig. 10, and corresponding full

Table 4
High spatial resolution EBSD olivine data for matrix and adjacent chondrule regions (chondrule composites) in different lithologies, including misorientation rotation parameter $R_{2\text{-}10}$, Grain Orientation Spread (*GOS*), and GOS skewness (*Sk*) for different equivalent grain diameters *d* (in μm). Values are means and ±1 standard deviation averaging different map areas (number of maps averaged given in parentheses). For the specified grain sizes, *Sk* and *GOS* data are based on maps with ≥40 and ≥5 olivine grains, respectively.

	Comment[1]	$R_{2\text{-}10}$	T^{2}_{deform} (°C)	GOS $_{d15\text{-}50}$ (°)	Sk $_{d15\text{-}50}$	GOS $_{d5\text{-}15}$ (°)	$Sk_{d5\text{-}15}$	GOS $_{d<5}$ (°)	$Sk_{d<5}$	$Sk_{d15\text{-}50}$ / $Sk_{d5\text{-}15}$	$Sk_{d<5}$ / $Sk_{d5\text{-}15}$	Annealing? [3]
NWA 5781												
Matrix	Chrl frags, coarser mtrx	0.743 ±0.060 (4)	1076 ±65 (4)	2.59 (1)	–	2.55 ±0.84 (4)	1.17 ±0.07 (2)	1.04 ±0.20 (4)	1.39 ±0.05 (4)	0.904 (1)	1.19 ±0.10 (2)	No
Chondrules		0.661 ±0.043 (3)	986 ±46 (3)	3.30 ±1.33 (2)	1.17 (1)	2.69 ±1.24 (3)	1.23 (1)	1.13 ±0.17 (3)	1.32 ±0.13 (3)	0.948 (1)	1.11 (1)	No
Tieschitz												
Matrix	Rims, smaller chrl frags, grains in metal-troi objects	0.628 ±0.056 (4)	950 ±61 (4)	1.72 ±0.74 (3)	1.30 ±0.09 (2)	1.48 ±0.45 (4)	1.72 ±0.08 (4)	0.67 ±0.21 (4)	1.39 ±0.20 (4)	0.86 ±0.20 (3)	0.81 ±0.14 (4)	Yes, d<5 only for 3 of 4 areas
Chondrules		0.647 ±0.035 (4)	970 ±39 (4)	1.30 ±0.54 (4)	1.94 ±0.24 (3)	1.04 ±0.24 (4)	1.94 ±0.32 (4)	0.70 ±0.19 (4)	1.52 ±0.22 (4)	0.965 ±0.006 (2)	0.789 ±0.093 (4)	Yes, d<5 only for 4 of 4 areas
NWA 5421												
Matrix	Fine grains, mineral clasts, rims, interchrl gls	0.645 ±0.051 (7)	969 ±56 (7)	2.76 ±0.88 (4)	–	2.32 ±0.49 (5)	1.43 ±0.19 (4)	1.06 ±0.24 (7)	1.38 ±0.11 (7)	–	1.01 ±0.13 (4)	No, except for d<5 in 1 of 4 areas (TM10)
Chondrules		0.678 ±0.071 (7)	1004 ±78 (7)	3.20 ±0.89 (7)	1.10 (1)	3.16 ±0.68 (7)	1.28 ±0.08 (4)	1.53 ±0.32 (6)	1.60 ±0.13 (6)	0.904 (1)	1.31 ±0.12 (3)	No
NWA 5205 Lithology A												
Matrix	Fine grains, clasts, interchrl gls	0.595 ±0.090 (3)	914 ±98 (3)	2.24 ±0.29 (2)	1.17 (1)	2.52 ±1.03 (3)	1.30 ±0.01 (2)	0.99 ±0.17 (3)	1.46 ±0.12 (3)	0.900 (1)	1.16 ±0.09 (2)	No
Chondrules		0.643 ±0.009 (2)	966 ±10 (2)	2.01 ±0.33 (2)	1.14 (1)	1.86 ±0.22 (2)	1.26 ±0.01 (2)	1.15 ±0.17 (2)	1.42 ±0.20 (2)	0.907 (1)	1.12 ±0.16 (2)	No
NWA 5205 Lithology B												
Matrix	Mainly mineral clasts	0.709 ±0.021 (2)	1039 ±23 (2)	1.55 ±0.37 (2)	1.28 ±0.09 (2)	1.22 ±0.28 (2)	1.35 ±0.04 (2)	0.69 ±0.07 (2)	1.37 ±0.01 (2)	0.953 ±0.036 (2)	1.02 ±0.04 (2)	No, except possibly for d<5 in 1 of 2 areas (TM9)
Chondrules	Chrl frags	0.677 ±0.036 (2)	1003 ±40 (2)	1.77 ±0.33 (2)	1.32 ±0.08 (2)	1.27 ±0.32 (2)	1.46 ±0.10 (2)	0.75 ±0.10 (2)	1.42 ±0.01 (2)	0.908 ±0.007 (2)	0.975 ±0.071 (2)	No, except for d<5 in 1 of 2 areas (TM9)
Ragland												
Matrix	Mainly mineral clasts	0.660 ±0.016 (4)	986 ±17 (4)	2.09 ±0.70 (4)	1.80 ±0.27 (3)	1.59 ±0.24 (4)	1.90 ±0.19 (4)	1.37 ±0.37 (3)	1.91 ±0.21 (3)	0.899 ±0.096 (3)	1.04 ±0.09 (3)	No, except for d<5 in 1 of 3 areas (TM6)
Chondrules	Chrl frags	0.629 ±0.023 (4)	951 ±25 (4)	2.17 ±1.85 (4)	2.27 ±0.69 (2)	1.67 ±0.93 (4)	2.21 ±0.41 (4)	1.31 ±0.43 (3)	2.00 ±0.19 (3)	0.994 ±0.024 (2)	0.871 ±0.166 (3)	Yes, d<5 only for 2 of 3 areas (TM2, TM6)
Average type 3 chondrite lithology												
Matrix	Many clasts, also rims & small grains	0.663 ±0.054 (6)	989 ±59 (6)	2.16 ±0.47 (6)	1.38 ±0.28 (4)	1.95 ±0.58 (6)	1.47 ±0.28 (6)	0.97 ±0.26 (6)	1.48 ±0.21 (6)	0.903 ±0.034 (5)	1.04 ±0.13 (6)	
Chondrules		0.655 ±0.020 (6)	980 ±21 (6)	2.29 ±0.80 (6)	1.49 ±0.50 (6)	1.95 ±0.82 (6)	1.56 ±0.41 (6)	1.09 ±0.32 (6)	1.54 ±0.25 (6)	0.938 ±0.037 (6)	1.03 ±0.19 (6)	

[1] frags = fragments, mtrx = matrix, chrl = chondrule, interchrl = interchrondrule, gls = glass, troi= troilite. [2] Model deformation temperature (see Text). [3] Tests for significant post-deformation annealing are based on ratios of Sk for different grain sizes: for microstructural annealing, predict $Sk_{d15\text{-}50}$ / $Sk_{d5\text{-}15}$ > 1 and $Sk_{d<5}$ / $Sk_{d5\text{-}15}$ <1 (see Text).

analyses of average compositions are given in Table 5. In Fig. 10, Al/(Si+Al) is a proxy for normative plagioclase (Al/(Si+Al) =0.25-0.5 at. for albite-anorthite, respectively); Na/(Na+Ca) is a proxy for normative albite / Ca-pyroxene ratio (given that Ca-plagioclase is not abundant); and Fe/(Fe+Mg) mainly represents the composition of ferromagnesian silicate.

3.7.1. *Tieschitz constituents*

All the analyzed constituents in Tieschitz have somewhat variable composition, as one would expect for mixtures of materials, but they still show chemical groupings (Fig. 10), with relatively low standard deviations for many chemical components (Table 5).

Interchondrule glass is feldspathic and sodic, with average Na/Si=0.39±0.03 at. (±1 SD), higher than for pure albite (Na/Si =0.33), and much lower than for pure nepheline (Na/Si=1), with an average of ~80 vol% normative plagioclase, ~7% nepheline, ~7% Ca-pyroxene, and ~5% olivine (Table 5). This glass is texturally equivalent to the "white matrix" described by Hutchison et al. (1998) and others. The composition generally resembles that of white matrix in Tieschitz given previously (Hutchison et al., 1998; Hutchison and Bevan, 1983; Alexander et al., 1989), especially the "poorly diffracting" material in white matrix (Alexander et al., 1989). We thus assume that our interchondrule glass in Tieschitz is equivalent to "white matrix" in this chondrite. The high normative feldspar and albitic composition place interchondrule glass at high values of Al/(Al+Si) and Na/(Na+Ca) (Fig. 10). This glass further has relatively elevated and variable Fe/(Fe+Mg) (0.46±0.10)

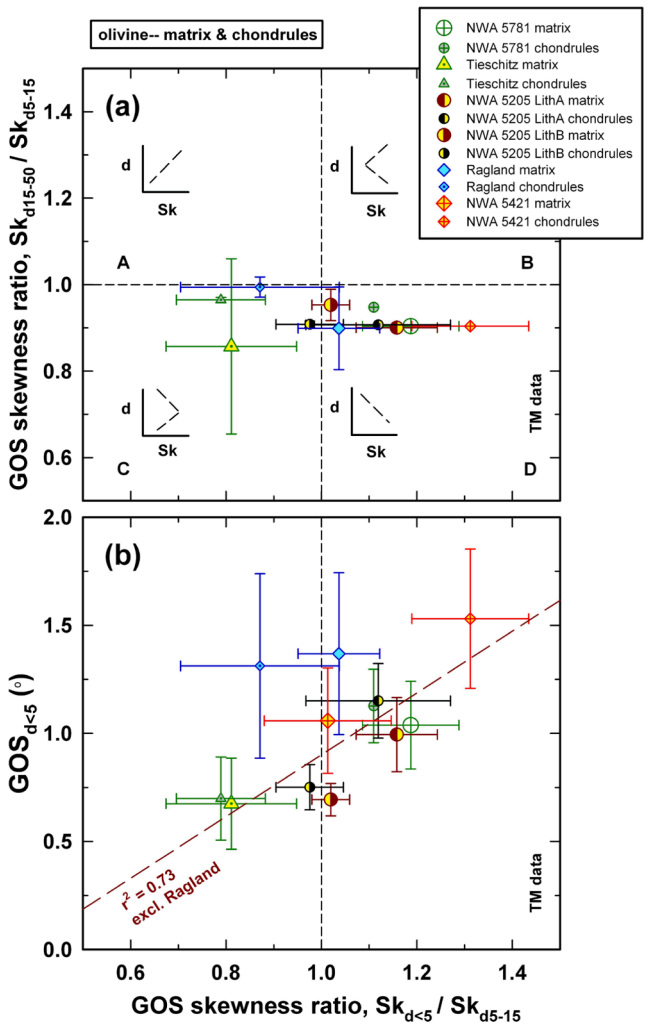

Fig. 9. *GOS* systematics for high-resolution datasets that include small (d < 5 μm) grains. Points are means of averaged data and bars indicate ±1 standard deviation of the means. **(a)** Variation of $Sk_{d<5}/Sk_{d5\text{-}15}$ with respect to $Sk_{d15\text{-}50}/Sk_{d5\text{-}15}$. A, B, C, D define four regions with different grain size (d) – skewness (Sk) trends (shown schematically, compare to Fig. 7). All data fall into regions C and D, characterized by $Sk_{d15\text{-}50}/Sk_{d5\text{-}15} \leq 1$ but with variable $Sk_{d<5}/Sk_{d5\text{-}15}$ (both <1 and >1). **(b)** Variation of $Sk_{d<5}/Sk_{d5\text{-}15}$ with respect to $GOS_{d<5}$. Excluding Ragland, data form a single trend (linear correlation coefficient r^2 = 0.73).

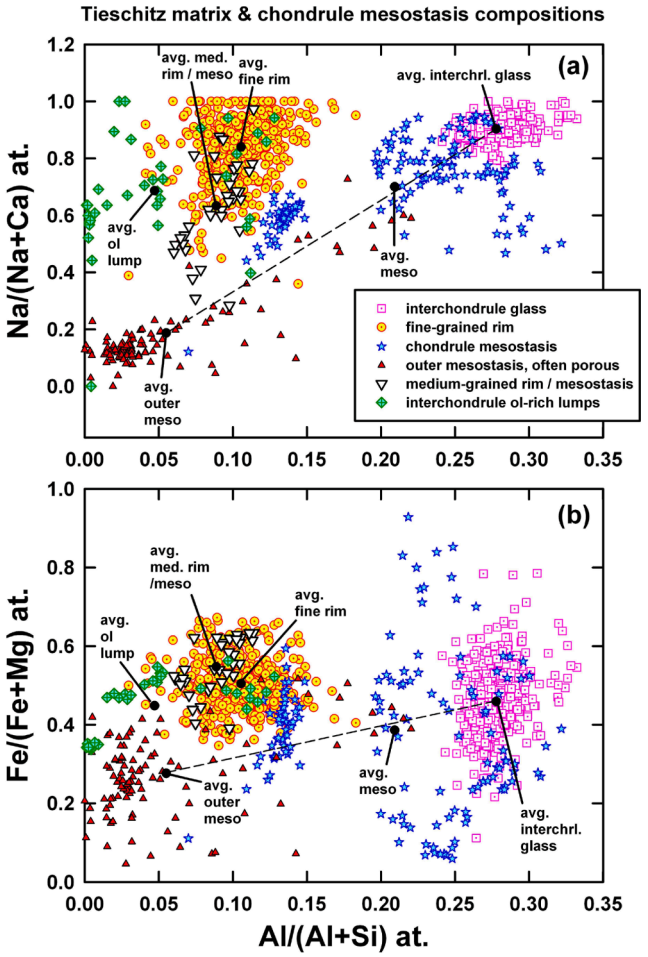

Fig. 10. Bulk analyses (on scale ~5-20 μm across) of constituents in Tieschitz, including chondrule mesostases, rims, and interchondrule areas analyzed by *EDS*. Average (avg.) compositions are indicated and are reported in Table 5. The dashed line is a mixing line between average interchondrule glass and average outer chondrule mesostasis; average chondrule mesostasis falls nearly on this line. **(a)** Al/(Al+Si) vs. Na/(Na+Ca). **(b)** Al/(Al+SI) vs. Fe/(Fe+Mg).

(Table 5, Fig. 10).

Fine-grained ferromagnesian rims are texturally equivalent to the "dark matrix" described by Hutchison et al. (1998). On average they are rich in normative olivine (average ~61%) and plagioclase (~16%), with the third most abundant constituent being normative nepheline (3.3 ±1.9 %) (Table 5). Analyzed compositions of the fine-grained rims scatter but have Na/(Na+Ca) and Fe/(Fe+Mg) ratios that overlap that of interchondrule glass, being only slightly less sodic and more ferroan on average (Fig. 10, Table 5). The relatively binary olivine + feldspathic normative composition of fine-grained rims agrees with TEM observations of rims in Tieschitz and other ordinary chondrites, which were found to consist chiefly of submicron olivine within a fine-grained amorphous feldspar "glue" (Alexander et al., 1989).

Olivine-rich pockets in Tieschitz interchondrule areas consist largely of fine-grained olivine crystallites (Sec. 3.1.4). Chemical data show that the pockets are nearly binary mixtures of normative olivine (~88 vol% on average) and plagioclase (~8% on average), but that they vary greatly from place to place in these two components (Table 5, Fig. 10). Some analyses of pockets range to Al/(Al+Si) ~0, indicating essentially no feldspar component and nearly pure olivine with Fa = Fe/(Fe+Mg) ~0.35. Other analyses of olivine-rich pockets with greater feldspar component are identical to fine-grained rims in terms of the key element ratios shown in Fig. 10. This suggests a chemical relationship between olivine-rich pockets and fine-grained rims.

Bleached outer mesostasis areas in microporphyritic chondrules are enriched in augite crystallites (Sec. 3.1.4). Chemically, these areas have low Al/(Al+Si) and low Na/(Na+Ca) values that reflect a high normative Ca-pyroxene composition (Fig. 10, Table 5), as one would expect from their petrography. Fe/(Fe+Mg) values vary but are mostly ~0.2-0.3. Besides Ca-pyroxene, normative low-Ca pyroxene and plagioclase are variably present and on average are the second and third most abundant components, respectively (Table 5). Overall silica content is also variable, including mostly quartz-normative but some slightly nepheline-normative compositions (Table 5). Some of these areas texturally resemble "blocky mesostasis" described by Hutchison et al. (1998), but the compositions are different, reflecting more feldspathic material in the analyses of Hutchison et al. (1998).

Analyses of mesostasis compositions within the interiors of microporphyritic chondrules, not adjacent to chondrule margins, have highly scattered compositions (Fig. 10). This is caused in part by varying amounts of Ca-pyroxene crystallites and feldspathic glass within analysis volumes. There are two chemical groups: (1) a group with Al/(Al+Si) ~0.12-0.15 that corresponds to areas with fine Ca-pyroxene

Table 5
Compositions of inter- and intra-chondrule constituents based on SEM analyses. N = number of analyses, n.d. = not determined, Low-Ca pyroxene = normative orthopyroxene (enstatite-ferrosilite), Ca-pyroxene = normative clinopyroxene (diopside-hedenbergite). Values for N>1 are means of individual analyses with ±1 standard deviations shown.

	(1) Tieschitz "white matrix"[1]	(2) Tieschitz inter-chondrule glass[2]	(3) Tieschitz matrix olivine pockets[2]	(4) Tieschitz fine-grained rim[2]	(5) Tieschitz medium-grained rim[2]	(6) Tieschitz porous outer chondrule mesostasis[2]	(7) Tieschitz chondrule mesostasis[2]	(8) NWA 5421 site 296 vuggy inter-chondrule glass[3]	(9) NWA 5421 site 296 vuggy chondrule glass[3]	(10) NWA 11351 site 1N "spotted matrix" feldspar glass[4]	(11) NWA 11351 site 1N "spotted matrix" olivine glass[4]
N	2	352	35	453	34	107	140	1	1	4	6
Wt%											
SiO_2	61.5 ±0.2	57.4 ±2.2	36.0 ±1.1	35.9 ±2.5	40.6 ±3.2	51.9 ±2.3	59.3 ±3.3	71.3	67.8	64.8 ±1.2	37.5 ±0.8
TiO_2	n.d.	0.28 ±0.30	0.11 ±0.16	0.17 ±0.22	0.12 ±0.14	0.51 ±0.42	0.51 ±0.27	0.07	0.23	n.d.	n.d.
Al_2O_3	19.3 ±0.13	18.7 ±1.2	1.59 ±1.50	3.60 ±0.80	3.35 ±0.62	2.97 ±3.54	13.6 ±4.5	20.0	23.3	19.3 ±1.0	0.22 ±0.24
Cr_2O_3	n.d.	0.22 ±0.29	0.62 ±0.30	0.32 ±0.29	0.28 ±0.24	1.42 ±0.80	0.32 ±0.30	n.d.	n.d.	n.d.	0.16 ±0.26
FeO	3.30 ±0.12	4.88 ±2.05	34.6 ±4.0	35.3 ±4.4	34.0 ±5.4	10.0 ±3.5	5.42 ±3.05	0.60	0.52	1.24 ±0.52	25.4 ±0.7
MnO	n.d.	0.19 ±0.27	0.45 ±0.25	0.47 ±0.34	0.48 ±0.26	0.70 ±0.54	0.28 ±0.24	n.d.	0.05	n.d.	n.d.
MgO	2.01 ±0.08	3.20 ±1.18	24.4 ±5.4	19.5 ±2.8	2.31 ±1.66	15.6 ±5.6	5.08 ±2.63	0.55	0.08	1.49 ±0.91	35.1 ±0.6
CaO	3.27 ±0.07	2.28 ±0.86	0.60 ±0.76	0.81 ±0.75	2.31 ±1.66	13.6 ±4.4	6.31 ±2.57	0.55	0.32	1.36 ±0.82	0.24 ±0.20
Na_2O	7.30 ±0.10	11.7 ±0.8	0.92 ±0.94	2.31 ±0.71	1.98 ±0.43	1.89 ±1.60	8.46 ±2.34	6.78	6.40	9.19 ±0.49	0.04 ±0.10
K_2O	0.11 ±0.04	0.39 ±0.28	0.08 ±0.10	0.22 ±0.17	0.27 ±0.12	0.16 ±0.16	0.13 ±0.13	0.86	0.39	0.52 ±0.21	0.03 ±0.08
P_2O_5	–	0.08 ±0.33	0.07 ±0.15	0.28 ±0.73	0.25 ±0.36	0.55 ±0.92	0.19 ±0.32	n.d.	n.d.	n.d.	n.d.
Cl	n.d.	0.11 ±0.12	0.20 ±0.20	0.39 ±0.27	0.25 ±0.15	0.20 ±0.15	0.06 ±0.08	n.d.	n.d.	n.d.	n.d.
S	n.d.	0.08 ±0.13	0.07 ±0.15	0.12 ±0.17	0.18 ±0.23	0.20 ±0.32	0.10 ±0.09	n.d.	n.d.	n.d.	n.d.
Ni	–	0.26 ±0.37	0.19 ±0.22	0.38 ±0.46	0.23 ±0.23	0.22 ±0.34	0.12 ±0.19	0.05	n.d.	0.43 ±0.86	0.87 ±0.70
Total	96.8	99.8	99.9	99.7	99.8	99.8	99.8	100.7	99.1	98.7	99.5
Atomic											
Na/Si	–	0.39 ±0.03	0.05 ±0.05	0.13 ±0.04	0.10 ±0.03	0.07 ±0.06	0.28 ±0.08	0.18	0.18	0.27 ±0.01	0.00 ±0.00
Na/(Na+Ca)	–	0.90 ±0.04	0.69 ±0.20	0.84 ±0.12	0.63 ±0.16	0.19 ±0.14	0.70 ±0.14	0.96	0.97	0.92 ±0.05	0.00 ±0.00
Fe/(Fe+Mg)	–	0.46 ±0.10	0.45 ±0.08	0.50 ±0.06	0.55 ±0.07	0.28 ±0.11	0.39 ±0.18	0.39	0.79	0.38 ±0.24	0.29 ±0.01
Al/(Al+Si)	–	0.28 ±0.01	0.05 ±0.04	0.11 ±0.02	0.09 ±0.02	0.06 ±0.06	0.21 ±0.06	0.25	0.29	0.26 ±0.01	0.01 ±0.01
Cation/8O	–	–	–	–	–	–	–	4.76	4.74	4.98 ±0.02	–
Cation/4O	–	–	–	–	–	–	–	–	–	–	3.00 ±0.01
Norm (vol%) [5]											
Olivine	–	5.3 ±3.3	87.7 ±9.4	75.9 ±5.7	61.3 ±12.2	4.5 ±8.2	2.1 ±2.7	–	–	–	–
Low-Ca pyroxene	–	<0.1	0.1 ±0.5	0.3 ±2.0	6.3 ±7.7	23.1 ±20.7	6.5 ±9.3	–	–	–	–
Ca-pyroxene	–	6.6 ±2.9	1.8 ±2.3	2.1 ±2.4	8.2 ±5.8	49.8 ±19.3	18.8 ±9.5	–	–	–	–
Plagioclase	–	80.3 ±4.1	7.8 ±6.7	16.3 ±4.5	21.9 ±4.0	16.2 ±15.6	65.2 ±16.2	–	–	–	–
Merrillite	–	0.1 ±0.3	<0.1	0.3 ±1.3	0.3 ±0.5	0.9 ±1.6	0.3 ±0.5	–	–	–	–
Cl-apatite	–	0.1 ±0.2	<0.1	0.3 ±0.4	0.3 ±0.5	0.5 ±0.7	0.1 ±0.2	–	–	–	–
Chromite	–	0.2 ±0.2	0.7 ±0.3	0.3 ±0.3	0.3 ±0.2	1.4 ±0.8	0.3 ±0.3	–	–	–	–
Ilmenite	–	0.3 ±0.3	0.2 ±0.2	0.2 ±0.3	0.2 ±0.2	0.7 ±0.5	0.6 ±0.3	–	–	–	–
Metal	–	0.4 ±0.5	0.4 ±0.5	0.8 ±1.1	0.5 ±0.5	0.4 ±0.6	0.2 ±0.3	–	–	–	–
Troilite	–	<0.1	<0.1	<0.1	0.1 ±0.1	0.1 ±0.1	0.1 ±0.1	–	–	–	–

(*continued on next page*)

Table 5 (*continued*)

	(1) Tieschitz "white matrix"[1]	(2) Tieschitz inter-chondrule glass[2]	(3) Tieschitz matrix olivine pockets[2]	(4) Tieschitz fine-grained rim[2]	(5) Tieschitz medium-grained rim[2]	(6) Tieschitz porous outer chondrule mesostasis[2]	(7) Tieschitz chondrule mesostasis[2]	(8) NWA 5421 site 296 vuggy inter-chondrule glass[3]	(9) NWA 5421 site 296 vuggy chondrule glass[3]	(10) NWA 11351 site 1N "spotted matrix" feldspar glass[4]	(11) NWA 11351 site 1N "spotted matrix" olivine glass[4]
Nepheline	–	6.7 ±1.8	1.1 ±1.5	3.3 ±1.9	0.6 ±1.1	0.4 ±1.3	2.5 ±3.5	–	–	–	–
Quartz	–	<0.1	<0.1	<0.1	<0.1	2.2 ±3.0	3.5 ±5.0	–	–	–	–

1 "White matrix" based on 6 x 5 μm EDS analysis spots (Hutchison et al., 1998). [2] Mean bulk compositions based on ~5-20 (up to ~50) μm-diameter analyses from EDS map data; analyses were individually normalized to 100% totals prior to averaging and calculation of a norm. "Interchondrule glass" and "fine-grained rim" are texturally equivalent to the "white matrix" and "dark matrix", respectively, of Hutchison et al (1992). [3] Focused beam analyses, with data normalized by using olivine and pyroxene as internal standards to yield an average total of 100% for the standards. [4] Focused beam analyses of material that with EBSD does not index as either plagioclase or olivine and which has low crystallinity. [5] Modified CIPW norm. Assumes mineral densities as given by Gaines et al. (1997) with linear interpolation between endmembers. Metal assumes $Fe_{80}Ni_{20}$ composition. In columns (6) and (7), the presence of both nepheline and quartz in the mean norm is attributed to different analyses being Si-undersaturated or Si-oversaturated, thus giving average values >0 for both normative nepheline and quartz.

crystallites within glass, and (2) a group with Al/(Al+Si) ~0.19-0.32 that corresponds to areas with larger crystals within glass that have highly varied crystal/glass proportions (Fig. 10). Interior mesostasis compositions are dominated by normative plagioclase with lesser normative Ca-pyroxene, and are mainly quartz normative but locally nepheline normative (Table 5). In terms of average Al/(Al+Si), Fe/(Fe+Mg), and Na/(Na+Ca) ratios, interior mesostasis lies close to a mixing line between interchondrule feldspathic glass and outer, porous ("bleached") mesostasis (Fig. 10). This suggests a chemical relationship between interior chondrule mesostases, bleached zones, and interchondrule glass. Finally, medium-grained rim / mesostasis areas were analyzed. They occur at the margins of chondrules in two forms: 1) like fine-grained rims but coarser, and 2) within the mesostases of chondrules where they appear to replace normal chondrule mesostases. In neither setting is this material especially porous on the scale of observation. In both cases, they chemically resemble fine-grained rims and may be a variant of them, with both Al/(Al+Si) and Fe/(Fe+Mg) values completely overlapping those for fine-grained rims (Fig. 10). However, compared to fine-grained rims, medium-grained rims have more normative pyroxene, more normative plagioclase, and less normative olivine on average (Table 5).

3.7.2. NWA 5421 vuggy glass

This chondrite shows many of the same textural features as Tieschitz (Sec. 3.1.2). Table 5 shows analyses for vuggy interchondrule glass as well as for vuggy glass in an adjacent chondrule interior. The two analyses are similar and feldspathic, with notably higher silica and lower soda content than analyses of bulk interchondrule glass in Tieschitz (Table 5). Although generally feldspathic, the glass in NWA 5421 contains small amounts of Fe and Mg and is deficient in cations/8O (4.74-4.76) compared to stoichiometric feldspar (5.00) (Table 5).

3.7.3. NWA 11351 spotted matrix

This chondrite contains good examples in Lithology A of "spotted matrix", including material that chemically resembles feldspar (the spots) inside olivine (Sec. 3.1.5). Table 5 provides analyses of phases in NWA 11351 for the area shown in Fig. 2r. EBSD indicates that the feldspar and olivine areas are poorly crystalline and mostly do not index, yet *EDS* analyses indicate stoichiometric compositions, with 4.98±0.02 cations/8O for "feldspar" and 3.00±0.01 cations/4O for "olivine" (Table 5). The "feldspar" has slightly variable Na/(Na+Ca) (0.92±0.05 at., N=4) and contains appreciable Fe, Mg, and Ni, whereas the "olivine" has uniform Fe/(Fe+Mg) (0.29±0.01, N = 6) and contains appreciable Ni (Table 5). Compositions resemble spotted matrix phases in the Lut chondrites (Hutson et al., 2014).

4. Discussion

4.1. Deformation temperature

4.1.1. Slip system systematics

An overall trend for misorientation rotation axis directions in olivine is apparent when combining data for different meteorites and lithologies (Fig. 6), consistent with systematic variations in slip systems that were activated during deformation (Sec. 3.3). For olivine, slip occurs primarily in the **c** <001> or **a** <100> directions. Lower temperature favors **c**-type slip and higher temperature favors **a**-type slip (e.g., Raleigh, 1968; Carter and Ave'Lallemant, 1970; Carter, 1971; Phakey et al., 1972; Green, 1976; Gueguen and Nicolas, 1980; Mainprice and Nicolas, 1989; Tommasi et al., 2000; Karato et al., 2008; Tielke et al., 2016). Slip systems also can be affected by other variables such as strain rate or deviatoric stress (Raleigh, 1968; Carter and Ave'Lallemant, 1970; Goetze, 1978; Karato et al., 2008; Tielke et al., 2016), pressure (Carter, 1971; Carter and Ave'Lallemant, 1970), and water content (Karato et al., 2008).

We infer that temperature was the main control on slip in olivine during shock deformation in ordinary chondrites. Strain rate and pressure dependencies in the **c**- to **a**-slip transition have a counteracting tendency based on experiments (Carter, 1971; Carter and Ave'Lallemant, 1970). Extrapolating to shock events with high strain rate and high pressure, the transition from **c**- to **a**-type slip will occur at roughly the same temperatures as in experimental studies at lower strain rates and lower pressures (Ruzicka and Hugo, 2018). Further, although water will promote more **c**-type slip in olivine (Karato et al., 2008), it probably did not control the activation of olivine slip systems in ordinary chondrites. Ordinary chondrites range from "wetter" Type 3 to "drier" Type 6 (Jarosewich, 1990). There is no evidence for a systematic change in olivine slip system that would correspond to this difference—Type 3 and Type 6 chondrites as groups overlap in their misorientation rotation axis directions and $R_{2\text{-}10}$ values (Fig. 6).

4.1.2. Model deformation temperature

A model deformation temperature can be derived by relating the $R_{2\text{-}10}$ parameter, which corresponds to the proportion of **c**-type and **a**-type slip in olivine, to absolute temperature using "benchmarks", or meteorites with well-characterized deformation temperatures. We use the Morrow County (L6 S5) chondrite as the low-temperature benchmark, and the olivine-pigeonite ureilite NWA 11993 as the high-temperature benchmark.

Morrow County olivine has $R_{2\text{-}10} = 0.399$ and an estimated effective deformation temperature of 700±100 °C, based on: (1) the presence of dislocations with mainly **c**-type (**b**=[001]) but also **a**-type (**b**=[100])

slip (Ruzicka et al., 2015; Ruzicka and Hugo, 2018); (2) experimental data that place the **c**-type to **a**-type transition at ~700-800 °C (Carter and Ave'Lallemant, 1970; Carter, 1971; Green, 1976; Gueguen and Nicolas, 1980; Mainprice and Nicolas, 1989); and (3) the shock temperature increase calculated from Hugoniot data of an S5 ordinary chondrite shocked to ~30-45 GPa pressure (Stöffler et al., 1991) of either ~600-900 °C (Schmitt, 2000) or ~630-1130 °C (Hu and Sharp, 2022), with pressure in naturally shocked rocks probably being lower (Sharp and DeCarli, 2006), and therefore shock temperatures on the lower end of these values. An error of ±100 °C is assumed, to account for the temperature variations noted above and to be consistent with data for other meteorites such as Bruderheim (L6 S4) and Leedey (L6 S4), which appear to have been shocked with deformation temperatures as low as ~600°C (Ruzicka and Hugo, 2018).

Coarse olivine in ureilite NWA 11993 has $R_{2\text{-}10} = 0.879$ (Frye, 2022) and an estimated deformation temperature of 1225±75 °C, based on: (1) a best estimate equilibration temperature of ~1220-1230 °C for $Fa_{22.6 \pm 0.7}$ olivine cores (MBD, 2023) in NWA 11993, using the geothermometry formulation of Singletary and Grove (2003); (2) mantle equilibration temperatures of ~1160-1300 °C for various ureilites (Singletary and Grove, 2003; Herrin et al., 2010); and (3) the inference that most ureilites were shocked at magmatic temperatures during catastrophic disruption and global unroofing of the ureilite parent body (Herrin et al., 2010; Rai et al., 2020). An error of ±75 °C is assumed, to account for the variations in temperatures quoted above.

Assuming a linear relationship between the benchmarks, the model effective deformation temperature and associated error are respectively (Ruzicka and Hugo, 2022a):

$$T_{deform}(^{\circ}C) = 1091.5x(R_{2-10} - 0.399) + 700 \quad (5a)$$

$$T_{err}(^{\circ}C) = 0.0476x(1225 - T_{deform}) + 75 \quad (5b)$$

The model temperatures should be applicable to olivine in shock-deformed rocks with T_{deform} ~600-1250 °C, if temperature was the main control affecting slip systems. Below the lower limit, temperatures may not be reliable as there will be little change in slip system, and above the upper limit, temperatures may not be reliable because no distinction is made between the <001> and <010> directions for $R_{2\text{-}10}$. Also, because resolved shear stress might favor different slip systems depending on grain orientations relative to maximum and minimum stress directions, analysis of a relatively large number of olivine grains with different orientations will lead to the most meaningful T_{deform} values. Thus, larger datasets, with more grains and more grain orientations, will give more accurate results. The T_{err} values should be considered as the largest likely uncertainty assuming temperature-controlled slip, provided the dataset is sufficiently large.

Model deformation temperatures estimated based on averaged large map (*LAM* and *miniLAM*) data for each chondrite lithology are given in Table 2. The data are highly consistent: T_{deform} = 945±17 °C (±1 SD) for eight Type 3 lithologies excluding NWA 11351, and T_{deform} = 715±1 °C for Lithology A and B of NWA 11351. The composite ±1 SD values given here, which are related to repeatability, are much smaller than the T_{err} values (Eq. [5b]), which are related to accuracy. These data pertain exclusively to the coarser olivine grains (≥5-15 μm across) in chondrules and the grains outside chondrules that were possibly derived from them.

Most Type 3 chondrites have T_{deform} values of ~950 °C, similar to those of Kernouvé (H6), Miller Range (MIL) 99301 (LL6), and Portales Valley (H6). These Type 6 chondrites were inferred to have been deformed at temperatures estimated as >700-800 °C and up to ~1000 °C (Ruzicka and Hugo, 2018), in agreement with the T_{deform} values given here.

4.1.3. Implications of deformation temperature

The relationship between olivine $R_{2\text{-}10}$ and T_{deform} to $GOS_{d>50}$, the main EBSD deformation intensity parameter, is shown in Fig. 11 for various chondrites. Most of the Type 3 chondrites, which range in average $GOS_{d>50}$ values between ~1.0-2.7° and which correspond to weak-moderate (S1-S3) shock deformation, have relatively constant $R_{2\text{-}10}$, whereas the two NWA 11351 lithologies have the highest mean $GOS_{d>50}$ values (~3.5-3.8°) and the lowest $R_{2\text{-}10}$ values (Fig. 11). In terms of both $R_{2\text{-}10}$ and $GOS_{d>50}$, NWA 11351 falls within the "*Group 1*" field, previously identified as chondrites strongly shocked from cold ambient temperature (Ruzicka et al., 2015; Ruzicka and Hugo, 2018). The clear implication is that slip systems and $R_{2\text{-}10}$ were effectively changed in a strong late shock experienced by NWA 11351. This is supported by fabric data for opaque minerals in NWA 11351 that require a late, significant shock, to create an essentially identical petrofabric for all lithologies (Sec. 3.5). The data for NWA 11351 imply that an S4 shock stage is sufficient to change slip systems in olivine.

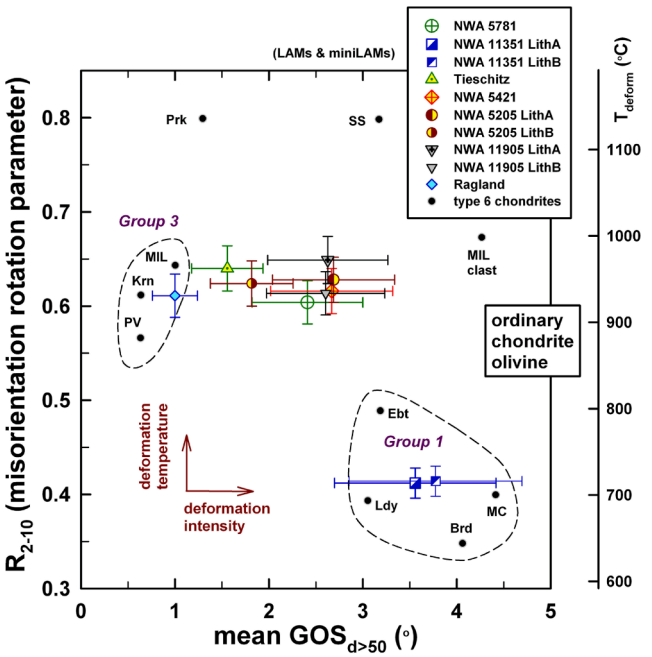

Fig. 11. Relationship between $R_{2\text{-}10}$ parameter ("relative deformation temperature") and mean $GOS_{d>50}$ parameter ("deformation intensity") for olivine in the Type 3 chondrites of this study (averaged LAM and miniLAM data) compared to Type 6 chondrites (LAM data). Error bars for Type 3 chondrites are "representative errors" based on the repeatability of results in LAM and miniLAM datasets. T_{deform} is based on Eq. (5a) in the Text. *Group 1* and *Group 3* are the designations of Ruzicka and Hugo (2018) and Hugo et al. (2020), modified to exclude Park from *Group 3* (see Text). Abbreviations and data sources: same as in Fig. 4 and Fig. 6.

There is additional evidence that a shock stage approaching S4 intensity was required to change olivine slip systems. In NWA 11905, the fine-grained olivine-rich object located at the edge of Lithology A has a change in the proportion of misorientation rotation axis directions together with lower deformation with increasing distance from the clast boundary (Fig 3c-e; Sec. 3.1.2). This pattern cannot be explained by texture or crystal orientation effects as these are not significantly different with distance from the clast edge. Instead, it suggests that an earlier event recorded in the less-deformed interior was locally overprinted by a lower-temperature deformation ($R_{2\text{-}10}$ = 0.458 and T_{deform} = 765±97 °C) recorded in the more deformed edge associated with the incorporation of Lithology A as a clast into Lithology B. The shock stages for NWA 11905 Lithology B are in the S3-S4 range (Fig. S1, Table 2), which implies that shock of corresponding intensity could have locally changed slip systems in olivine at the clast edge. Moreover, a later post-agglomeration shock is implied for NWA 5781 (*CSS* = S3), based on the foliation of metal and troilite grains (Sec. 3.5). However, there is no evidence that $R_{2\text{-}10}$ for NWA 5781 was globally or locally changed.

Altogether, these data suggest that effective overprinting for olivine slip systems requires global shock intensities that were between those experienced by NWA 5781 (*CSS* = S3) and NWA 11351 (*CSS* = S4).

Another implication of Fig. 11 is that olivine deformation temperature is not solely the result of shock heating. If shock heating alone were responsible for the deformation temperatures, temperatures would correlate with shock stage (Stöffler et al., 1991; Schmitt, 2000). Instead, more strongly shocked (S4-S5) Type 3 and Type 6 chondrites have lower deformation temperatures than less-shocked (S1-S3) chondrites. This can be explained if the less-strongly-shocked chondrites were warm for some reason other than shock compression, such as pre-shock metamorphic heating for warm Type 6 chondrites (Ruzicka et al., 2015; Ruzicka and Hugo, 2018), or already-warm chondrules that became deformed for Type 3 chondrites (Metzler, 2012). For more-strongly shocked (S4-S5) chondrites, shock reheating is likely responsible for the observed deformation temperatures, as it generally agrees with estimates from Hugoniots and is consistent with younger ^{39}Ar-^{40}Ar ages (Ruzicka et al., 2015; Ruzicka and Hugo, 2018).

Given good evidence for shock overprinting in NWA 11351, one can ask what effect multiple impacts might have on $R_{2\text{-}10}$ for other Type 3 chondrites that show a warm deformation signature. There are two possibilities. Either $R_{2\text{-}10}$ was established in (1) one event, or (2) multiple events.

If one event, one could surmise deformation at a temperature of ~950 °C. This is much higher than the temperature estimated for metamorphic heating of Type 3 ordinary chondrites (Dodd, 1981; Huss et al., 2006). It cannot be caused by shock heating, owing to the low temperature increases associated with S1-S3 shocks (Stöffler et al., 1991; Schmitt, 2000; Hu and Sharp, 2022). The elevated temperature could instead be caused by the collision of already warm chondrules as they were cooling from melt temperatures during accretion (Metzler, 2012). The high degree of consistency in averaged $R_{2\text{-}10}$ and T_{deform} values for most Type 3 chondrites could be explained by a single, dominant event such as accretion, which would have been experienced by all chondrules under the same conditions.

However, it is also possible that there were multiple events at different deformation temperatures that averaged to $R_{2\text{-}10}$ values that correspond to T_{deform} ~950 °C. This could arise, for example, with chondrule collisions occurring at higher temperatures (>1000 °C) pre-accretion, but with chondrites then affected by later shocks post-accretion at lower temperatures (<900 °C). Although this might explain variations in chondrite shock stages and *GOS* values, it does not readily explain the high degree of consistency in T_{deform} values for most Type 3 chondrites (945±17 °C for eight lithologies), and the invariance of T_{deform} over a range of low-moderate *GOS* values (Fig. 11), which implies that T_{deform} was not much affected by variations in deformation history involving low-moderate intensity shock events. Another possibility is that chondrules collided at different pre-accretion temperatures (>1000 °C and <900 °C), averaging out to a more middling value. This is possible, but again, to obtain consistency on a chondrite scale for different lithologies requires a consistent distribution of temperatures that always average to nearly the same value.

It appears that $R_{2\text{-}10}$ is not very sensitive to the effects of possible multiple low-to- moderate intensity shock events, and that the data can be largely explained by a dominant deformation associated with accretion close to a temperature of ~950 °C. However, as discussed below (Sec. 4.3), there is evidence that chondrules could have been deformed at higher temperatures in addition to deformation at the time of accretion. If so, this would tend to lower the effective accretion temperature somewhat.

4.2. Post-deformation annealing

In this section, we explore evidence for post-deformation annealing based on *GOS* data and comparisons to TEM evidence. Annealing is considered separately for larger and smaller length scales.

4.2.1. Larger-scale annealing

For olivine in Type 6 chondrites, Ruzicka and Hugo (2018) noted that chondrites that experienced microstructural recovery as evidenced from TEM observations of picket-fence subgrain boundaries (Ruzicka et al., 2015) also contained a distinctive EBSD-scale deformation signature, composed of occasional larger, elevated-*GOS* grains amidst many low-*GOS* grains, with the elevated-*GOS* grains containing subgrain boundaries with sharp changes in orientation separating otherwise weakly-deformed parts of the grains. The picket-fence subgrain boundaries seen by TEM that are produced by recovery (Ruzicka et al., 2015) have as their analogue these larger subgrain boundaries identified by EBSD, and the weakly-deformed character of elevated *GOS* grains outside the subgrain boundaries supports the interpretation that these subgrain boundaries were produced by recovery (Ruzicka and Hugo, 2018). The presence of the occasional elevated-*GOS* grains in annealed chondrites results in high *GOS* skew, but the effect is most apparent for large (d>50 μm) grains as these are the grains that mostly have elevated *GOS*. Ruzicka and Hugo (2018) concluded that $Sk_{d>50}$ (as designated here) can be used as an annealing parameter, but that high $Sk_{d>50}$ also can be produced by an admixture of more deformed material in weakly deformed material by impact mixing. This leads to potential ambiguity in how to interpret $Sk_{d>50}$.

Comparing *Sk* values for grains of different size ranges can help distinguish between annealing and impact-mixing effects. The inset in Fig. 7b shows the *Sk*-grain size trend expected for recovery caused by post-deformation dislocation climb and annealing (Ruzicka and Hugo, 2022b). Recovery will cause dislocation annihilation within grains, removal of dislocations from grain boundaries, and recovery-induced subgrain boundaries within grains. These recovery processes reduce *GOS*, but at different rates for different grain sizes. *GOS* and *Sk* values are reduced quickly in small grains because dislocations have a small distance to travel to grain margins. Further, *GOS* and *Sk* reduction is slowed by the formation of subgrain boundaries, which preserve *GOS* and *Sk* during dislocation recovery (Ruzicka and Hugo, 2018). Both effects should scale with grain size; thus, annealing can be identified for grain populations that have $Sk_{d>50} > Sk_{d15\text{-}50} > Sk_{d5\text{-}15} > Sk_{d<5}$.

In contrast, there is no reason to expect that shock deformation will result in such systematics. Indeed, if deformation results in local brecciation together with plastic deformation, one might expect the opposite pattern to prevail, with some highly deformed small grains causing an increase in *Sk* with smaller grain size, as is often seen (Fig. 7).

The only meteorites that show the expected positive *Sk*-grain size trend for annealing on the grain size scale examined in Fig. 7 are Portales Valley, Kernouvé, and the MIL 93301 host (Fig. 7b). These three meteorites, together with Park, were suggested to have been annealed following deformation (Ruzicka and Hugo, 2018), but the data for Park are inconsistent with the *Sk*-grain size model for annealing given here and there are other data that argue against annealing in Park (see below). Similarly, none of the Type 3 chondrites would seem to fit the annealing model for grain sizes of $d \geq$ 5-15 μm, as none show the expected positive trend in Fig. 7a.

Ratios between *Sk* values for different d bins are a more compact way to express *Sk-d* trends. For the *LAMs* and *miniLAMs* obtained in this work, the smallest bin that can be effectively sampled is the $d_{5\text{-}15}$ bin, but it has the largest number of grains and the statistically best-defined *Sk* values. Thus, considering the predicted positive *Sk-d* trend for annealing, we suggest *GOS* skewness ratio $Sk_{d>50}/Sk_{d5\text{-}15}$ with values > 1 (if outside errors) as a robust annealing indicator.

The relationship between $Sk_{d>50}$ (previous annealing metric—Ruzicka and Hugo, 2018) and $Sk_{d>50}/Skd_{5\text{-}15}$ (proposed large-scale annealing metric) for various chondrites is shown in Fig. 12a. We assert that $Sk_{d>50}/Skd_{5\text{-}15} > 1$ fits a condition of annealing, whereas $Sk_{d>50}$ alone is a measure of *GOS* heterogeneity in coarse grains that might or might not be related to annealing. In this interpretation, none of the Type 3 chondrites were significantly annealed on the scale being measured (d≥5-15 μm) in large area maps, and only three Type 6

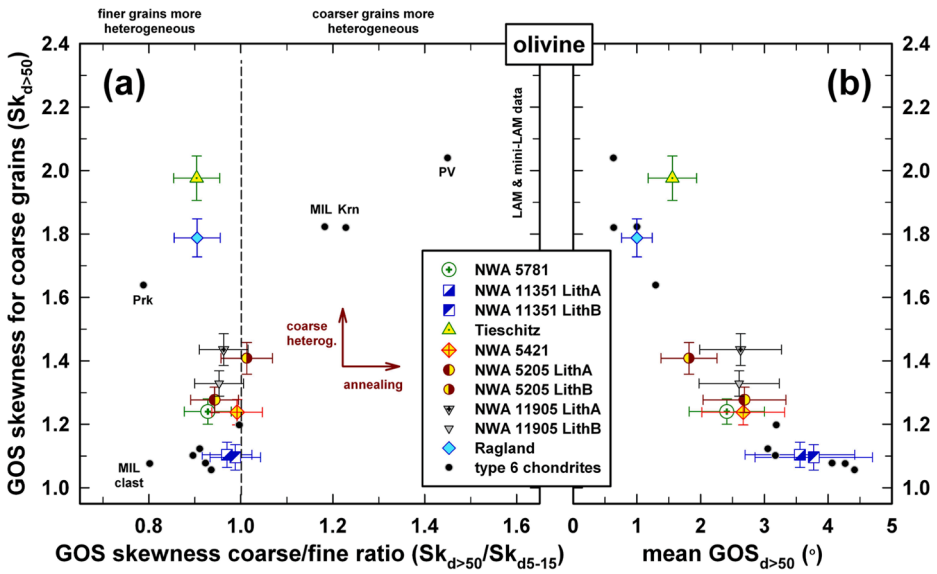

Fig. 12. *GOS* systematics. *GOS* skewness for coarse grains ($Sk_{d>50}$) vs. **(a)** *GOS* skewness ratio ($Sk_{d>50}/Sk_{d5-15}$) and **(b)** mean $GOS_{d>50}$. Data are shown for the Type 3 chondrites of this study (averaged *LAM* and *miniLAM* data) compared to Type 6 chondrites (*LAM* data). Error bars for Type 3 chondrites are "representative errors" based on the repeatability of results in *LAM* and *miniLAM* datasets. The dashed line in part (a) delimits an "annealed" from "non-annealed" condition. Abbreviations and data sources: same as in Fig. 4 and Fig. 6.

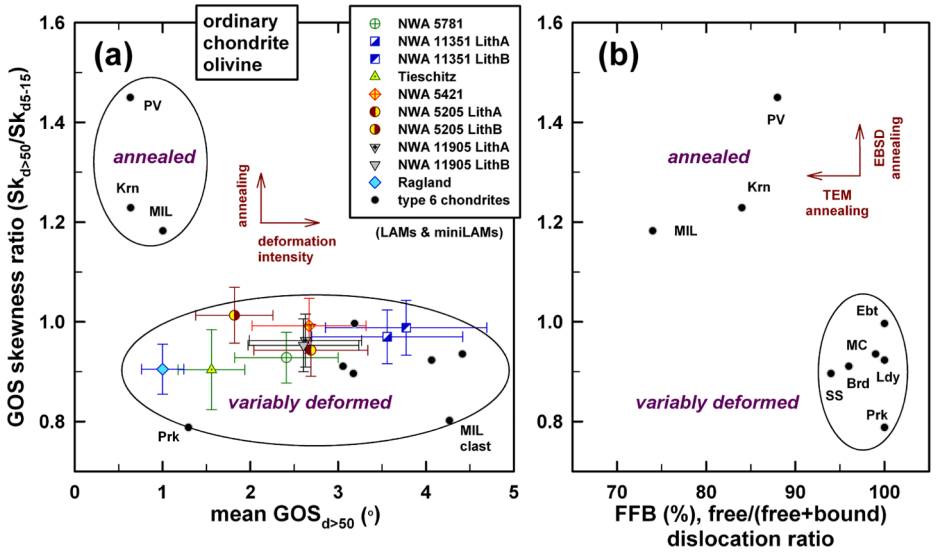

Fig. 13. Relationship between annealing and deformation parameters. (a) GOS skewness ratio ($Sk_{d>50}/Sk_{d5-15}$) vs. mean $GOS_{d>50}$ (EBSD, Type 3 and Type 6 chondrites) and (b) GOS skewness ratio ($Sk_{d>50}/Sk_{d5-15}$) vs. Free/(Free+Bound) dislocation (FFB) ratio in olivine (TEM, Type 6 chondrites only). EBSD data for the Type 3 chondrites are based on averaged LAM and miniLAM data and error bars are "representative errors" based on the repeatability of results in these maps. For Type 6 chondrites, GOS values are based on LAM EBSD data, and dislocation FFB values are based on TEM data from Ruzicka et al. (2015) and Hugo et al. (2020). The apparent trend for the three annealed chondrites in part (b) is not meaningful as TEM error bars overlap. Abbreviations and other data sources: same as in Fig. 4 and Fig. 6.

chondrites previously identified as having been recovered based on TEM evidence— Portales Valley, MIL 99301 host, and Kernouvé (Ruzicka et al., 2015)— experienced significant annealing as measured by EBSD (Fig. 13a). These three meteorites have high $Sk_{d>50}$, but so do three others (Park, Tieschitz, and Ragland) that are not consistent with annealing according to the $Sk_{d>50}/Skd_{5-15}$ metric (Fig. 12a). For the latter three meteorites, we suggest that *GOS* heterogeneity was not caused by annealing.

A relevant consideration here is the overall tendency for $Sk_{d>50}$ to increase as mean $GOS_{d>50}$ decreases (Fig. 12b). This trend is well defined and includes the three chondrites with $Sk_{d>50}/Sk_{d5-15}$ >1 ("annealed") and many more with $Sk_{d>50}/Sk_{d5-15}$ <1 ("non-annealed") (Fig. 12b), so it does not seem to reflect annealing alone, or even primarily. Instead, we suggest that the trend in Fig. 12b is caused by two entirely different heterogeneity effects: 1) incomplete recovery, which causes the "annealed chondrites" to have low *GOS* overall, but residual deformation concentrated mainly in some larger grains, and 2) deformation heterogeneity not produced by annealing, which will be more sensitively recorded in progressively less-shocked "non-annealed chondrites". Provided some more highly deformed grains are present, such as might be caused by heterogeneities during shock, or by an impact admixture of more deformed grains, *GOS* skew for progressively more weakly-deformed chondrites will better record the presence of the deformed grains, because comparatively few deformed grains are

needed to keep mean *GOS* elevated relative to median *GOS* and to increase skew. In other words, heterogeneity is more evident when overall *GOS* is low. If these interpretations are correct, it indicates elevated $Sk_{d>50}$ values do not necessarily indicate post-deformation annealing.

TEM data support the validity of $Sk_{d>50}/Sk_{d5\text{-}15}$ as a superior large-scale annealing metric. In Fig. 13, *GOS* skewness ratio ($Sk_{d>50}/Sk_{d5\text{-}15}$) is plotted against mean $GOS_{d>50}$ and Free/(Free+Bound) (*FFB*) dislocation ratio in chondrites. The *FFB* ratio is a TEM-derived annealing metric that quantifies the proportion of dislocations not associated with subgrain boundaries, with lower values indicative of more dislocation recovery (Goetze and Kohlstedt, 1973; Ruzicka et al., 2015). Three Type 6 chondrites, Portales Valley, Kernouvé, and MIL 99301 host, are designated as "annealed" in Fig. 13, because they have low mean $GOS_{d>50}$, low *FFB*, and elevated mean $Sk_{d>50}/Sk_{d5\text{-}15}$, all consistent with significant post-deformation recovery. Other chondrites, including all the Type 3 chondrites of this study, are designated as "variably deformed" in Fig. 13, because they have variable mean $GOS_{d>50}$, high *FFB* ratios where measured, and low mean *GOS* skewness ratios ($Sk_{d>50}/Sk_{d5\text{-}15}$). The consistency between EBSD and TEM evidence in Fig. 13 is powerful evidence for the validity of the *GOS* skewness ratio ($Sk_{d>50}/Sk_{d5\text{-}15}$) as an annealing metric.

With this improved annealing metric, Park now fits into the variably deformed group (Fig. 13), as opposed to annealed group based on $Sk_{d>50}$ alone. In fact, Park has the lowest *GOS* skewness ratio ($Sk_{d>50}/Sk_{d5\text{-}15}$) of any chondrite and one of the highest *FFB* ratios (Fig. 13), making it clear it was not significantly annealed. Thus, Park should be removed from the "*Group 3*", annealed chondrites of Ruzicka and Hugo (2018). It is now apparent that the high $Sk_{d>50}$ value for Park is caused by deformation heterogeneity not caused by annealing. EBSD maps for Park show that most deformation in this chondrite is localized in zones associated with fractures, a pattern unlike that shown in what are interpreted as truly annealed chondrites such as Portales Valley, MIL 99301 host, and Kernouvé.

4.2.2. Smaller-scale annealing

Although there is no evidence that the Type 3 chondrites experienced microstructural recovery on larger grain scales ($d \geq$5-15 μm grains), there is evidence for limited annealing on a small ($d <$5 μm, average $d \sim$2 μm) scale. Fig. 9 and Table 4 present olivine data for Type 3 chondrites obtained using high spatial resolution data for matrix and adjacent chondrules. In Fig. 9a, regions A, B, C and D are defined based on whether skewness ratios are >1 or <1 for different grain sizes. Region A would be consistent with an annealing model on scales from $d <$5 μm up to $d =$50 μm, and is not populated, suggesting a lack of widespread annealing. Region B would be consistent with annealing on a $d =$5-50 μm scale but not $d <$5 μm scale and is not populated. Region C would be consistent with annealing on a $d <$5 μm scale but not $d =$5-50 μm scale, and is populated with Tieschitz matrix and chondrules, Ragland chondrules, and locally for NWA 5205 Lithology B chondrules. The case for small-scale annealing is strong for Tieschitz, as it has low values of $GOS_{d<5}$ in addition to low skewness ratio for $Sk_{d<5}/Sk_{d5\text{-}15}$, and seven of eight high-resolution maps for it are consistent with recovery on a small scale (Fig. 9, Table 4). Region D in Fig. 9a has increasing skewness with decreasing grain size which is opposite to that expected for annealing, and is populated with NWA 5205 Lithology B matrix, NWA 5205 Lithology A matrix and chondrules, NWA 5781 matrix and chondrules, Ragland matrix, and NWA 5421 chondrules. Thus, based on skewness ratios alone there is evidence for annealing on a small (<5 μm) scale in some chondrites and not others.

However, the correlation seen in Fig. 9b between $GOS_{d<5}$ and $Sk_{d<5}/Sk_{d5\text{-}15}$ for all lithologies except for Ragland matrix and chondrules provides good evidence that all these lithologies could have experienced some recovery on a small (d<5 μm) scale. This correlation implies that grains become less deformed and more uniformly deformed as they become smaller, as expected for post-deformation annealing. We suggest that all the chondrites could have experienced small-scale annealing, but that in many it was not sufficient to overcome a tendency for higher skew in smaller grain sizes produced by some other effect (likely impact deformation). The offset of Ragland matrix and chondrules to higher $GOS_{d<5}$ compared to other lithologies for a given $Sk_{d<5}/Sk_{d5\text{-}15}$ (Fig. 9b) could indicate an additional deformation event that increased *GOS* somewhat, but Ragland too has evidence for small-scale annealing effects.

4.3. Thermal history and effective accretion temperature

Evidence for annealing on a small scale in Type 3 chondrites (Sec. 4.2) has implications for thermal histories following deformation and implications for effective accretion temperatures. Given that evidence for recovery in olivine is found for the smallest grain size population (d<5 μm bins) which has an average grain diameter $d \sim$2 μm, or ~1 μm radius, a critical length scale for dislocation mobility of ~1 μm is implied. This length scale can be combined with the rate constants for dislocation recovery to constrain timescales. Farla et al. (2011) annealed fine-grained olivine and quantified dislocation removal during annealing. This removal can occur by climb involving annihilation of dislocations of opposite sign, or by the climb of dislocations out of grains. Although Farla et al. (2011) assumed a large role for annihilation, removal at grain boundaries could also have occurred and we infer that this was important in chondrites. Thus, we considered the movement of dislocations out of grains by diffusion (strictly, it is the atoms in the crystal lattice containing the dislocations that must diffuse) and compare this to other diffusing species for reference. Fig. 14 applies diffusion models to evaluate post-deformation annealing conditions for chondrules in Type 3 chondrites. Temperatures considered range from subsolidus to magmatic; experiments suggest peak temperatures for chondrules of ~1400-1850 °C (Hewins et al., 2015).

Fig 14a shows the time needed to diffuse out of spherical olivine grains of different sizes for different species. This includes (1) dislocation climb for dislocations (1-μm-radius grains, dashed orange line) (incorporating data from Farla et al., 2011); (2, 3) Fe-Mg interdiffusion (15-μm-radius and 20-μm-radius grains, thick and thin blue solid lines respectively) (Dohmen and Chakraborty, 2007); and (4) Si self-diffusion (1-μm-radius grains, black dotted-dashed line) (Costa and Chakraborty, 2008). Silicon diffusion is relatively slow but together with oxygen is believed to be relevant for olivine plasticity and recovery effects (Karato et al., 1993; Costa and Chakraborty, 2008; Fei et al., 2012; Boioli et al., 2015), whereas Fe-Mg interdiffusion is relatively fast (Dohmen and Chakraborty, 2007) and provides a constraint as it can be compared to Fe-Mg zoning observable in *BSE* and *EDS* map images.

For temperatures corresponding to T_{deform} (~900-1000 °C) for most Type 3 chondrites (Sec. 4.1), the implied duration for significant dislocation recovery in 1-μm-radius grains is similar to that needed for Fe-Mg equilibration in olivine grains with radius ~10-20 μm (Fig. 14a). In contrast, at these temperatures significant Si equilibration in 1-μm-radius olivine grains would require 2-3 orders of magnitude longer equilibration times (Fig. 14a).

At magmatic temperatures (1400-1850 °C), the implied durations for significant dislocation mobility in olivine grains with radius of 1 μm is roughly like that needed for Si diffusion, and like that needed for Fe-Mg equilibration in 10-μm-radius grains (Fig. 14a). All the timescales are roughly consistent, suggesting that a ~1 μm scale of dislocation mobility at magmatic temperatures is compatible with a ~10 μm scale of Fe-Mg diffusion and with an important role for Si diffusion in recovery.

If chondrules were deformed while they were cooling, the constraints on diffusion timescale for dislocation climb can be recast in terms of the cooling rates needed to explain measurable dislocation recovery. Fig. 14b shows the results. The curve was calculated over 10 °C cooling intervals combining temperature and diffusion time needed. If cooling rates were too fast (to the right of the curve), there would be insufficient recovery, whereas if cooling rates were too slow (to the left of the curve), there would be too much recovery. We consider two temperature cases

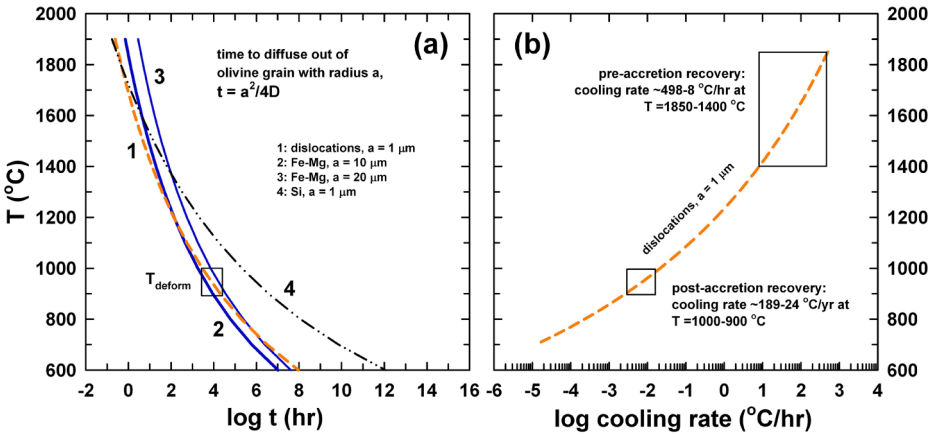

Fig. 14. Evaluation of post-deformation annealing conditions. (a) Model time to diffuse out of a spherical olivine grain with radius 'a' assuming $(Dt/a^2)^{0.5} = 0.5$ (D= diffusion coefficient, t = time), which brings the initial concentration at r/a = 0.5 (midpoint of radial position in grain) down to about 38% of the initial value (Crank, 1975, p.30) ("significant diffusion"). Curves are shown for: 1= dislocations, based on recovery data for olivine assuming 2nd order kinetics from Farla et al. (2011) (dashed orange line); 2, 3 = Fe-Mg interdiffusion in olivine (dry and Fe-bearing) from Dohmen and Chakraborty (2007) (solid blue lines); 4 = Si self-diffusion in olivine (hydrated but not saturated, Fe-bearing olivine) from Costa and Chakraborty (2008) (black dotted-dashed line). The box shows the range in implied diffusion time assuming significant olivine recovery in 1-μm-radius (2-μm-diameter) olivine grains as implied for some Type 3 chondrites, and assuming temperatures of 1000-900 °C, the model deformation temperatures for most Type 3 chondrites. (b) Cooling rate corresponding to condition 1 in part (a) (significant dislocation recovery in olivine). Two boxes show ranges in implied cooling rates for two different cases, including pre-accretion recovery (chondrules at magmatic conditions) and post-accretion recovery (chondrules at T_{deform}). See Text.

in Fig. 14b. "Post-accretion recovery" corresponds to T_{deform} = 900-1000 °C, and "pre-accretion recovery" corresponds to magmatic temperatures (1400-1850 °C).

The calculated post-accretion cooling rates are ~189-24 °C/yr, or roughly ~100 °C/yr (Fig. 14b). This is very slow. For comparison, experimental constraints for chondrule cooling rates at magmatic temperatures based on textures and olivine zoning are ~10-1000 °C/hr (Hewins et al., 2015), a factor of 876-87,600 higher than the calculated rates at 900-1000 °C. Some slowing of cooling after accretion would be expected, but the very low cooling rates are difficult to reconcile with other data for Type 3 ordinary chondrites. For instance, such chondrites contain temperature-sensitive components including pre-solar grains, organic matter, and hydrous phases that are easily destroyed by thermal metamorphism (Huss et al., 2006), and contain abundances of volatile elements such as In and Ar (Huss et al., 2006) that imply low accretion temperatures. Furthermore, structural states of feldspathic matter (chiefly glass, but also feldspar of low-temperature structural state) in Type 3 chondrites imply formation at low temperatures (Guimon et al., 1985). Although small amounts of temperature-sensitive and volatile materials could have been added to chondrites during brecciation events, abundant feldspathic glass in chondrules cannot be easily explained this way. Thus, it is difficult to reconcile the inferred amount of recovery with post-accretion annealing.

Alternatively, chondrules may have experienced some recovery while they were cooling during crystallization. Deformation would be required, such as might occur by collisions between chondrules in the nebula, as suggested by the presence of cratered or indented chondrules (e.g., Fig. 3k) (Gooding and Keil, 1981; Grossman et al., 2000) and by compound chondrules (e.g., Fig. 3b) (Gooding and Keil, 1981; Connolly et al., 1994; Wasson et al., 1995; Ciesla et al., 2004; Hubbard 2015). For pre-accretion recovery, calculated cooling rates are ~498-8 °C/hr between 1850-1400 °C (Fig. 14b). This is consistent with well-established best estimates of chondrule cooling rates (1000-10 °C/hr) during crystallization (Hewins et al., 2005). Thus, limited recovery during chondrule crystallization can explain the deformation-annealing data for Type 3 chondrites. Cooling rates might still decrease significantly after accretion because of thermal buffering caused by warm chondrules, but the rates may have been too fast to result in appreciable recovery in olivine, and too fast to destroy temperature-sensitive components or to prevent feldspathic glass from forming.

Together with other data we have presented, this suggests a complex scenario whereby chondrules collided prior to accretion, annealed somewhat while in space, and then were deformed again more substantially at the time of accretion. This scenario might explain why the signature for recovery (decreasing $Sk_{d<5}/Sk_{d5\text{-}15}$ with decreasing $GOS_{d<5}$) appears to be superposed on what is interpreted as a contrary deformation signature ($Sk_{d<5}/Sk_{d5\text{-}15} > 1$) for many chondrites (Sec. 4.2.2). If this scenario is correct, it could indicate that the values for T_{deform} in S1-S3 Type 3 chondrites are to some extent indeed representing more than one deformation event (Sec. 4.1.3), namely one or more higher-temperature pre-accretionary events and a dominant, lower-temperature accretion event.

To result in generally consistent T_{deform} values of ~950 °C while still allowing minor pre-accretion deformation implies accretion at an effective temperature closer to 900 °C than to 1000 °C. Although an exact accretion temperature is difficult to determine, we suggest that chondrules in Type 3 LL and H/L chondrites could have accreted at effective temperatures of ~900-950 °C, somewhat less than the average T_{deform} value of 945 °C for weakly shocked chondrites (Sec. 4.1.2), at temperatures just below the metal-troilite eutectic temperature, and close to the previously suggested accretion temperature for Tieschitz (~800 ± 100 °C) (Hutchison et al., 1979).

4.4. Formation of strongly and weakly clustered Type 3 chondrites

Here we examine the origin of Type 3 chondrite clustering textures. These textures were considered evidence for "hot accretion" (Hutchison et al., 1979; Metzler, 2012). In strongly clustered lithologies, evidence for impingement-related deformation is widespread, which implies nearly *in situ* deformation between chondrules (Sec. 3.1.2). In principle, this could be caused by chondrules that were mutually deformed during agglomeration, or by shock events following agglomeration that pushed closely spaced chondrules together and caused them to become peripherally deformed. The first possibility is favored, as it is consistent with olivine slip system analysis, including data that suggests that slip systems were established by deformation between warm chondrules during agglomeration (Sec. 4.1.3), as well as specific instances of impingement-related deformation that appears to have occurred at an elevated temperature of deformation (e.g., Fig. 2c). This supports the idea that strong clustering textures were produced by the mutual

deformation of warm chondrules during accretion. In weakly clustered lithologies, the same deformation signatures are seen, but impingement deformation between chondrules cannot be so clearly established (Sec. 3.1.3).

Brecciation events may have created weakly clustered lithologies from strongly clustered lithologies (Metzler, 2012). Indeed, in weakly clustered chondrites such as NWA 5205 Lithology B, Ragland, and NWA 11351 Lithology B, many lithic and mineral clasts are visible (Fig. 3f, 3m), suggestive of significant brecciation (Sec. 3.1.3). Weakly clustered chondrites have more fine-grained material ("matrix") between chondrules, including many mineral clasts and finer debris (Sec. 3.1.3). Thus, it appears that brecciation and admixture of fine debris, which itself could have been produced by brecciation, are consistent with the petrography of weakly clustered lithologies.

Figure 15 shows the relationship between cluster texture strength values (C_s) and different olivine EBSD metrics such as $GOS_{d>50}$, $R_{2\text{-}10}$, and $Sk_{d>50}/Sk_{d5\text{-}15}$. In general, there is little evidence that any of these metrics are strongly related to cluster texture strengths.

For instance, there is no obvious correlation between C_s and $GOS_{d>50}$ (Fig. 15a). NWA 11351 has lithologies with both the highest and lowest C_s values but both have the highest observed $GOS_{d>50}$ values (Fig. 15a). The high *GOS* values are certainly due in large part to a late strong shock that affected both lithologies, which re-oriented metal and troilite to form a foliation (Sec. 3.5). Excluding this meteorite, one might argue for a weak overall positive trend between C_s and $GOS_{d>50}$, but the trend is unconvincing (Fig. 15a). More obvious is that lithologies that such as NWA 11905 Lithology A and B, NWA 5205 Lithology A, and NWA 5421, have essentially identical $GOS_{d>50}$ values but vary greatly in cluster texture strength (Fig. 15a). Moreover, three other lithologies, including NWA 5205 Lithology B, Ragland, and Tieschitz, have notably low $GOS_{d>50}$ values but also vary greatly in cluster texture strength, from weak to strong (Fig. 15a).

Altogether, these data suggest that the formation of clustering textures (measured by C_s) did not depend much on the degree of intracrystalline plastic deformation (measured by mean $GOS_{d>50}$). Clearly, strong clustering texture did not require significant plastic deformation of olivine. The best example of this is Tieschitz, which has both low mean $GOS_{d>50}$ and high C_s (Fig. 16a). This meteorite has good examples of chondrules and grains "stuck partly into other chondrules", microfaulting, and bent twins in pyroxene (Fig. 2f), which suggest that both ductile and brittle deformation occurred. But plastic deformation within grains as recorded by EBSD and by optical microscopy is modest (mean olivine $GOS_{d>50}$ ~1.6°, shock stage S1).

From this, we infer that molding of chondrules to form cluster texture involved a somewhat plastic, somewhat rigid deformation, accompanied by brittle deformation and only modest crystal plastic deformation within silicates. During accretion under warm conditions (~900-950 °C, Sec. 4.3), chondrule mesostasis glass would have been above the glass transition temperature (~750-810 °C for plagioclase compositions; Arndt and Häberle, 1973). This means that it could have acted in a "rubbery" as opposed to "stiff" fashion during accretion, possibly protecting enclosed silicates from deformation, and helping to explain how even strongly clustered lithologies have only modest internal deformation.

Other strongly clustered lithologies such as NWA 5205 Lithology A, NWA 5421, and NWA 5781, experienced either stronger shocks or multiple weak shocks resulting in a final S2 or S3 shock stage. These shocks may have occurred during agglomeration or in post-agglomeration events. Judging from microtomography data for NWA 5781, metal and troilite grains could have been reoriented in a single shock event after agglomeration (Sec. 3.5). Thus, the data imply that

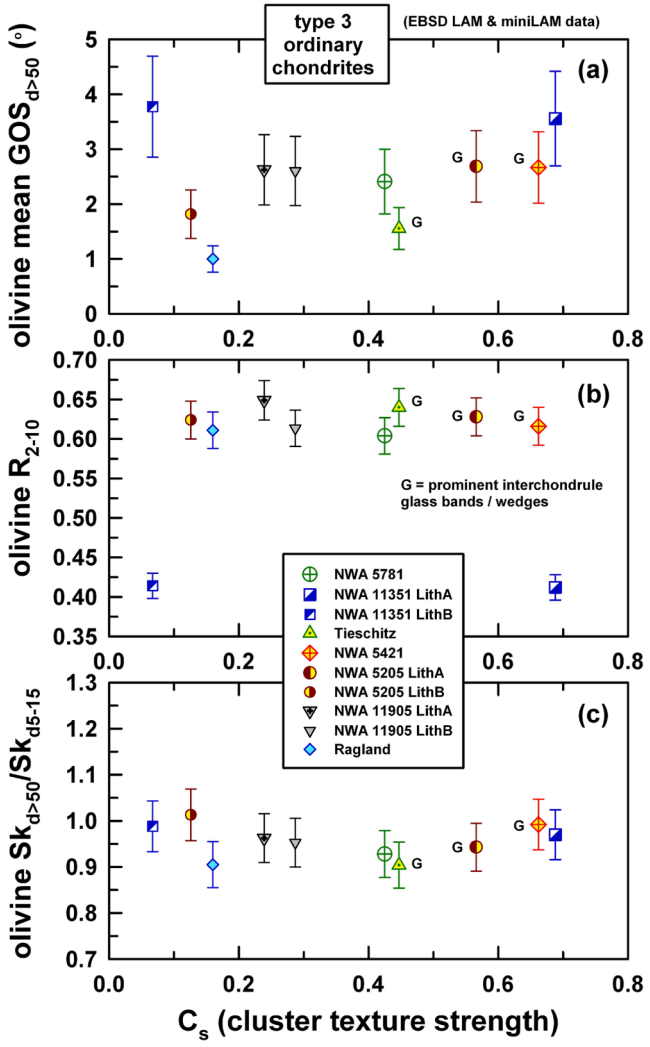

Fig. 15. Relationship between cluster texture strength (C_s) and EBSD olivine parameters including **(a)** mean $GOS_{d>50}$ ("deformation intensity"), **(b)** $R_{2\text{-}10}$ ("relative deformation temperature"), and **(c)** $Sk_{d>50}/Sk_{d5\text{-}15}$ ("large-scale annealing" parameter). EBSD parameters are averaged data from *LAMs* and *miniLAMs* and error bars are a measure of repeatability.

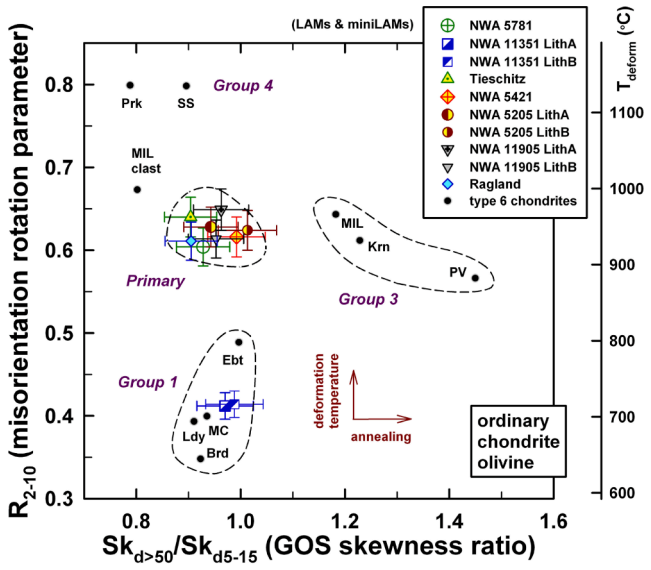

Fig. 16. Classification of ordinary chondrites into groups based on olivine EBSD characteristics. Type 3 chondrites can be assigned into a Primary Group that reflects initial formation characteristics and into a *Group 1* that also includes Type 6 chondrites. *Groups 3* and *4* are represented by other Type 6 chondrites. See Text.

strongly clustered chondrites could have formed in events involving relatively little crystal-plastic deformation, and that some or all could have experienced additional shock.

Brecciation and fracturing appear to have been important in the formation of the chondrites. Brecciation clearly was involved in the formation of well-defined clasts of strongly clustered and moderately clustered lithologies ("Lithology A clasts", Sec. 3.1.1) (Fig.1e-g). The existence of the Lithology A clasts implies that brecciation broke precursor rocks but did not finely comminute them. A greater amount of comminution would be necessary to make weakly clustered lithologies from strongly clustered ones. Lithology B of NWA 5205, Lithology B of NWA 11351, Lithology B of NWA 11905, and Ragland all could have been derived by more substantial comminution.

However, brecciation that substantially destroyed cluster textures, and involving much comminution, perhaps counterintuitively need not have been accompanied by much plastic deformation. This is illustrated by Ragland, which has both low mean $GOS_{d>50}$ and low C_s (Fig. 15a). Despite weak plastic deformation effects, brecciation in Ragland was likely responsible for creating many lithic and mineral clasts, including chondrite clasts that differ in matrix textures (Sec. 3.1.3, Fig. 3k, 3m).

Therefore, there is evidence for brecciation of different scales and types, either breaking strongly clustered lithologies but leaving them mostly intact (Lithology A clasts) or destroying them substantially (Lithology B hosts). That only modest plastic deformation in olivine occurred in most lithologies suggests that weak shock events (S1-S3) were responsible for most of this brecciation. A dominance of brittle deformation over plastic deformation for olivine is expected for olivine at low temperatures, estimated as <600-830 °C in laboratory experiments at low confining pressures (Druiventak et al., 2011; Boioli et al., 2015). This is consistent with low shock temperature increases corresponding to S1-S3 shock pressures (Stöffler et al., 1991), estimated as <50-600 °C (Schmitt, 2000; Hu and Sharp, 2022).

On the other hand, in strongly shocked NWA 11351, some plastic deformation may have accompanied brecciation. Weakly clustered Lithology B has both higher averaged olivine $GOS_{d>50}$ (3.78°) and shock stage (WSS = 3.87) than strongly clustered Lithology A ($GOS_{d>50}$ = 3.56°, WSS = 3.76), suggesting that if Lithology B were derived from Lithology A, both intense comminution as well as intracrystalline plastic deformation occurred.

It is further obvious that cluster texture strength values are not correlated with misorientation rotation axis parameter $R_{2\text{-}10}$ or GOS skewness ratio $Sk_{d>50}/Sk_{d5\text{-}15}$ (Fig. 15b-c). The $R_{2\text{-}10}$ parameter is roughly constant for most Type 3 chondrites over nearly the complete range of cluster texture strengths, and the only exception is NWA 11351, which had $R_{2\text{-}10}$ reset later during strong shock (Sec. 4.1.3). GOS skewness ratio $Sk_{d>50}/Sk_{d5\text{-}15}$ is also relatively constant for all lithologies despite large variations in cluster texture strength. Thus, it appears that cluster texture strength was not related to deformation temperature or to asymmetries in GOS distribution for grain populations.

An apparent metric related to small-scale annealing in these chondrites is $Sk_{d<5}/Sk_{d5\text{-}15}$ (Sec. 4.2.2). Based on this metric and trends with $GOS_{d<5}$ values, the best evidence for annealing occurs in lithologies that are both strongly clustered (Tieschitz) and weakly clustered (parts of NWA 5205 Lithology B and Ragland) (Sec. 4.2.2; Fig. 9b). Therefore, cluster chondrite texture is not obviously related to post-deformation annealing. Nor is it related to chondrite subtype (Table 1).

The similarity between weakly clustered and strongly clustered chondrites in GOS values, $R_{2\text{-}10}$ values, $Sk_{d>50}/Sk_{d5\text{-}15}$ values, and the lack of any evidence for systematic differences in annealing, suggest that weakly clustered and strongly clustered chondrites both formed initially in the same way. Evidently, the difference was that in the case of weakly clustered lithologies, the chondrites experienced subsequent brecciation. Our data therefore support the hypothesis of Metzler (2012) that strongly clustered lithologies could represent a "primary accretionary rock", and that weakly clustered lithologies were produced by the brecciation of such primary rock. Strong shock events need not have been involved in this transformation.

The only feature of the chondrites that *does* appear to be related to cluster texture strengths is the presence or absence of distinct interchondrule glass bands and triangular glass wedges. The three lithologies that contain such interchondrule glass, including Tieschitz, NWA 5205 Lithology A, and NWA 5421, have among highest cluster texture strengths (these lithologies are labeled with "G" in Fig. 15). This could indicate that such interchondrule glass was related to the formation of strong cluster textures. The origin of interchondrule glass will be discussed below. But here we suggest that post-agglomeration shock processes could have helped to destroy interchondrule glass bands and glass wedges in all chondrites that lack these features.

Post-agglomeration shock was strong in NWA 11351 and created strongly foliated metal and troilite (Sec. 3.5, Fig. 8). In Lithology A, shock may have destroyed glass bands and wedges as chondrules were pushed together during compaction, potentially even increasing cluster texture strength. In Lithology B, shearing and fracturing largely destroyed the original chondrite texture. Strong shock in NWA 11351 could have been responsible for a variety of features found only in this chondrite (Sec. 3.1.5), including: (1) melting chondrule mesostases to produce glass (Fig. 3i), similar to that inferred for Type 3 shock stage S5 chondrite NWA 8709 (Ruzicka et al., 2020); (2) removal of all crystalline feldspar by melting to produce glass; and (3) destruction of feldspar and olivine by melting or vitrification to form "spotted matrix", including apparently glassy olivine, which can be produced by strong shock (Jeanloz et al., 1977).

For the remaining lithologies that lack interchondrule glass bands and wedges, shock effects were lower but variable. On the low-shock extreme is Ragland, in which extensive brecciation on larger and smaller scales in one or more weak shock events would have thoroughly destroyed any interchondrule glass patches. On the high-shock extreme is NWA 5781, in which metal and troilite became well-foliated in a late shock (Sec. 3.5) even though the strong cluster texture was not destroyed (Fig. 8). We speculate that during this event, brittle Na-rich interchondule glass could have been fractured and mixed with small matrix particles, resulting in a bulk Na content of matrix that is somewhat elevated (Fig. 2b).

4.5. Bleached chondrules, glass, and fine-grained olivine-rich objects

Type 3 chondrites contain various petrographic features that might be related to accretionary conditions, including bleached chondrules, interchondrule glass, and fine-grained olivine-rich objects.

4.5.1. Bleached chondrules

Many researchers have attributed glass loss from the outer parts of chondrules ("bleaching") in ordinary chondrites to aqueous alteration, which could selectively leach glass and leave surrounding minerals such as pyroxene and olivine unaffected (Kurat, 1969; Hutchison et al., 1998; Grossman et al., 2000; Lewis et al., 2018; Lewis and Jones, 2019). This would seem to well explain our observations of bleached chondrule margins (Fig. 2d) and is the interpretation favored here. However, it was also suggested that feldspathic mesostasis melt in Tieschitz could have been expelled from chondrules during accretion while chondrules were mutually deformed (Hutchison et al., 1979, 1998), that pyroxene-enriched margins of mesostases could be consistent with loss of feldspathic melt that became separated from already-crystallized pyroxene (Hutchison et al., 1998), and that both melt removal and later aqueous alteration may have occurred (Hutchison et al., 1998). Rather than attempt to conclusively resolve these possibilities, we here focus on the relationship between bleaching and deformation.

Data support the inference that bleaching both post-dated and pre-dated deformation (Grossman et al. 2000) (Sec. 3.1.4). However, with evidence that there were multiple episodes of deformation (Sec. 4.1.3, 4.2.2, 4.3, 4.4), the significance of how bleaching fits into an overall formation scenario for Type 3 chondrites is not immediately apparent.

We suggest that the data can be accommodated by a model in which bleaching occurred *after* initial deformation events that occurred before or during final agglomeration, and *before* later brecciation episodes.

Thus, weakly clustered chondrites such as Ragland and Lithology B of NWA 5205 show good evidence of pre-deformation bleaching episodes because these lithologies experienced a late brecciation (Sec. 4.4). Many apparently broken chondrules in Ragland completely lack evidence for bleaching and have mesostasis Na-glass in direct contact with matrix, as could arise if brecciation removed bleached chondrule margins. Examples include olivine microporphyry 2-5 (Fig. 3j) and Object g (Fig. 3m) which sits astride an apparent breccia contact between two matrix types and so must have been fragmented late. Likewise, in NWA 5205 Lithology B, fine-grained olivine-rich Clast AD (Fig. 3g-h) was bleached prior to a late fragmentation event that created the clast (Sec. 3.1.4).

For strongly clustered chondrites excluding shock-overprinted NWA 11351, evidence suggests bleaching followed an initial deformation. Examples include Object b1 in NWA 5781 (Fig. 2a-c), which was bleached after agglomeration (Sec. 3.1.4). Another example is the earlier deformation that affected Chondrule b in NWA 5205 Lithology A (Fig. 2l-n). This chondrule experienced a later deformation that removed part of the bleached margin and which possibly also microfaulted nearby Chondrule 10-5-5 (Fig. 2l) (Sec. 3.1.4).

In both NWA 5781 and NWA 5205 Lithology A, the strong cluster texture was not destroyed by subsequent deformation, and bleaching could have occurred nearly *in situ*. In contrast, bleached Chondrule b in Ragland at indent points 1 and 2 (Fig. 3j-k) must have been deformed and bleached prior to brecciation (see above), which destroyed strong cluster texture (Sec. 4.4). Indent points 1 and 2 either were deformed prior to accretion by collision between chondrules in space, or during accretion by mutual deformation between chondrules. In both cases, deformation and bleaching occurred before the final assembly of Ragland.

Thus, *data suggest a scenario whereby an initial deformation associated with collisions in space or agglomeration was followed by bleaching, which was followed by later deformation that mechanically reworked chondrules with no further bleaching activity.* If bleaching was the result of aqueous alteration, and chondrules accreted warm and cooled more slowly after their accretion into a parent body (Sec. 4.1-4.3), it is possible that aqueous alteration occurred in response to the heat released from this process.

4.5.2. Interchondrule glass (white matrix)

Studies of white matrix (what we call interchondrule glass) in Tieschitz (Sec. 3.1.2, Sec. 3.7.1) have led to the conclusion that it was derived from chondrule mesostases (Michel-Levy, 1976; Hutchison et al., 1979, 1998). Similar material is now known to be present in NWA 5421 and NWA 5205 Lithology A (Sec. 3.1.2), which together with Tieschitz represent the most strongly clustered lithologies we have studied (excluding strongly shocked NWA 11351 Lithology A). Like previous workers, we suggest that the feldspathic matrix was derived from chondrules and deposited in matrix. We further suggest that it was associated with chondrule bleaching (Sec. 3.1.4) and that it could be a feature of the ordinary chondrite "primary accretionary rock" of Metzler (2012) (Sec. 4.4).

Chemical data strongly support the hypothesis that interchondrule glass was derived from the feldspathic mesostases of chondrules during a mobilization that corresponds to "bleaching" events. The composition of glass in chondrules and adjacent interchondrule glass in NWA 5421 are similar (Sec. 3.7.2, Table 5). Furthermore, the average composition of chondrule mesostasis in Tieschitz lies nearly on a tie line between interchondrule glass and the outer parts of chondrule mesostases that have been bleached (Fig. 10). This suggests removal of a glassy feldspar component from mesostasis to leave behind an augite-rich residuum in the bleached chondrule margins, and the deposition of this feldspar component in matrix to form the interchondrule glass.

Based on the average compositions in Table 5, the chemistry of feldspathic materials appears to have changed somewhat during mobilization, starting out slightly silica oversaturated in chondrule mesostases, and ending up more silica-undersaturated in the interchondrule areas. At the outermost edges of chondrules, at the transition to fine-grained rims or matrix, there is often phosphate (Fig. 2d). We speculate this phosphate was formed by a combination of enhanced Ca activity (in the augite-rich outer mesostasis) and decreased Si activity (in the matrix) together with availability of P at the chondrule/matrix interface where the composition changes most rapidly.

The nature and associated temperature of the mobilization event is debatable. Textural evidence allows latitude in possible mobilization mechanisms. Interchondrule glass contains mineral clasts and inclusions of rim material and can be highly vuggy (Fig. 2o-p). The presence of clasts and inclusions of rim material inside the interchondrule glass suggest mechanical break-up of chondrules and rims prior to the formation of the glass, consistent with bleaching and glass deposition after accretion-related chondrule deformation (Sec. 4.5.1). Vugs in the glass suggest the presence of a fluid or gas phase, either an aqueous fluid at low temperature or a gas phase at elevated temperature. Fine grained chondrule rims often intervene between bleached chondrule margins and interchondrule glass (Fig. 2d). This raises the possibility of leaching occurring through the rims, especially if the transfer medium was gaseous and there was some porosity in the rims to allow passage of gas (Michel-Levy, 1976). Transport through porous rims seems possible also for an aqueous fluid, but unlikely for melt that was highly viscous, as might be true for feldspathic eutectic melt in chondrules (Hutchison et al., 1979). Cracks in fine grained rims (Fig. 2d) allow another possible pathway, but again transfer from chondrule to matrix would be more consistent with low-viscosity gas or aqueous fluid and less likely for viscous melt. Chondrules are often fragmented (Fig. 2d) and fine-grained rims are often incomplete (Fig. 2o), which could have exposed the interiors of chondrules to their surroundings. If viscous mesostasis melts were mobilized, removal from chondrules during fragmentation is the most likely way to get these melts into the matrix.

4.5.3. Fine-grained olivine-rich objects

Distinctive fine-grained to cryptocrystalline olivine-rich objects that are texturally dissimilar to most chondrules were found in various Type 3 chondrites (Sec. 3.1.4). All are dominated by olivine crystallites that typically form multiple orientation domains within the objects, a "dendritic" texture that likely reflects a crystallization fabric produced during rapid cooling (Welsch et al., 2013). All have high olivine *GOS* values, which could be explained by lattice mismatches during rapid solidification (Welsch et al., 2013). They texturally and mineralogically resemble the "melt clast" in MIL 99301 that was interpreted to be a rapidly crystallized shock melt (Ruzicka and Hugo, 2018). We suggest that these objects could have crystallized rapidly from olivine-rich melts before and during agglomeration in different cases.

Olivine-rich pockets in Tieschitz could have crystallized largely *in situ*. The most prominent example is Object 5-1, which fills an irregular space between adjacent chondrules, rims, and interchondrule glass in matrix (Fig. 2g-h; Sec. 3.1.4). The margins of this object conform well to the surrounding chondrules, with many convex inward projections, suggesting it formed *in situ*. Olivine crystallites within 5-1 are locally aligned subparallel to adjacent chondrules except at opposite ends of the elongated object (Fig. 2g), as if these crystallites formed in a melt mush that was compressed between adjacent chondrules and became aligned. The object contains inclusions of both interchondrule glass and fine-grained rim (Fig. 2g-h), suggesting it crystallized after both had formed. Olivine-rich lumps in Tieschitz such as 5-1 were texturally late features.

The composition of olivine-rich pockets in Tieschitz ranges from nearly pure olivine to material like fine-grained and medium-grained rims on chondrules (Fig. 10, Table 5; Sec. 3.7.1). Based on average normative compositions, pockets differ from fine-grained rims mainly in

the proportion of olivine to feldspar, with olivine:plagioclase ~ 89:8 in pockets and ~76:16 in rims (Table 5). This implies that pockets are an olivine-rich, coarse-grained variant of rim material. It could indicate that the pockets formed by the melting of fine-grained ferromagnesian material like rims, accumulation of this material into spaces between chondrules, and subsequent olivine crystallization. Although one might argue for shock melting to produce them, this is unlikely owing to the weakly shocked character (S1) of Tieschitz. Rather, it appears that the pockets accreted while in the molten state.

Object 1-1 in NWA 5421 resembles Object 5-1 in Tieschitz in some ways and differs in others. The olivine-rich mineralogy and texture of crystallites are similar, but whereas Object 5-1 has convex-inwards margins and appears to fill space between chondrules, Object 1-1 has convex-outward margins and appears to have pushed against and indented neighboring chondrules 1-2 and 1-4 with a combination of microfaulting and plastic deformation (Fig. 2i-k; Sec. 3.1.2, 3.1.4). These features suggest Object 1-1 was largely solid at the time of impingement deformation. Given the significant deformation against the adjacent chondrules, it seems unlikely that the weak shock experienced by NWA 5421 (shock stage S2) could have been responsible. Rather, such deformation probably occurred at an early stage, during the accretion of Object 1-1 and neighboring chondrules, while these objects were somewhat plastic and still warm.

We infer that *all the fine-grained olivine-rich objects in chondrites crystallized rapidly from olivine-rich melts, but accreted in various physical states, ranging from solid and warm in NWA 5421 (Object 1-1) to partly molten in Tieschitz (Object 5-1 and other olivine pockets)*. This interpretation supports the idea of accretion of warm chondrules, as heating of these materials could have occurred just before accretion.

The fine-grained olivine-rich clast at the edge of Lithology A in NWA 11905 (Fig. 3c-e) provides an unusually good example of late deformation partly overprinting earlier misorientations recorded in the interior (Sec. 4.1.3). The interior misorientations are associated with $R_{2\text{-}10}$ and T_{deform} values (0.747 and 1079±82 °C, respectively) close to the expected solidus and may indicate deformation associated with solidification, although it is also possible that lattice mismatches during rapid crystallization (Welsch et al., 2013) may have occurred in a way that do not accurately record temperature.

4.6. Chondrite primary and secondary conditions

Olivine grains in the shock stage S1-S3 Type 3 chondrites of this study appear to record some of the original deformation-thermal conditions of ordinary chondrite formation. Figure 16 shows averaged values for olivine misorientation rotation parameter $R_{2\text{-}10}$ (proxy for deformation temperature) and *GOS* skewness ratio $Sk_{d>50}/Sk_{d5\text{-}15}$ (proxy for large-scale post-deformation annealing) in various chondrites. The S1-S3 Type 3 chondrites define a tight *"Primary"* field, with implied elevated deformation temperature (T_{deform} ~900-1000 °C) and minimal large-scale post-deformation annealing ($Sk_{d>50}/Sk_{d5\text{-}15} < 1$) (Sec. 4.1, 4.2). These characteristics can be explained by deformation of already warm chondrules (Sec. 4.1) that were cooling relatively rapidly (Sec. 4.3).

Two other groups of chondrites experienced either strong shock overprinting or significant annealing. High shock (S4-S5) chondrites, including representatives of both Type 6 and Type 3 chondrites, have lower $R_{2\text{-}10}$ and T_{deform} values but similarly low *GOS* skewness ratios ($Sk_{d>50}/Sk_{d5\text{-}15} \leq 1$) that define a relatively tight "*Group 1*" field (Fig. 16). *Group 1* chondrites experienced shock-heating from a cold ambient state and rapid cooling thereafter (Ruzicka and Hugo, 2018), and this was likely true also for NWA 11351. Three low-shock (S1) Type 6 chondrites, Portales Valley (H6), Kernouvé (H6), and MIL 99301 (LL6), form a "*Group 3*" field with both elevated $R_{2\text{-}10}$ and T_{deform} values and elevated *GOS* skewness ratios ($Sk_{d>50}/Sk_{d5\text{-}15} > 1$) (Fig. 16). This is attributed to deformation from a warm ambient state followed by burial metamorphism in a warm parent body (Ruzicka and Hugo, 2018).

Two other Type 6 chondrites, Saint-Séverin (LL6) and Park (L6), have high $R_{2\text{-}10}$ and T_{deform} values (1136±79 °C and 1137±79 °C, respectively) but low *GOS* skewness ratios ($Sk_{d>50}/Sk_{d5\text{-}15}$) (Fig. 16) and can be tentatively assigned to "*Group 4*". These chondrites could have been shocked while warm and rapidly cooled from high temperature, possibly caused by excavation from a hot parent body, and placement near the cool surface (Ruzicka and Hugo, 2018; Hugo et al., 2020). The apparent high deformation temperatures can be best explained by high pre-shock temperatures with superposed brief shock heating. This interpretation of supplemental shock heating is more plausible for Saint-Séverin, which has *CSS* = S4 and *WSS* = 3.2±1.2 (Hugo et al., 2020) than Park, which has *CSS* = S1 and *WSS* = 1.60±1.30 (Ruzicka and Hugo, 2018). In any case, heating to the temperatures implied by $R_{2\text{-}10}$ must have been brief to avoid much melting.

In essence, the Primary olivine field is defined both by an initial warm deformation signature, as well as an absence of significant modification by later shock or post-deformation annealing effects. In terms of Fig. 16, the S1-S3 Type 3 chondrites most closely resemble, but are distinct from, the high-*GOS* melt clast in MIL 99301 (labeled *Group 2* by Ruzicka and Hugo, 2018), which may have obtained high *GOS* during solidification (Sec. 4.5.3). This melt clast differs from chondrites in the Primary field obviously in texture but also in having high olivine mean *GOS* values. The clast's high *GOS* values are more similar to *Group 1* chondrites, but differs from them in having high T_{deform}, probably because it had a different paragenesis (misorientation while cooling from high temperatures, as opposed to deformation from a cold ambient condition).

Although the S1-S3 Type 3 chondrite lithologies resemble one another in terms of olivine $R_{2\text{-}10}$ and $Sk_{d>50}/Sk_{d5\text{-}15}$ EBSD parameters and in inferred deformation-thermal formation conditions (Sec. 4.1.1, 4.2, 4.3), they vary significantly in cluster chondrite textures and could have experienced significantly different impact histories after initial agglomeration (Sec. 4.4). Based on all available data, interpretations for all the Type 3 lithologies are given in Table 6. This table is ordered by cluster texture strength, higher at the top and lower at the bottom of the table. For lithologies lower in cluster texture strength, post-accretionary brecciation was probably important (Sec. 4.4). The two matrix types in weakly clustered Ragland (Sec. 3.1.3) could indicate two distinct generations of chondrite brecciation. Brecciation may have easily destroyed interchondrule glass bands and wedges (Sec. 4.4). Similarly, grain alignments of opaque minerals in response to shock compaction occurred even for shock stage S1-S3 chondrites (Friedrich et al., 2008, 2017). All these features in weakly shocked chondrites could have been affected by physical modifications involving mainly fracturing and grain displacement (Sec. 4.4).

4.7. Accretion of warm chondrules: a robust result?

The chief finding of this work is that chondrules could have been mutually deformed by collisions while they were still warm during cooling from higher temperatures, during their initial agglomeration into chondritic aggregates. But how robust is the inference for warm chondrule accretion?

Intragranular olivine misorientations imply a systematic change in slip systems during olivine deformation that are attributed to changes in deformation temperature (Sec. 4.1.1). Assuming temperature to be the main control, model deformation temperatures can be inferred (Sec. 4.1.2). However, the activation of slip systems also can depend on variables such as water content, pressure, and strain rate. Could these other variables have been important?

Water content is unlikely to have been a controlling factor. Increased water activity will promote **c**-type slip (Jung and Karato, 2001; Karato et al., 2018), which would have the effect of underestimating deformation temperatures, which are already elevated for S1-S3 Type 3 chondrites. Further, there is no evidence to suggest that chondrites dominated by **c**-type slip (*Group 1* Type 3 and 6 chondrites), formed

Table 6
Interpretations for Type 3 chondrite lithologies.

Cluster texture strength	Lithology	Interpretation
High	NWA 11351 Lith A	Late strong shock (overprinting) following parent body metamorphism, responsible for foliation, localized melting including inside chondrules and matrix regions; possible shock-induced strengthening of cluster texture
	NWA 5421	Accretion of warm chondrules with little fine-grained material; some fragmentation of chondrules; extrusion or leaching of feldspathic component from chondrules to form bleached chondrules and interchondrule glass deposits
	NWA 5205 Lith A	Accretion of warm chondrules with little fine-grained material (some as matrix lumps); some fragmentation of chondrules; extrusion or leaching of feldspathic component from chondrules to form bleached chondrules and interchondrule glass deposits; some bleached chondrules deformed again, later incorporation of Lith A as a large clast in the host of NWA 5205 (Lith B)
	Tieschitz	Accretion of warm chondrules with little fine-grained material (most as rims); some fragmentation of chondrules; in situ crystallization of interchondrule olivine-rich melt; extrusion or leaching of feldspathic component from chondrules to form bleached chondrules and interchondrule glass deposits
	NWA 5781	Accretion of warm chondrules with relatively little fine-grained material; some fragmentation of chondrules; later moderate shock to form a petrofabric (aligned metal-sulfide grains) that partly destroys previous matrix textures
	NWA 11905 Lith A	Warm chondrule accretion, with metal-troilite rims and fine-grained material; later brecciation produces Lith A as clasts incorporated in the host of NWA 11905 (Lith B)
	NWA 11905 Lith B	Warm chondrule accretion; later brecciation during moderately strong shock produces the host of NWA 11095, containing variably metamorphosed chondritic clasts (Lith A and Lith C)
	Ragland	Warm chondrule accretion; later extensive fragmentation and brecciation, with two brecciation events possible to create two types of matrix
	NWA 5205 Lith B	Warm chondrule accretion; later fragmentation; multiple brecciation events possible to create clasts within clasts; admixture of bleached objects and Lithology A chondritic clast to form the host of NWA 5205
Low	NWA 11315 Lith B	Late strong shock (overprinting) responsible for foliation, localized melting; extensively fragmented chondrule debris produces poor cluster texture, but compaction produces aligned metal-sulfide grains

under wetter conditions than other chondrites with more **a**-type slip (*Group 3* and *Group 4* Type 6 chondrites and Primary Type 3 chondrites) (Sec. 4.6). Bleached chondrules may indicate the presence of water (Grossman et al., 2000), and such chondrules are more widely found in Type 3 chondrules than previously supposed (Lewis and Jones, 2019; Sec. 3.1.4). However, bleaching and water activity appears to have followed initial deformation (Sec. 4.5.1), which may indicate that initial deformation occurred under dry conditions.

Pressure probably also was not a controlling factor. Increasing pressure appears to promote **a**-type slip (Carter and Ave'Lallemant, 1970), although the effect of pressure on slip in olivine is not well known (Karato et al., 2008), and although elevated pressures (≥3 GPa) accompanied by high shear strains accompanied by sustained plastic deformation at ~1300 °C favors **c**-type slip (Jung et al., 2008). The most strongly shocked chondrites have less **a**-type slip (*Group 1*, whereas less shocked chondrites (*Group 3, 4*, *Primary*) have more **a**-type slip. This is opposite to the pattern expected for a dominant pressure effect. Shock pressure alone during deformation evidently did not control the variation in slip behavior.

Strain rate undoubtedly was elevated during shock deformation but again was probably not the main control in slip system variations. Given that all the meteorites were likely deformed by shock, it is not obvious that differences between them in strain rates or shear stresses could account for the large slip variations. Higher strain rate has the effect of promoting **c**-type slip (Carter and Ave'Lallemant, 1970; Green, 1976), so higher strain rates would tend to lead to an underestimate in deformation temperatures, which are already elevated for S1-S3 Type 3 chondrites. Thus, appealing to strain rate effects cannot account for elevated deformation temperatures for these chondrites.

Finally, the temperature benchmarks used to infer T_{deform} potentially could be in error. However, the benchmarks are relatively well-supported by a variety of data, including geothermometry for the high temperature ureilite benchmark, and TEM evidence and Hugoniot calculations for the low temperature Morrow County benchmark (Sec. 4.1.2). Furthermore, the benchmarks lead to estimates for deformation temperatures for the *Group 3* Type 6 chondrites that agree with previous estimates (Ruzicka et al., 2015; Ruzicka and Hugo, 2018 and references therein). There is no indication the benchmarks are in significant error.

The main difficulty with assuming high deformation temperatures of accreting chondrules would seem to be the preservation of temperature-sensitive components in chondrites. However, this would be more of a problem if cooling after accretion were slow. If instead cooling rates were relatively fast after accretion (Sec. 4.3), this would be less of a constraint, because there would be limited heating. Furthermore, given that lithologies with strongly developed cluster textures are always present as clasts in chondrites (Sec. 3.1.1) (Metzler, 2012), much or all of the temperature-sensitive components that are present in the matrix of chondrites could have been added after the initial agglomeration of warm chondrules occurred. That is, the presence of temperature-sensitive components somewhere within a chondrite does not invalidate the idea that chondrules could have accreted while warm at an earlier time. Later addition of components following brecciation in chondrites is illustrated by studies of noble gases in chondrites such as NWA 5205, which show little solar wind implantation in the strongly clustered lithologies and more in weakly clustered host lithologies (Müsing et al., 2021). During such gas implantation, which must have occurred in a regolith (Müsing et al., 2021), admixture of hydrous materials, organic materials, pre-solar grains, and volatile elements could have occurred. More difficult to explain is the presence of carbon materials in dark rims in Tieschitz that imply a low temperature origin (Michel-Levy and Lautie, 1981). If these low-temperature organics are present in rims in a strongly clustered lithology such as Tieschitz, they must have been added to the chondrites at the time of accretion or been altered afterwards.

Overall, we assess that warm deformation of colliding chondrules during accretion is a robust result. However, it is not year clear how temperature-sensitive components in chondrites relate to the specific impact, metamorphic, and alteration histories experienced by chondrites.

5. Conclusion

Studies of Type 3 LL and H/L chondrites suggest that they experienced a complex series of deformation and thermal events. Data are consistent with a four-stage formation model (Fig. 17). From earliest to latest these include the following.

1 Stage 1 involved minor **pre-accretion collisions** of chondrules in the nebula followed by recovery in olivine over a ~1 μm scale during chondrule crystallization (Sec. 4.2, 4.3). Such collisions resulted in

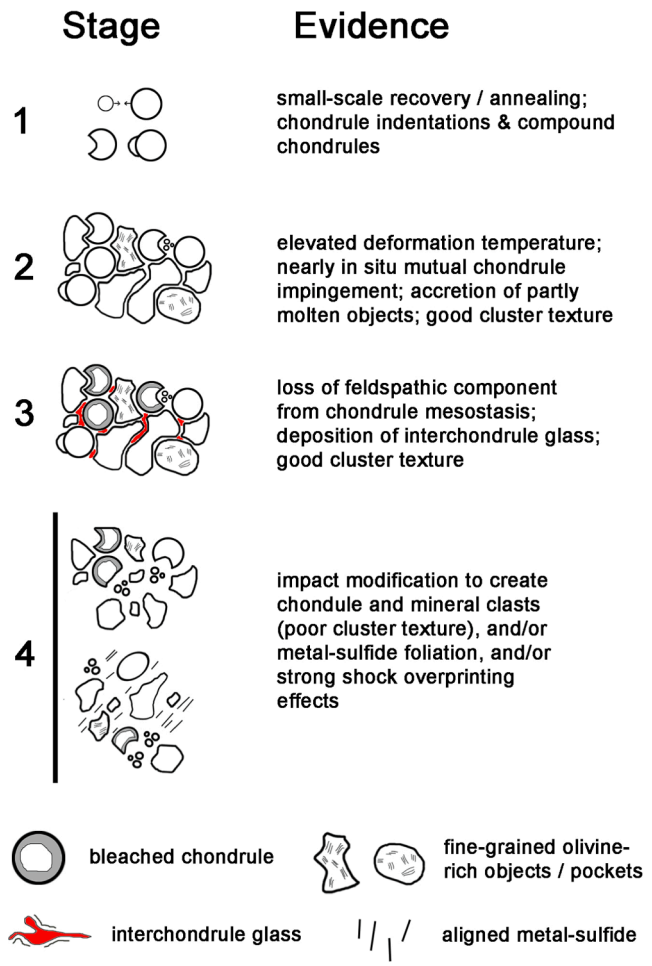

Fig. 17. Cartoon illustrating proposed four-stage model for Type 3 ordinary chondrites. Stage 1—pre-accretionary collisions resulting in cratered or indented chondrules, compound chondrules, and associated with small-scale annealing at magmatic temperatures (Sec. 4.2, 4.3). Stage 2— accretion of still-warm chondrules in an initial agglomeration (Sec. 4.1, 4.3, 4.4, 4.5, 4.7). Stage 3— bleaching event that transferred feldspathic material from chondrules into matrix to form interchondrule glass (Sec. 4.5). Stage 4— impact modification (Sec. 4.1, 4.4, 4.6).

chondrule indentations and compound chondrules; annealing affected the deformation character of small grains.

2 Stage 2 is represented by the initial **accretion of still-warm chondrules** into chondritic aggregates, possibly planetesimals, at an estimated effective accretion temperature of ~900-950 °C, as evidenced by an elevated temperature of deformation as recorded by intragranular olivine misorientations for weakly shocked (conventional shock stage S1-S3) chondrites, by evidence for mutual impingement and nearly *in situ* deformation between chondrules in strongly clustered chondrites, and by evidence that some fine-grained olivine-rich pockets in Tieschitz could have accreted while still partly molten (Sec. 4.1, 4.3, 4.4, 4.5, 4.7). The most texturally pristine chondrites that best record the accretion process and that escaped later significant impact effects are Tieschitz (S1), NWA 5421 (S2), and NWA 5205 Lithology A (S2), which all have good cluster textures and contain interchondrule glass deposits (white matrix) (Sec. 4.4).

3 Following accretion-related deformation, chondrules of many different textural types were affected by **bleaching** in Stage 3 that involved loss of feldspathic materials from chondrule margins and the deposition of interchondrule glass (Sec. 4.5).

4 In Stage 4, post-bleaching **impact modification** destroyed interchondrule glass deposits, and resulted in some combination of brecciation to create fragmental breccias (such as Ragland, NWA 5205 Lithology B, and NWA 11351 Lithology B); foliation of metal and sulfide (NWA 5781 and NWA 11351 Lithologies A and B); and localized shock melting or vitrification effects (NWA 11351 Lithologies A and B) (Sec. 4.4, 4.6).

Chondrites can be classified by EBSD metrics for olivine into different groups, including a *Primary* group that preserves initial formation conditions (Type 3 chondrites with shock stage S1-S3) characterized by high deformation temperature and low-moderate *GOS* values; and into *Group 1* chondrites that were affected by later strong shock (Type 3 and 6 chondrites with shock stage ≥S4) characterized by lower deformation temperature and high *GOS* values (Sec. 4.6). Neither group shows evidence for recovery (annealing) in olivine on a ≥ 5-15 μm scale. In addition, *Group 3* chondrites are Type 6 chondrites that show evidence for having been shocked while warm and then significantly annealed.

Altogether, data support the model of Metzler (2012), in which mutual chondrule collisions between warm chondrules in ordinary chondrites followed by initial lithification created Primary Accretionary Rock (PAR) with strong cluster texture, and subsequent brecciation broke PAR into clasts that remain as strongly clustered lithologies, or into smaller clasts that form weakly clustered lithologies. The accretion of warm chondrules in ordinary chondrites has major implications for accretionary processes in the early solar system, as it implies a strong link between chondrule formation, which provided heat, and the accretion of planetesimals, which was necessary to allow the growth of planetary bodies.

CRediT authorship contribution statement

Alex M. Ruzicka: . **Richard C. Hugo:** Writing – review & editing, Methodology, Investigation, Funding acquisition, Data curation, Conceptualization. **Jon M. Friedrich:** Investigation, Formal analysis, Data curation. **Michael T. Ream:** Investigation.

Data availability

Data are available through PDXScholar (Portland State University) at https://doi.org/10.15760/geology-data.06y (Ruzicka et al., 2023).

Declaration of competing interest

The authors declare that they have no known competing financial interests or personal relationships that could have appeared to influence the work reported in this paper.

Acknowledgments

This work was supported by NASA grant 80NSSC19K0517. The authors thank John Wheeler, two anonymous reviewers, and Melinda Hutson for constructive reviews that improved the quality of this manuscript.

Appendix A. Supplementary material

Appendix A includes information about shock stages for the samples studied including histogram data (Fig. S1); a narrative of petrographic details for each meteorite lithology accompanied by images (Fig. S2, Fig. S3); a list of abbreviations, map types and parameters used in this work (Table S1); and a list of tabulated SEM datasets including metadata, observations, and comments (Table S2). Supplementary material to this article can be found online at https://doi.org/10.1016/j.gca.2024.05.031.

References

Alexander, C.M.O.'D., Hutchison, R., Barber, D.J., 1989. Origin of chondrule rims and interchondrule matrices in unequilibrated ordinary chondrites. Earth Planet. Sci. Lett. 95, 187-207.

Arndt, J., Häberle, F., 1973. Thermal expansion and glass transition temperatures of synthetic glasses of plagioclase-like compositions. Contrib. Miner. Petrol. 39 (2), 175–183.

Ashworth, J.R., 1981. Fine structure in H-group chondrites. Proc. R. Soc. London, Ser. A 374, 179-194, 1981.

Best, M.G., 1982. Igneous and Metamorphic Petrology. W.H. Freeman and Co., New York.

Bischoff, A., Schleitung, M., Patzek, M., 2019. Shock stage distribution in 2280 ordinary chondrites—Can bulk chondrites with a shock stage of S6 exist as individual rocks? Meteorit. Planet. Sci. 54, 2189–2202.

Boioli, F., Tomassi, A., Cordier, P., Demouchy, S., Mussi, A., 2015. Low steady-state stresses in the cold lithospheric mantle inferred from dislocation dynamics models of dislocation creep in olivine. Earth Planet. Sci. Lett. 432, 232–242.

Brewer, L.N., Field, D.P., Merriman, C.C., 2009. Mapping and assessing plastic deformation using EBSD. In: Schwartz, A.J., Kumar, M., Adams, B.L., Field, D.P. (Eds.), Electron Backscatter Diffraction in Materials Science, Second ed. Springer, pp. 251–262.

Carter, N.L., 1971. Static deformation of silica and silicates. J. Geophys. Res. 76, 5514–5540.

Carter, N.L., Ave'Lallemant, H.G., 1970. High temperature flow of dunite and peridotite. Geol. Soc. Amer. Bull. 81, 2181–2202.

Ciesla, F.J., Lauretta, D.S., Hood, L.L., 2004. The frequency of compound chondrules and implications for chondrule formation. Meteorit. Planet. Sci. 39, 531–544.

Connolly Jr., H.C., Hewins, R.H., Atre, N., Lofgren, G.E., 1994. Compound chondrules: An experimental investigation. Meteoritics 29 (4), 458.

Costa, F., Chakraborty, S., 2008. The effect of water on Si and O diffusion rates in olivine and implications for transport properties and processes in the upper mantle. Phys. Earth Planet. Int. 166, 11–29.

Crank, J., 1975. The mathematics of diffusion. Clarendon Press, Oxford.

Dodd, R.T., 1981. Meteorites: A petrologic-chemical synthesis. Cambridge University Press.

Dohmen, R., Chakraborty, S., 2007. Fe–Mg diffusion in olivine II: point defect chemistry, change of diffusion mechanisms and a model for calculation of diffusion coefficients in natural olivine. Phys. Chem. Minerals 34, 409–430.

Druiventak, A., Trepmann, C.A., Renner, J., Hanke, K., 2011. Low-temperature plasticity of olivine during high stress deformation of peridotite at lithospheric conditions — An experimental study. Earth Planet. Sci. Lett. 311, 199–211.

Farla, R. J. M., Kokkonen, Fitz Gerald. J. D., Barnhoorn. A., Faul. U. H., Jackson. I., 2011. Dislocation recovery in fine-grained polycrystalline olivine. Phys. Chem. Minerals 38, 363–377.

Fei, H., Hegoda, C., Yamazaki, D., Wiedenbeck, M., Yurimoto, H., Shcheka, S., Katsura, T., 2012. High silicon self-diffusion coefficient in dry forsterite. Earth Planet. Sci. Lett. 345–348, 95–103.

Friedrich, J.M., Wignarajah, D.P., Chaudhary, S., Rivers, M.L., Nehru, C.E., Ebel, D.S., 2008. Three-dimensional petrography of metal phases in equilibrated L chondrites—effects of shock loading and dynamic compaction. Earth Planet. Sci. Lett. 275, 72–180.

Friedrich, J.M., Ruzicka, A., Macke, R.J., Thostenson, J.O., Rudolph, R.A., Rivers, M.L., Ebel, D.S., 2017. Relationships among physical properties as indicators of high temperature deformation or post-shock thermal annealing in ordinary chondrites. Geochim. Cosmochim. Acta 203, 157–174.

Frye, J. K., 2022. Electron backscatter diffraction analysis of olivine in ureilite meteorites: Evaluation of the partially magmatic catastrophic disruption model of the Ureilite Parent Body (UPB). M.S. Thesis, Portland State University. PDXScholar Paper 6004.

Gaines, R. V., Skinner H. C. W., Foord, E. E., Mason, B., Rosenzweig, A., 1997. Dana's New Mineralogy, Eighth Ed., John Wiley & Sons.

Goetze, C., 1978. The mechanisms of creep in olivine. Phil. Trans. Royal Soc Lond. Series A, Math. Phys. Sci. 288, 99–119.

Goetze, C., Kohlstedt, D.L., 1973. Laboratory study of dislocation climb and diffusion in olivine. J. Geophys. Res. 78, 5961–5971.

Gooding, J.L., Keil, K., 1981. Relative abundances of chondrule primary textural types in ordinary chondrites and their bearing on conditions of chondrule formation. Meteoritics 16 (1), 17–43.

Goudy, S. P., 2019. Assessment of cluster chondrite accretion temperature using electron backscatter electron diffraction and implications for chondrule formation models. M. S. Thesis, Portland State University. PDXScholar Paper 5268.

Green, H. W., 1976. Plasticity of olivine in peridotites. In H.-R. Wenk (ed.), Electron Microscopy in Mineralogy, Springer Berlin Heidelberg, pp. 443-464.

Grossman, J.N., Alexander, C.M.O.D., Wang, J., Brearley, A.J., 2000. Bleached chondrules: Evidence for widespread aqueous processes on the parent asteroids of ordinary chondrites. Meteorit. Planet. Sci. 35, 467–486.

Gueguen, Y., Nicolas, A., 1980. Deformation of mantle rocks. Ann. Rev. Earth Planet. Sci. 8, 119–144.

Guimon, R.K., Keck, B.D., Weeks, K.S., DeHart, J., Sears, D.W., 1985. Chemical and physical studies of type 3 chondrites. IV Annealing studies of a type 3. 4 ordinary chondrite and the metamorphic history of meteorites. Geochim. Cosmochim. Acta 49, 1515–1524.

Herrin, J.S., Zolensky, M.E., Ito, M., Le, L., Mittlefehldt, D.W., Jenniskens, P., Ross, A.J., Shaddad, M.H., 2010. Thermal and fragmentation history of ureilitic asteroids: Insights from the Almahata Sitta fall. Meteorit. Planet. Sci. 45, 1789–1803.

Hewins, R. H., Connolly, H. C., Jr., Lofgren, G. E., Libourel, G., 2005. Experimental constraints on chondrule formation, in: Krot, A. N., Scott, E. R. D., Reipurth, B. R. (eds.), Chondrites and the Protoplanetary Disk, ASP Conf. Series 341, pp. 286-316.

Hu, J., Sharp, T., 2022. Formation, preservation, and extinction of high-pressure minerals in meteorites: temperature effects in shock metamorphism and shock classification. Prog. Earth Planet Sci. 9 (1), 6.

Hubbard, A., 2015. Compound chondrules fused cold. Icarus 254, 56–61.

Hugo, R.C., Ruzicka, A.M., Rubin, A.E., 2020. Mesoscale and microscale shock effects in the LL6 (S4) chondrites Saint-Severin and Elbert: A tale of two breccias. Meteorit. Planet. Sci. 55, 1418–1438.

Huss, G.R., Rubin, A.E., Grossman, J.N., 2006. Thermal metamorphism in chondrites. In: Lauretta, D.S., McSween Jr., H.Y. (Eds.), Meteorites and the Early Solar System II. University of Arizona Press, pp. 567–586.

Hutchison, R., Bevan, A. W. R., 1983. Conditions and time of chondrule accretion, in: King, E. A. (ed.), Chondrules and Their Origins, Lunar and Planetary Institute, Houston, pp. 162-179.

Hutchison, R., Bevan, A.W.R., Agrell, S.O., Ashworth, J.R., 1979. Accretion temperature of the Tieschitz, H3, chondritic meteorite. Nature 280, 116–119.

Hutchison, R., Alexander, C. M.O' D., Bridges, J. C., 1998. Elemental redistribution in Tieschitz and the origin of white matrix. Meteorit. Planet. Sci. 33, 1169-1179.

Hutchison, R., 2004. Meteorites: A Petrologic, Chemical and Isotopic Synthesis. Cambridge University Press.

Hutson, M. L., Ruzicka, A. M., Nazari, M., 2014. Diverse and unusual O-chondrites from the Lut desert, Iran. In: 77th Annual Meeting of the Meteoritical Society, Abstract #5180.

Jamsja, N., Ruzicka, A., 2010. Shock and thermal history of NWA 4859, an annealed impact melt breccia of LL-chondrite parentage containing unusual igneous features and pentlandite. Meteorit. Planet. Sci. 45, 828–849.

Jarosewich, E., 1990. Chemical analyses of meteorites: A compilation of stony and iron meteorite analyses. Meteoritics 25, 323–337.

Jeanloz, R., Ahrens, T. J., Lally, J. S., Nord G. L., Jr., Christie, J. M., Heuer, A. H., 1977. Shock-produced olivine glass: First observation. Science 197, 457-459.

Jelinek, V., 1981. Characterization of the magnetic fabric of rocks. Tectonophysics 79, T63–T67.

Johansen, A., Mordecai-Mark, M.L., Lacerda, P., Bizzarro, M., 2015. Growth of asteroids, planetary embryos, and Kuiper belt objects by chondrule accretion. Sci. Adv. 1 (3), e1500109.

Jung., H., Mo, W., Green, H. W., 2008. Upper mantle seismic anisotropy resulting from pressure-induced slip transition in olivine. Nature Geoscience 2, 73-77.

Jung, H., Karato, S.-I., 2001. Water-induced fabric transitions in olivine. Science 293, 1460–1463.

Karato, S.-I., Rubie, D.C., Yan, H., 1993. Dislocation recovery in olivine under deep upper mantle conditions: Implications for creep and diffusion. J. Geophys. Res. 98, 9761–9768.

Karato, S.-I., Jung, H., Katayama, I., Skemer, P., 2008. Geodynamic significance of seismic anisotropy of the upper mantle: new insights from laboratory studies. Annu. Rev. Earth Planet. Sci. 36, 59–95.

Kostynick, R. P., 2019. Bleached Chondrules and the Possible Influence of Aqueous Alteration. Geology Undergraduate Honors Thesis, Portland State University. https://pdxscholar.library.pdx.edu/geology_honorsthesis/1.

Kurat, G., 1969. The formation of chondrules and chondrites and some observations on chondrules from the Tieschitz meteorite, in: Millman, P. M. (ed.), Meteorite Research, Springer, Dordrecht, pp. 185-190.

Lewis, J.A., Jones, R.H., 2019. Primary feldspar in the Semarkona LL 3.00 chondrite: Constraints on chondrule formation and secondary alteration. Meteorit. Planet. Sci. 54, 72–89.

Lewis, J.A., Jones, R.H., Garcea, S.C., 2018. Chondrule porosity in the L4 chondrite Saratov: Dissolution, chemical transport, and fluid flow. Geochim. Cosmochim. Acta 240, 293–313.

Mainprice, D., Nicolas, A., 1989. Development of shape and lattice preferred orientations: application to the seismic anisotropy of the lower crust. J. Structural Geol. 11, 175–189.

MBD, 2023. Meteoritical Bulletin Database, https://www.lpi.usra.edu/meteor/ (accessed July 13, 2023).

Metzler, K., 2012. Ultrarapid chondrite formation by hot chondrule accretion? Evidence from unequilibrated ordinary chondrites. Meteorit. Planet. Sci. 47, 2193–2217.

Metzler, K., Pack, A., 2016. Chemistry and oxygen isotopic composition of cluster chondrite clasts and their components in LL 3 chondrites. Meteorit. Planet. Sci. 51 (2), 276–302.

Michel-Levy, M.C., 1976. La matrice noire et blanche de la chondrite de Tieschitz (H3). Earth Planet. Sci. Lett. 30, 143–150.

Michel-Levy, M.C., Lautie, A., 1981. Microanalysis by Raman spectroscopy of carbon in the Tieschitz chondrite. Nature 292, 321–322.

Müsing, K., Busemann, H., Huber, L., Maden, C., Riebe, M.E., Wieler, R., Metzler, K., 2021. Noble gases in cluster chondrite clasts and their host breccias. Meteorit. Planet. Sci. 56, 642–662.

Phakey, P., Dollinger, G., Christie, J., 1972. Transmission electron microscopy of experimentally deformed olivine crystals. In Flow and Fracture of Rocks, American Geophysical Union Geophysical Monograph Series, 16, pp.117-138. Washington, D. C.

Rai, N., Downes, H., Smith, C., 2020. Ureilite meteorites provide a new model of early planetesimal formation and destruction. Geochem. Perspectives Lett. 14, 20–25.

Raleigh, C.B., 1968. Mechanisms of plastic deformation of olivine. J. Geophys. Res. 73, 5391–5406.

Rubin, A.E., Brearley, A.J., 1996. A critical evaluation of the evidence for hot accretion. Icarus 124, 86–96.

[Dataset] Ruzicka, A.M., Hugo, R.C., Friedrich, J.M., Ream, M.T., 2023. Data from: Accretion of warm chondrules in weakly metamorphosed ordinary chondrites and their subsequent reprocessing.

Ruzicka, A., Hugo, R., Hutson, M., 2015. Deformation and thermal histories of ordinary chondrites: Evidence for post-deformation annealing and syn-metamorphic shock. Geochim. Cosmochim. Acta 163, 219–233.

Ruzicka, A.M., Hugo, R.C., 2022a. Model deformation temperatures derived from EBSD data for olivine in type 6 ordinary chondrites and ureilites. In: 53rd Lunar and Planetary Science Conference, #1757.

Ruzicka, A.M., Hugo, R.C., 2022b. A robust Electron Backscatter Diffraction annealing metric for olivine. In: 85th Annual Meeting of the Meteoritical Society, Abstract #6179.

Ruzicka, A.M., Hugo, R.C., 2018. Electron Backscatter Diffraction (EBSD) study of seven heavily metamorphosed chondrites: Deformation systematics and variations in pre-shock temperature and post-shock annealing. Geochim. Cosmochim. Acta 234, 115–147.

Ruzicka, A.M., Friedrich, J.M., Hutson, M.L., Strasser, J.W., Macke, R.J., Rivers, M.L., Greenwood, R.C., Ziegler, K., Pugh, R.N., 2020. Shock compaction heating and collisional processes in the production of type 3 ordinary chondrites: Lessons from the (nearly) unique L3 chondrite melt breccia Northwest Africa 8709. Meteorit. Planet. Sci. 55, 1418–1438.

Schmitt, R.T., 2000. Shock experiments with the H6 chondrite Kernouvé: Pressure calibration of microscopic shock effects. Meteorit. Planet. Sci. 35, 545–560.

Sharp, T.G., DeCarli, P.S., 2006. Shock effects in meteorites. In: Lauretta, D.S., McSween, H.Y., Jr. (Eds.), Meteorites and the Early Solar System II. University of Arizona Press, pp. 653–677.

Singletary, S.J., Grove, T.L., 2003. Early petrologic processes on the ureilite parent body. Meteorit. Planet. Sci. 38, 95–108.

Skinner, W.R., McSween Jr., H.Y., Patchen, A.D., 1989. Bleached chondrules and the diagenetic histories of ordinary chondrite parent bodies. Meteoritics 24, 326.

Stöffler, D., Hamann, C., Metzler, K., 2019. Addendum to "Stöffler, D., Hamann, C., and Metzler, K., Shock metamorphism of planetary silicate rocks and sediments: Proposal for an updated classification system. Meteoritics & Planetary Science 53, 5–49, 2018". Meteorit. Planet. Sci. 54, 946-949.

Stöffler, D., Keil, K., Scott, E.R.D., 1991. Shock metamorphism of ordinary chondrites. Geochim. Cosmochim. Acta 55, 3845–3867.

Stöffler, D., Hamann, C., Metzler, K., 2018. Shock metamorphism of planetary silicate rocks and sediments: Proposal for an updated classification system. Meteorit. Planet. Sci. 53, 5–49.

Tielke, J.A., Zimmerman, M.E., Kohlstedt, D.L., 2016. Direct shear of olivine single crystals. Earth Planet. Sci. Lett. 455, 140–148.

Tommasi, A., Mainprice, D., Canova, G., Chastel, Y., 2000. Viscoplastic self-consistent and equilibrium based modeling of olivine lattice preferred orientations: Implications for the upper mantle seismic anisotropy. J. Geophys Res. Solid Earth 105 (B4), 7893–7908.

Warren, P. H., 1997. The unequal host-phase density effect in electron probe defocused beam analysis: an easily correctable problem. In: 26th Lunar and Planetary Science Conference, Abstract #1406.

Wasson, J.T., Krot, A.N., Lee, M.S., Rubin, A.E., 1995. Compound chondrules. Geochim. Cosmochim. Acta 59 (9), 1847–1869.

Welsch, B., Faure, F., Famin, V., Baronnet, A., Bachèlery, P., 2013. Dendritic crystallization: a single process for all the textures of olivine in basalts? J. Petrol. 54, 539–574.

Woodcock, N.H., Naylor, M.A., 1983. Randomness testing in three-dimensional orientation data. J. Structural Geol. 5, 539–548.